TREND AND ADVANCED STUDIES IN CIVIL ENGINEERING

All Sciences Academy

TRENDAND ADVANCED STUDIES IN CIVIL ENGINEERING

Editor

Asst. Prof. Dr. Serdar KORKMAZ

Trend and Advanced Studies in Civil Engineering
Editor: Asst. Prof. Dr. Serdar KORKMAZ

Design: All Sciences Academy Design
Published Date: July 2026
Publisher's Certification Number: 72273
ISBN: 978-625-8839-39-5

www.allsciencesacademy.com
allsciencesacademy@gmail.com

CONTENT

A Hypoplasticity Model for Cohesionless Soils

Bayram ATEŞ[1*]

Mehmet Ali KALAYLI[2]

1- Dr.; Karadeniz Technical University, Faculty of Engineering, Department of Civil Engineering, 61030, Trabzon, Türkiye. bayramates61@hotmail.com, ORCID No: 0000-0002-1251-7053 (corresponding author)[*]
2- Dr.; Kırıkkale University, Faculty of Engineering, Department of Civil Engineering, 71000, Kırıkkale, Türkiye. mehalkal777@gmail.com, ORCID No: 0000-0003-2776-4740

ABSTRACT

The stress–strain behaviour of cohesionless soils exhibits features that are difficult to represent in a unified manner with classical approaches, such as density- and stress-level-dependent stiffness, irreversibility upon loading and unloading, volume change during shearing, post-peak softening, and the tendency towards a critical state at large strains. This chapter examines hypoplastic constitutive models, which describe these behaviours through a single incremental (rate-type) tensorial equation, within a framework extending from their theoretical foundations to engineering applications. First, the basic mechanical behaviour of granular soils is summarised in the light of experimental observations; then the mathematical structure of hypoplasticity, the model adopted as a reference for cohesionless soils, and its eight material parameters are introduced. The determination of the parameters through standard laboratory tests, the principles of calibration and validation, and the intergranular strain extension that improves the small-strain and cyclic-loading response are explained. Finally, the place of the model in geotechnical applications is assessed, and its advantages and limitations are compared with those of other widely used constitutive models. The chapter shows that hypoplasticity offers a powerful and consistent modelling framework for state- and loading-path-dependent problems, capable of covering a broad density–pressure range with a relatively small number of physically meaningful parameters.

Keywords – Hypoplasticity, cohesionless soil, constitutive model, sand, intergranular strain, cyclic loading.

INTRODUCTION

Numerical modelling has become an indispensable tool in geotechnical engineering for the design of complex soil–structure interaction problems, deep excavations, tunnels, and geotechnical systems subjected to dynamic loads. The reliability of a numerical analysis depends, above all, on the realism of the constitutive model that represents the stress–strain behaviour of the soil (Bayraktaroğlu, 2019; Mašín, 2019). Cohesionless (granular) soils such as sand and gravel exhibit behavioural features not encountered in classical engineering materials, including density- and stress-level-dependent stiffness, post-peak softening, volume change during shearing (dilatancy/contraction), pronounced irreversibility upon loading and unloading, and cumulative deformation under cyclic loading. Representing all of these features consistently within a single mathematical framework is one of the most challenging theoretical problems in soil mechanics.

The classical elastoplastic approach widely used for modelling soil behaviour rests on a number of additional concepts, such as a yield surface, a flow rule, a plastic potential, a hardening law, and the decomposition of strain into elastic and plastic components (Schofield and Wroth, 1968; Roscoe et al., 1958). Simple elastoplastic models such as Mohr–Coulomb can reproduce the nonlinear, density- and pressure-dependent behaviour of granular soils only crudely; the assumption of fully elastic (reversible) behaviour for stress states inside the yield surface fundamentally contradicts real soil behaviour, because experimental observations show that in granular soils every stress change, however small, produces some permanent strain (Kolymbas, 2000). More advanced elastoplastic models have sought to remedy these shortcomings through multiple yield surfaces, the bounding-surface concept, or kinematic hardening; this, however, has considerably complicated the model structure and increased the number of parameters (Niemunis, 2003; Wichtmann et al., 2019).

As an alternative to this complexity, hypoplasticity is a family of constitutive theories developed around the University of Karlsruhe that describes soil behaviour holistically through a single tensorial rate equation, without recourse to concepts such as a yield surface, a plastic potential, or strain decomposition (Kolymbas, 1991; Gudehus, 1996; von Wolffersdorff, 1996). The prefix “hypo” (meaning “less”) in the name of the theory indicates that fewer conceptual building blocks are required than in plasticity theory. In hypoplastic models, the distinction between loading and unloading is provided intrinsically by the nonlinear dependence of the equation on the strain rate, rather than by an externally defined loading criterion; the concepts corresponding to a failure surface and a flow rule emerge spontaneously as mathematical properties of the equation (Wu and Niemunis, 1996). In this way, the defining features of granular soil behaviour, nonlinearity, irreversibility, pycnotropy (density dependence), barotropy (pressure dependence), and the critical state, can be represented with a relatively small number of physically meaningful parameters (Herle and Gudehus, 1999).

The aim of this chapter is to present, in an integrated manner, the hypoplastic constitutive models developed for cohesionless soils: their theoretical foundations, the von Wolffersdorff (1996) formulation that has become the reference model, the experimental determination of the model parameters, the intergranular strain extension developed for cyclic loading, and their applications in geotechnical engineering.

MECHANICAL BEHAVIOUR OF COHESIONLESS SOILS

The success of a constitutive model begins with a correct definition of the experimental behavioural features it is expected to represent. This section summarises the fundamental mechanical properties of cohesionless soils that underlie hypoplastic modelling, within the framework of observations obtained from triaxial compression and oedometer tests

(Kolymbas and Wu, 1990; Wu, 1992; Verdugo and Ishihara, 1996; Wichtmann and Triantafyllidis, 2016).

Stress–Strain Relationship

The stress–strain relationship of cohesionless soils is nonlinear from the very smallest strain levels and is markedly irreversible. Figure 1 shows the results of triaxial compression tests carried out at the same confining pressure on Karlsruhe sand specimens of different densities. In a dense specimen, the stress ratio reaches its peak value at an axial strain of a few per cent; as straining continues, the stress softens and falls to a residual (critical) level. In a loose specimen, no peak is observed; the deviatoric stress increases monotonically and approaches the same residual level asymptotically (Casagrande, 1936; Schofield and Wroth, 1968). The tangent stiffness decreases continuously with strain and drops to zero at failure; that is, the "elastic region" of the soil is practically negligible (Atkinson et al., 1990; Kolymbas, 2000). The irreversible nature of the behaviour is clearly seen in loading–unloading cycles: the slope of the unloading curve is markedly steeper than that of the initial loading curve, and a permanent strain remains once the cycle is complete. The difference between the tangent stiffnesses in loading and unloading is the expression of the property known in the literature as incremental nonlinearity (Kolymbas, 2000; Ertek, 2020). This property means that the behaviour depends on the *direction* of the strain rate and cannot be represented by linear (hypo)elastic equations; as discussed later, it is the starting point of the mathematical structure of hypoplasticity.

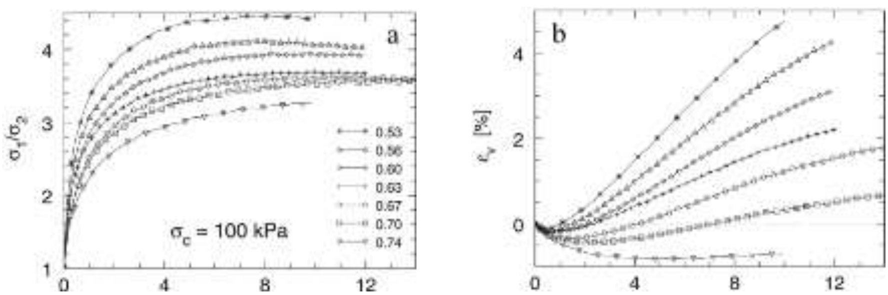

Figure 1: Results of triaxial compression tests on Karlsruhe sand of different densities at a confining pressure of 100 kPa: (a) stress ratio–axial strain; (b) volumetric strain–axial strain
Source: Kolymbas, 2016

Effect of Density and Initial Void Ratio

Specimens of the same sand at different densities behave qualitatively differently at the same confining pressure: dense specimens exhibit a high peak friction angle and dilation, whereas loose specimens exhibit low strength and contraction. This dependence of behaviour on void ratio (density) was termed pycnotropy by Kolymbas (Kolymbas, 1991); the family of tests in Figure 1 is a typical example of this phenomenon. The decisive consequence of pycnotropy is that the peak friction angle is not a material constant but a function of density and stress level; the only friction angle that qualifies as a material constant is the critical-state friction angle φ_c reached at large strains (Schanz and Vermeer, 1996; Herle and Gudehus, 1999).

Effect of Stress Level (Barotropy)

Soil behaviour also depends on the stress level: as the confining pressure increases, the stiffness increases in absolute terms, but the stress-normalised peak strength ratio (q/σ_3, where $q = \sigma_1 - \sigma_3$ is the deviatoric stress) and the tendency to dilate decrease (Kolymbas and Wu, 1990; Wu, 1992). This dependence is termed barotropy (Kolymbas, 1991). The increase of stiffness with mean stress is not linear; experimental findings show that the stiffness increases according to a power law of the form σ^n $(0 < n < 1)$ (Kolymbas, 2000). At high stress levels, the behaviours of dense and loose specimens approach one another; at very high pressures even dense specimens behave contractively (Wu et al., 1996). Barotropy and pycnotropy are not independent of each other: the quantity governing the behaviour is the position of the current void ratio relative to the critical void ratio at that pressure level.

Contraction and Dilatancy

Volume change during shearing is a distinctive feature of granular soils (the volumetric curves in Figure 1b). A specimen denser than the critical void ratio first contracts slightly at the onset of shearing and then dilates, as the grains ride over one another and rearrange; a specimen looser than the critical state, by contrast, contracts throughout shearing (Casagrande, 1936). The rate of dilation is highest near the peak stress and drops to zero as straining continues. In water-saturated soils under undrained conditions, this tendency for volume change is converted into pore-water pressure: a contractive tendency generates positive pore-water pressure and thereby reduces the effective stress; this mechanism also underlies liquefaction (Verdugo and Ishihara, 1996; Fuentes et al., 2020). From the standpoint of a constitutive model, the critical requirement is that the contraction/dilation transition be reproduced correctly as a function of density and stress level, without defining a separate dilatancy rule.

Critical State

Under sufficiently large monotonic shearing, all specimens, irrespective of their initial density, reach an asymptotic state in which continued straining takes place at constant stress and constant volume. This state, introduced by Casagrande (1936) through the concept of the critical void ratio and systematised within critical-state soil mechanics by Roscoe et al. (1958) and Schofield and Wroth (1968), is defined by the $q = Mp'$ line (p′: mean effective stress) and the critical-state line (CSL) in the e–lnp' plane. The critical void ratio e_c is not a material constant; it decreases with the mean effective stress. In the p–e diagram shown in Figure 2, specimens whose current state lies above the CSL (loose) approach the critical state by contracting, while those lying below it (dense) approach it by dilating (Li and Wang, 1998). The tests carried out by Verdugo and Ishihara (1996) on Toyoura sand showed that drained and undrained paths converge to the same curve at large strains in e–q–p' space, thereby supporting the path independence of the critical state.

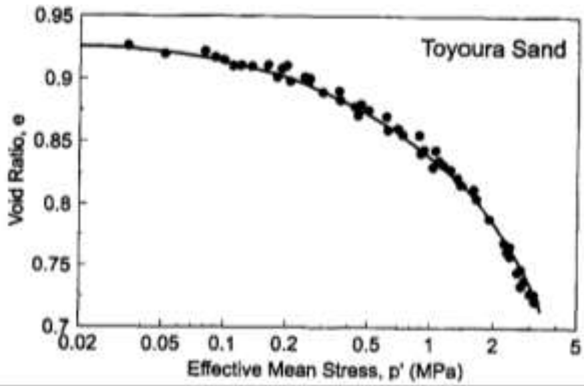

Figure 2: Representation of the critical-state line in the p–e plane
Source: Li and Wang (1998)

Cyclic Loading Behaviour and Small-Strain Stiffness

Under cyclic and dynamic loads (earthquakes, waves, traffic, machine foundations), cohesionless soils develop small but cumulative permanent strains in each cycle; under undrained conditions, pore-water pressure accumulates from cycle to cycle (Niemunis et al., 2005; Wichtmann and Triantafyllidis, 2016). In the small-strain region ($\varepsilon < 10^{-5}$), the soil exhibits an approximately elastic stiffness 3–10 times higher than at large strains; the stiffness decreases in the form of a characteristic S-curve as the strain amplitude increases (Atkinson et al., 1990). Upon a sudden change in loading direction (for example, a 180° reversal), the stiffness jumps back to its small-strain value and decreases again as straining proceeds. This effect of deformation history—the remembering of the direction of the most recent stress path—is the key to a realistic modelling of cyclic behaviour and constitutes the experimental basis of the intergranular strain concept (Niemunis and Herle, 1997).

Stress-Path Dependence and Proportional Paths

Granular soil behaviour is path-dependent: the stress state reached depends not only on the current strain but on the entire path followed. Nevertheless, the true triaxial tests of Goldscheider (1976) revealed a strong regularity within this path dependence. Known as proportional paths, this regularity is summarised by two rules: (i) proportional strain paths (with constant component ratios) applied from a stress-free (or very-low-stress) initial state produce proportional stress paths; (ii) proportional strain paths started from a stressed state approach asymptotically the proportional stress paths that would be obtained from the stress-free state (Goldscheider, 1976; Kolymbas, 2012; Ertek, 2020). The settling of the stress ratio at the constant value K_0 in oedometric compression is a well-known special case of these rules. Proportional paths constitute the experimental justification for the stress-homogeneity constraint of the hypoplastic equation and are also the point of departure for the Barodesy theory of Kolymbas (2012). When these behavioural features are considered together, the minimum requirements for a constitutive model of cohesionless soils may be listed as follows: (i) a nonlinear and irreversible stress–strain relationship; (ii) representation of pycnotropy and barotropy with a single parameter set; (iii) natural reproduction of the contraction/dilation transition and of the critical state; (iv) peak and softening behaviour; (v) small-strain stiffness and deformation-history effects; and (vi) compatibility with proportional paths. The following sections present the mathematical structure by which hypoplasticity meets these requirements.

FUNDAMENTALS OF HYPOPLASTICITY THEORY

The Concept of Hypoplasticity and Its Historical Development

Hypoplasticity is a family of rate-type, incrementally nonlinear constitutive theories that describe the soil with a small number of state variables, such as the current stress state and (in their extended forms) the void ratio. The distinguishing feature of the theory is that the distinction between loading and unloading is provided internally by the nonlinear structure of the equation in the strain rate, rather than by external definitions such as a yield surface and a loading criterion (Kolymbas, 1991; Wu and Kolymbas, 1990). The term “hypoplasticity” was proposed by Kolymbas and Wu for this class of models, whose tangent stiffness is a continuous function of the strain rate (Niemunis, 2003). The development of the theory can be summarised as follows. The first rate-type nonlinear tensorial equation was proposed by Kolymbas (1977), and the general framework of the theory matured with Kolymbas (1985, 1991). Wu (1992) and Wu and Bauer (1994) made the theory operational by presenting a lean four-term model; Wu et al.

(1996) carried the critical-state concept into the model by adding the void ratio as a state variable. The year 1996 was a turning point for hypoplasticity: Gudehus (1996) published a comprehensive general form incorporating barotropy and pycnotropy factors, Bauer (1996) published the compression law giving the variation of the limiting void ratios with pressure, and von Wolffersdorff (1996) published a formulation incorporating the Matsuoka–Nakai failure criterion as a predefined limit surface. The von Wolffersdorff (1996) model has become the reference model that comes to mind today when hypoplasticity is mentioned (Mašín, 2019). Niemunis and Herle (1997) added the concept of intergranular strain to remedy the shortcomings at small strains and under cyclic loading; Niemunis (2003) systematised the theory with methods for its visualisation and extension. Mašín (2005) extended hypoplasticity to clays, and Niemunis et al. (2005) developed the explicit high-cycle accumulation (HCA) model for large numbers of cycles. Kolymbas (2012) proposed the Barodesy theory founded on proportional paths, and Fuentes and Triantafyllidis (2015) proposed the ISA approach, which defines a yield surface in intergranular strain space. Recent developments include new-generation basic models (Wu et al., 2017), extensions targeting the fabric effect and multidirectional shearing (Liao and Yang, 2021, 2022), models accounting for grain crushing (Cui et al., 2024), and improved intergranular strain formulations for repetitive cycles (Duque et al., 2020).

Absence of a Yield Surface and Plastic Potential

In classical elastoplasticity, the constitutive relationship has a dual (bilinear) structure: if the stress state is inside the yield surface, the behaviour is elastic, whereas if it is on the surface, the behaviour is elastoplastic and the strain rate is decomposed into elastic and plastic components. This structure requires the separate definition of a yield function, a plastic potential, a flow rule, a hardening law, and a consistency condition (Niemunis, 2003; Ertek, 2020). In granular soils, however, a "fully elastic" stress region is not observed experimentally; plastic strains occur even under the smallest stress changes (Kolymbas, 2000).

Hypoplasticity abandons this dual structure entirely: a single equation is valid for all stress states and all strain directions. The difference in stiffness between loading and unloading arises spontaneously from the sign sensitivity of the nonlinear term that depends on the norm of the strain rate ($\| D \|$). The failure surface, in turn, is not a boundary imposed on the model from outside but a *consequence* of the equation: at certain stress states, the condition that the stress rate vanishes for a particular strain direction ($\overset{\circ}{\sigma} = 0$) defines a surface in stress space, and the flow direction corresponding to the flow rule is derived from the same condition (Wu and Niemunis, 1996). The practical counterpart of this approach is fewer conceptual building blocks, a leaner formulation, and the ability to calibrate the entire model with a small number of parameters.

The Rate-Type Constitutive Equation and Fundamental Constraints

In its most general form, the hypoplastic constitutive equation is a tensorial function relating the objective stress rate to the stress state and the strain rate:

$$\overset{\circ}{\sigma} = \mathrm{H}(\sigma, \mathrm{D}) \tag{1}$$

Here σ is the effective Cauchy stress tensor (compression taken as negative) and D is the strain-rate (stretching) tensor. Three fundamental constraints, arising from the general features of granular soil behaviour, are imposed on the function H (Wu and Kolymbas, 1990; Wu and Bauer, 1994):

(i) Rate independence. The behaviour of dry or drained granular soils does not involve viscous effects within the range of loading rates encountered in practice. For this to hold, H must be positively homogeneous of the first degree in D:

$$\mathrm{H}(\sigma, \lambda \mathrm{D}) = \lambda\, \mathrm{H}(\sigma, \mathrm{D}), \qquad \lambda > 0 \tag{2}$$

This condition does not require directional differentiability: H may be a function that is non-differentiable (has a corner) at the point $\mathrm{D} = 0$, and incremental nonlinearity arises precisely from this corner.

(ii) Homogeneity in stress. For consistency with the proportional-path rules of Goldscheider (1976), H is required to be homogeneous in stress:

$$\mathrm{H}(\lambda\sigma, \mathrm{D}) = \lambda^{m}\, \mathrm{H}(\sigma, \mathrm{D}) \tag{3}$$

In the case of first-degree homogeneity, the stiffness becomes directly proportional to the stress level; the experimentally observed dependence of the type σ^n $(n < 1)$ is provided by the barotropy factor (Gudehus, 1996).

(iii) Objectivity (material frame indifference). The constitutive equation must not be affected by a change of observer:

$$\mathrm{H}(\mathrm{Q}\sigma\mathrm{Q}^T, \mathrm{Q}\mathrm{D}\mathrm{Q}^T) = \mathrm{Q}\,\mathrm{H}(\sigma, \mathrm{D})\,\mathrm{Q}^T \tag{4}$$

Here Q is any orthogonal rotation tensor. This condition requires H to be an isotropic tensor function and, by the representation theorem, H can be written as a linear combination, with coefficients depending on the joint invariants, of a finite number of tensorial generators formed from σ, D and their products (Ertek, 2020). The natural (depositional) anisotropy of the soil is thereby neglected within this framework; for recent extensions targeting anisotropy, fabric-tensor formulations of the type of Liao and Yang (2021) and Yang et al. (2020) are employed.

Objective Stress Rate

In problems involving large deformations, the material time derivative of the stress tensor $\dot{\sigma}$ is not objective; rigid-body rotations produce spurious stress rates. In hypoplasticity, therefore, the Jaumann–Zaremba objective rate is used on the left-hand side of Equation (1):

$$\overset{\circ}{\sigma} = \dot{\sigma} + \sigma W - W \sigma \quad (5)$$

Here W is the antisymmetric part of the velocity gradient (the spin tensor) and D is its symmetric part (Bayraktaroğlu, 2019). In element tests and small-deformation analyses, where rotation can be neglected, one may take $W = 0$ and hence $\overset{\circ}{\sigma} = \dot{\sigma}$; in finite-element applications, the transformation between the objective rate and the material derivative is carried out by the software within the large-deformation formulation employed.

Physical Meaning of the Linear and Nonlinear Terms

Under the above constraints, the hypoplastic equation reduces in practice to a special two-term structure (Wu, 1992; Wu and Kolymbas, 1990):

$$\overset{\circ}{\sigma} = L(\sigma){:}\, D + N(\sigma) \;\| D \| \quad (6)$$

Here L is a fourth-order stiffness tensor and N is a second-order tensor. The first term is linear in D and, taken alone, corresponds to Truesdell's hypoelasticity; the second term is nonlinear through $\| D \|$ and carries all of the irreversibility content of the theory. When D changes direction ($D \rightarrow -D$), the linear term changes sign, but the $N \| D \|$ term does not; the difference between the loading and unloading stiffnesses is thereby produced within a single equation. By a rough analogy, the linear term is the "constructive" (reversible) component and the nonlinear term is the "destructive" (energy-dissipating, relaxing) component; the relative magnitude of the two terms determines the contractive–dilative tendency and the distance to failure (Wu et al., 1996). The most instructive visualisation of this structure is the response envelopes proposed by Gudehus (1979). At a given stress state σ_0, the locus of the tips of the stress rates computed for all unit-norm strain-rate directions is plotted. In a hypoelastic equation ($N = 0$) this envelope is an ellipse centred at σ_0; D and $-D$ produce opposite responses of equal magnitude. In the hypoplastic equation, by contrast, the $N \| D \|$ term shifts the envelope by a constant vector independent of direction: as seen in Figure 3, the envelope is an ellipse displaced with respect to σ_0. As failure is approached, the envelope becomes positioned so as to touch the point σ_0; the stiffness drops to zero for at least one strain direction. The cases in which the envelope cannot enclose σ_0 correspond to unreachable stress states and lead to the concept of the bound surface enclosing all attainable states (Wu and Kolymbas, 1990). Whereas the response envelopes of elastoplastic models take angular/discontinuous forms on the yield surface, the smooth and convex character of the hypoplastic envelopes is regarded as an advantage of the theory that is consistent with experimental findings (Ertek, 2020).

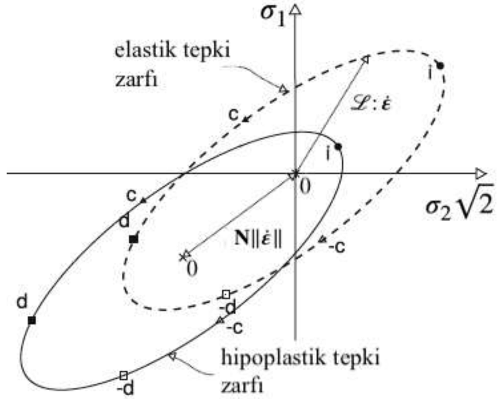

Figure 3: Hypoelastic and hypoplastic response envelopes
Source: Mašín (2019)

HYPOPLASTIC MODEL FOR COHESIONLESS SOILS

This section presents in full the von Wolffersdorff (1996) formulation, adopted as the reference model for cohesionless soils, with all its components, and shows how the model reproduces the behavioural features discussed in the previous section, using validation figures compiled from the literature. The model combines the general framework of Gudehus (1996), the compression law of Bauer (1996), and the Matsuoka–Nakai (1974) failure criterion in a single formulation.

Basic Model Equations

The general hypoplastic equation, in which the void ratio is added as a state variable, was proposed by Gudehus (1996) in the following form:

$$\mathring{\sigma} = f_s[\,\mathsf{L}(\hat{\sigma}) : \mathsf{D} + f_d\,\mathsf{N}(\hat{\sigma})\ \|\,\mathsf{D}\,\|\,] \qquad (7)$$

Here f_s is the barotropy (stiffness) factor and f_d is the pycnotropy factor; both are scalar functions of the stress level and the void ratio. von Wolffersdorff (1996) derived the tensors L and N such that the failure surface for $f_d = 1$ coincides exactly with the Matsuoka–Nakai condition:

$$\mathsf{L} = \frac{1}{\hat{\sigma}:\hat{\sigma}}\left(F^2\,\mathsf{I} + a^2\,\hat{\sigma}\otimes\hat{\sigma}\right), \qquad \mathsf{N} = \frac{F\,a}{\hat{\sigma}:\hat{\sigma}}\left(\hat{\sigma} + \hat{\sigma}^*\right) \quad (8)$$

Here $\hat{\sigma} = \sigma/\operatorname{tr}\sigma$ is the normalised stress, $\hat{\sigma}^* = \hat{\sigma} - 1/3\,1$ is the dimensionless stress deviator, and I is the fourth-order unit tensor (von Wolffersdorff, 1996; Liao and Yang, 2022; Cui et al., 2024). The scalar a links the critical-state friction angle to the model:

$$a = \frac{\sqrt{3}\,(3-\sin\varphi_c)}{2\sqrt{2}\,\sin\varphi_c} \qquad (9)$$

The coefficient F is the Lode-angle function that produces the Matsuoka–Nakai form in the deviatoric plane:

$$F = \sqrt{\frac{1}{8}\tan^2\psi + \frac{2-\tan^2\psi}{2+\sqrt{2}\tan\psi\cos3\theta}} - \frac{\tan\psi}{2\sqrt{2}} \tag{10}$$

$$\tan\psi = \sqrt{3}\ \parallel \hat{\boldsymbol{\sigma}}^* \parallel, \qquad \cos3\theta = -\sqrt{6}\,\frac{\mathrm{tr}(\hat{\boldsymbol{\sigma}}^*\cdot\hat{\boldsymbol{\sigma}}^*\cdot\hat{\boldsymbol{\sigma}}^*)}{[\hat{\boldsymbol{\sigma}}^*:\hat{\boldsymbol{\sigma}}^*]^{3/2}} \tag{11}$$

In axisymmetric (triaxial) stress states, $F = 1$ (Bayraktaroğlu, 2019). The evolution of the void ratio follows directly from mass conservation:

$$\dot{e} = (1+e)\,\mathrm{tr}\,\mathrm{D} \tag{12}$$

Critical State and Failure Surface

In the model, the critical state is represented by the simultaneous satisfaction of the conditions $e = e_c$ and, at the critical stress ratio, $\mathring{\sigma} = 0$ and $\mathrm{tr}\,\mathrm{D} = 0$. In a model of the structure of Equation (6), the failure state is characterised by the condition $\parallel \mathsf{L}^{-1}:\mathrm{N} \parallel = 1$, with the flow direction $\vec{\mathrm{B}} = -\mathsf{L}^{-1}:\mathrm{N}$; the surface swept by this condition in stress space is the failure surface of the model (Wu and Niemunis, 1996). In the von Wolffersdorff (1996) formulation this surface coincides, by construction, with the Matsuoka–Nakai (1974) condition. Figure 4 shows the Matsuoka–Nakai surface in the deviatoric (π) plane and in three-dimensional principal stress space. The criterion coincides with the Mohr–Coulomb hexagon in triaxial compression and triaxial extension; at intermediate Lode angles its corner-free, convex form is both more consistent with experimental data and free of the derivative discontinuities that hamper numerical implementation (Matsuoka and Nakai, 1974; von Wolffersdorff, 1996). For the bound surface, which in hypoplastic models encloses the failure surface that stress paths can somewhat exceed and which bounds all attainable states, the reader is referred to Ertek (2020) and Niemunis (2003).

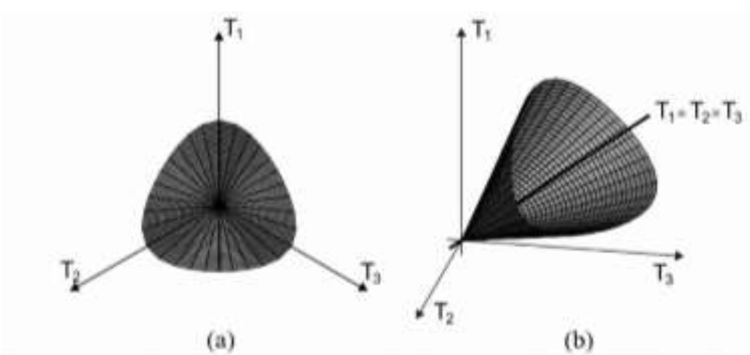

Figure 4: Matsuoka–Nakai failure criterion (a) in deviatoric plane (b) in 3D principal stress space
Source: Matsuoka and Nakai (1974)

Limiting Void Ratios

The backbone of the model's grasp of state is three characteristic void ratios (Gudehus, 1996): e_i, representing the loosest state attainable under isotropic compression; the critical void ratio e_c; and e_d, representing the densest state attainable by small-amplitude cyclic shearing. The Bauer (1996) compression law assumes that all three decrease with mean stress in the same manner:

$$\frac{e_i}{e_{i0}} = \frac{e_c}{e_{c0}} = \frac{e_d}{e_{d0}} = \exp\left[-\left(\frac{3p_s}{h_s}\right)^n\right] \tag{13}$$

Here $p_s = -\mathrm{tr}\,\sigma/3$ is the mean effective stress and e_{i0}, e_{c0}, e_{d0} are the reference values at zero pressure. Figure 5 shows the variation of these three curves with stress. The regions $e > e_i$ and $e < e_d$ are physically impossible; the current state of the soil always lies in the band $e_d \leq e \leq e_i$, and the position of e relative to e_c determines whether the behaviour will be contractive or dilative. This structure is a pressure-dependent, consistent generalisation of the concept of "relative density": a sand at the same void ratio may behave as dense (dilative) at low pressure and as loose (contractive) at high pressure.

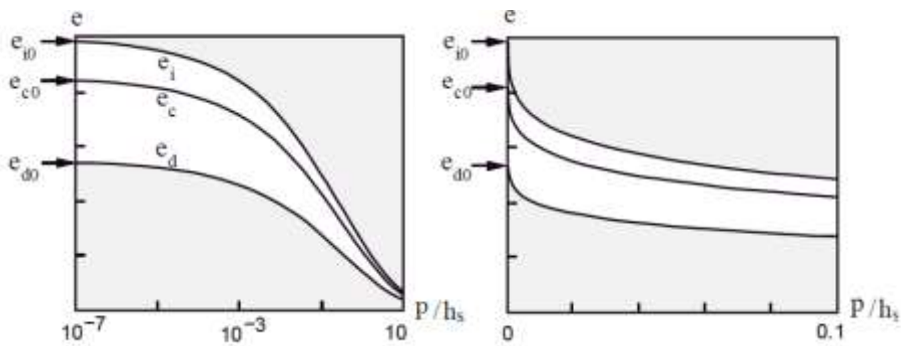

Figure 5: Relation between limiting void ratios and mean effective stress
Source: Herle and Gudehus (1999)

Pressure and Density Dependence: The f_s and f_d Factors

Barotropy and pycnotropy are represented by the two scalar factors in Equation (7). The pycnotropy factor measures the position of the current void ratio relative to the limiting void ratios:

$$f_d = \left(\frac{e-e_d}{e_c-e_d}\right)^\alpha \tag{14}$$

At the critical state ($e = e_c$), $f_d = 1$; at the densest state ($e = e_d$), $f_d = 0$. Because f_d scales the nonlinear ("destructive") term, in dense soils ($f_d < 1$) the peak strength rises above the critical value and dilation develops, whereas in loose soils ($f_d > 1$) the behaviour is contractive. The stiffness (barotropy) factor has the following form (von Wolffersdorff, 1996; Bayraktaroğlu, 2019):

$$f_s = \frac{h_s}{n}\left(\frac{e_i}{e}\right)^\beta \frac{1+e_i}{e_i}\left(\frac{3p_s}{h_s}\right)^{1-n}\left[3 + a^2 - a\sqrt{3}\left(\frac{e_{i0}-e_{d0}}{e_{c0}-e_{d0}}\right)^\alpha\right]^{-1} \tag{15}$$

f_s represents together the exponential increase of stiffness with stress level (through the ${p_s}^{1-n}$ factor) and its increase with density (through the $(e_i/e)^\beta$ factor). Equations (13)–(15) together determine the oedometric compression behaviour of the model: the initial loading curve follows the form of the Bauer law; the stiffness is markedly higher in unloading, and a permanent decrease in void ratio (permanent settlement) remains at the end of a loading–unloading cycle (Bauer, 1996). The ability of the model to represent pycnotropy and barotropy with a single parameter set was demonstrated by von Wolffersdorff (1996) on Hochstetten sand: Figure 6 shows a comparison of drained triaxial tests under different density and stress conditions with model simulations performed using a single parameter set. The dense specimen exhibits a pronounced peak and softening together with strong dilation, whereas the loose specimen exhibits peak-free, contractive hardening behaviour; as the confining pressure increases, the normalised peak strength and dilation decrease systematically. The reproduction with a single set of this range of behaviour, which in classical models requires separate parameter sets (e.g. a different friction and dilation angle for each density), is among the greatest strengths of the model.

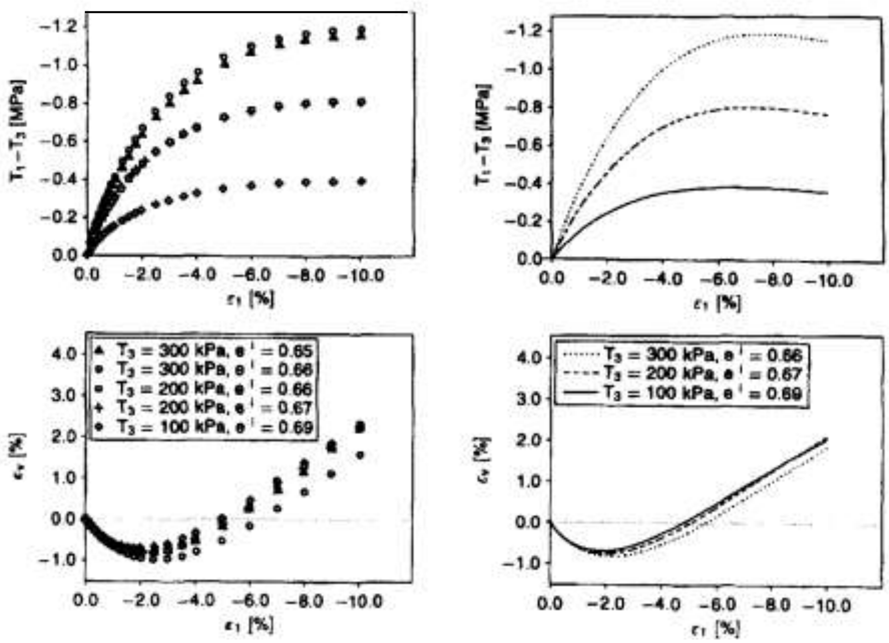

Figure 6: Triaxial test and analysis results for Hochstetten sand
Source: von Wolffersdorff (1996)

In the model, the contraction–dilation transition is produced without a separate dilatancy rule, as a function of the density–pressure state through f_d. This mechanism is integrated with the critical-state concept: the mobilised friction angles of specimens with different initial void ratios converge at large strain to a common value φ_c, and their state paths converge in the e–p_s plane to the critical-state line defined by Equation (13); dense specimens approach the critical state from above by softening after the peak, and loose specimens approach it from below by hardening (Wu et al., 1996).

MODEL PARAMETERS

The von Wolffersdorff (1996) hypoplastic model is defined by eight material parameters, all of which can be determined from standard or near-standard laboratory tests; none of these parameters is a "fitting" coefficient specific to a particular stress path. The systematic relationships between granulometric quantities (grain shape, distribution, mineralogy) and the parameters were established by Herle and Gudehus (1999); these relationships guarantee the physical meaningfulness of the parameters and their transferability to different sands. These eight parameters and their physical meanings can be summarised as follows. The critical-state friction angle φ_c [°] is the material constant governing the residual strength reached at large strain and generally lies in the range 28–36° for sands. The compression behaviour is controlled by two parameters: the granular hardness h_s [MPa], the only parameter carrying stress dimension and setting the stress scale of the compression curve, which may vary over a very wide range of roughly 100–30,000 MPa depending on the type of sand; and the dimensionless pressure-sensitivity exponent n, which determines the curvature of the compression curve and the rate of increase of stiffness with pressure and is typically between 0.15 and 0.60. The basis of the model's grasp of state is formed by three reference void ratios defined at zero pressure: e_{d0} (≈ e_{min}; typically 0.4–0.7), representing the densest state; the critical void ratio e_{c0} (≈ e_{max}; typically 0.7–1.1); and e_{i0} (≈ 1.1–1.3 e_{max}; typically 0.9–1.3), representing the isotropic loosest state. Finally, two dimensionless exponents control the density dependence of the behaviour: the pycnotropy exponent α determines the variation of peak strength and dilation with density (typically 0.05–0.30), and the stiffness exponent β controls the variation of stiffness with density (typically 1.0–3.0) (von Wolffersdorff, 1996; Herle and Gudehus, 1999; Bayraktaroğlu, 2019).

Critical-State Friction Angle, φ_c

φ_c enters the model through Equation (9) and controls both the size of the failure surface and the flow direction. It has the character of a material constant: it is independent of density and stress level (as long as grain crushing does not develop) (Schanz and Vermeer, 1996). In calcareous sands, where grain crushing is pronounced, φ_c has been shown to decrease as crushing progresses and has been incorporated into the model through functions dependent on a crushing index (Cui et al., 2024).

Granular Hardness (h_s) and Pressure-Sensitivity Exponent (n)

h_s is the only parameter of the model carrying stress dimension and has the character of a reference pressure representing the compressibility of the grain skeleton (not of the individual grains); n, in turn, controls the curvature of the compression curve (Bauer, 1996; Herle and Gudehus, 1999). As shown in Figure 7, the curvature of the compression curve increases as n increases; as h_s increases, the curve shifts to the right (a stiffer skeleton).

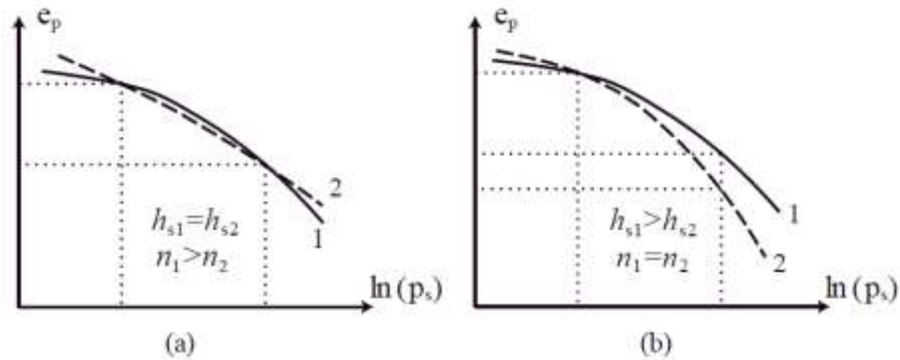

Figure 7: Influence of exponent n (a) and granulate hardness h_s (b) on compression curve

Source: Herle and Gudehus (1999)

Reference Void Ratios: e_{d0}, e_{c0}, e_{i0}

The three reference void ratios are the initial values, at zero pressure, of the limiting-void-ratio curves (Figure 5). The practical approximations proposed by Herle and Gudehus (1999) are as follows: $e_{d0} \approx e_{min}$ (standard densest-packing index test); $e_{c0} \approx e_{max}$ (loosest-packing index test); $e_{i0} \approx (1{,}1\text{–}1{,}3)\, e_{max}$. The reason e_{i0} is larger than e_{max} is that the isotropic loosest state (grains arranged in contact in a gravity-free environment such that the contact force is zero) cannot be obtained by the standard test under gravity; a geometric evaluation based on equal-sphere packing gives $e_{i0} \approx 1{,}2\, e_{max}$ (Bayraktaroğlu, 2019). For the zero-pressure extension of the critical void ratio, e_{max} has been shown on various sands to be a good approximation (Herle, 1997).

Pycnotropy Exponent, α

α controls the transition from peak to critical state, the increase of the peak friction angle with relative density, and the intensity of dilation (Equation 14). Small values of α produce a weak peak and a smooth transition, while large values produce a sharp peak and intense softening; the control of the peak-to-critical transition by α is shown in Figure 8.

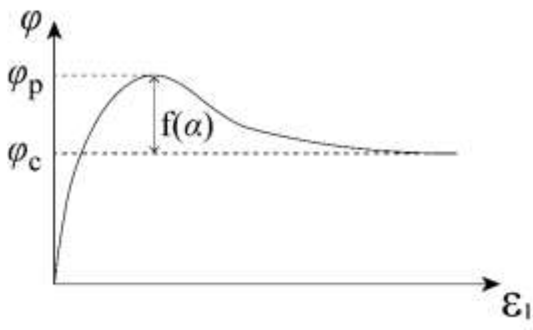

Figure 8: Transition from peak to critical state with exponent α

Source: Bayraktaroğlu (2019)

Stiffness Exponent, β

β controls the variation of stiffness with void ratio through $f_s \propto (e_i/e)^{\beta}$: at the same stress a dense specimen is stiffer than a loose one. For the loose state, since $e \rightarrow e_i$ the effect of the factor vanishes; therefore taking β≈1 in loose soils is a common and sufficient approximation (Herle and Gudehus, 1999). The parameter sets published in the literature for different sands clearly reveal the sensitivity of these eight parameters to granulometry. When the values reported for sands such as Hochstetten, Karlsruhe, Fraser River, Baskarp, and Monterey and for a well-graded sand are compared, the critical-state friction angle clusters in a narrow band for most quartz sands (approximately 32.5–35°), while the granular hardness h_s can vary by several orders of magnitude, from the order of tens of MPa (≈40 MPa for the well-graded sand) to tens of thousands of MPa (≈18,000 MPa for Baskarp sand). The pressure-sensitivity exponent n typically lies in the range 0.25–0.57, and the pycnotropy exponent α in the range 0.10–0.25. The three reference void ratios, following the densest/loosest packing values of the sand concerned, vary with gradation (approximately e_{d0} = 0.50–0.67, e_{c0} = 0.85–1.05, e_{i0} = 0.98–1.21). The stiffness exponent β was taken as 1.0 (at most 1.12) in almost all of the sets examined, which supports the assumption β≈1 above. The values in question can be compiled from various sources (Niemunis and Herle, 1997; Holler, 2006; Sturm, 2011; Liao and Yang, 2022; Bayraktaroğlu, 2019).

EXPERIMENTAL DETERMINATION OF THE PARAMETERS

The systematics of parameter determination were established by Herle and Gudehus (1999). Each of the eight parameters is determined by relatively simple tests that can be carried out in most geotechnical laboratories. The critical-state friction angle φ_c is obtained from the angle-of-repose (heap) test on dry, loosely poured material, or alternatively from a drained triaxial test on a loose specimen. The granular hardness h_s and the pressure-sensitivity exponent n are determined from an oedometer (or isotropic compression) test on an initially very loose, dry specimen. The three reference void ratios e_{d0}, e_{c0}, and e_{i0} are estimated from the standard densest/loosest (e_{min}/e_{max}) index tests. The pycnotropy exponent α is computed from the peak point of a drained triaxial compression test on a dense specimen; the stiffness exponent β is found from two drained triaxial compression (or oedometer) tests on two specimens of different density. The following subsections present these determination methods in detail; in the formulae, for triaxial conditions, T_1 denotes the vertical (axial) and $T_2 = T_3$ the lateral principal stresses, and D_1 and D_2 the corresponding strain rates.

Critical-State Friction Angle: The Angle-of-Repose Test

The critical state cannot always be reliably measured in a triaxial test, because homogeneous deformation cannot be sustained up to large strains in the laboratory. Herle and Gudehus (1999) showed on various sands that the angle of repose (φ_{rep}) of the cone formed by dry, loosely poured material is very close to the critical-state friction angle, and they proposed the approximation $\varphi_c \approx \varphi_{rep}$; the test technique was standardised by Miura et al. (1997). The calculation is made from the geometry of the heap through the relation $\tan\varphi_{rep} \cong 2H/D$ (H: cone height, D: base diameter). Bayraktaroğlu (2019) developed a measurement method that eliminates operator subjectivity, based on photographing the cone from different angles and fitting the boundary line by image processing, and obtained $\varphi_c = 33{,}45°$ with a standard deviation of 0.01° from the average of three tests.

Oedometer Tests: h_s and n

h_s and n are determined from the oedometric (or isotropic) compression curve of an initially very loosely prepared, dry specimen. The loose-specimen condition is intended to start as close as possible to the e_i curve followed by Equation (13) and to ensure the normally consolidated state in which the Jaky relation ($K_0 = 1 - \sin\varphi_c$) holds (Bayraktaroğlu, 2019). Using the void ratios (e_{p1}, e_{p2}) and compression indices (C_{c1}, C_{c2}) at two points (p_{s1}, p_{s2}) chosen on the compression curve (Herle, 1997; Herle and Gudehus, 1999):

$$n = \frac{\ln\left(\frac{e_{p1}C_{c2}}{e_{p2}C_{c1}}\right)}{\ln\left(\frac{p_{s2}}{p_{s1}}\right)}, \qquad h_s = 3\,p_s\left(\frac{n\,e_p}{C_c}\right)^{1/n} \tag{16}$$

is calculated; here $p_s = (T_1 + 2T_2)/3$ is found by taking $T_2 = K_0 T_1$ in the oedometer, and for h_s the values C_c, e_p are read at a point within the range $[p_{s1}, p_{s2}]$. In practice, deriving the variation of C_c with stress by fitting a continuous curve to the test data and taking the range average of h_s reduces the subjectivity arising from point selection (Bayraktaroğlu, 2019).

Index Tests: e_{d0}*,* e_{c0}*,* e_{i0}

For the reference void ratios, the standard densest/loosest packing tests are sufficient: $e_{d0} \approx e_{min}$, $e_{c0} \approx e_{max}$, $e_{i0} \approx 1{,}15\, e_{max}$ (Herle, 1997; Herle and Gudehus, 1999). Theoretically, e_{d0} corresponds to the densest state reached under small-amplitude cyclic shearing and is somewhat smaller than e_{min} (Youd, 1972); in practice this difference is neglected. Bayraktaroğlu (2019) reported the low scatter of the values obtained for the tested sand with different standards (6 tests for e_{max}, 4 tests for e_{min}) and used the averages $e_{max} = 0{,}918$, $e_{min} = 0{,}629$.

Drained Triaxial Tests: α *and* β

α is determined from the peak point of a drained triaxial compression test on a dense specimen. A closed-form expression is obtained by substituting the peak condition ($\dot{T}_1 = 0$) into the model equation reduced to triaxial form (Herle and Gudehus, 1999; Cui et al., 2024):

$$\alpha = \frac{\ln\left[6\,\frac{\left(2+K_p\right)^2 + a^2 K_p\,(K_p - 1 - \tan\nu_p)}{a\,(2+K_p)(5K_p-2)\sqrt{4+2\left(1+\tan\nu_p\right)^2}}\right]}{\ln\left[\frac{e-e_d}{e_c-e_d}\right]} \tag{17}$$

Here $K_p = \left(1+\sin\varphi_p\right)/\left(1-\sin\varphi_p\right)$ is the peak stress ratio, $\tan\nu_p = -(D_1 + 2D_2)/D_1$ is the measure of dilation at the peak, and e is the void ratio at the peak; e_c, e_d are calculated from Equation (13) for the mean stress at the peak. β, in turn, is determined from the ratio E_1, E_2 of the initial (or same-stress-ratio) stiffnesses of two specimens of different density at the same mean stress (Herle and Gudehus, 1999; Bayraktaroğlu, 2019):

$$\beta = \frac{\ln\left[\frac{E_2}{E_1}\left(\frac{3+a^2-f_{d1}\,a\sqrt{3}}{3+a^2-f_{d2}\,a\sqrt{3}}\right)\right]}{\ln\left(\frac{e_1}{e_2}\right)} \tag{18}$$

Since the effect of β remains negligible in loose specimens, the assumption $\beta = 1$ is common.

Calibration and Validation Procedure

The parameter set determined from the formulae should be regarded as an *initial* set. Good practice is to re-simulate each test at the element level with the determined parameters and to check the agreement between the measured and computed curves (Bayraktaroğlu, 2019). In case of disagreement, the parameters are adjusted within limits that preserve their physical meaning (calibration) and are verified with an independent test not used in the calibration (validation). For the element simulations, the freely available element-test drivers developed by Niemunis are widely used (Gudehus et al., 2008; Mašín, 2019). To make the process objective, Kadlíček et al. (2022) developed the ExCalibre algorithm, which automatically calibrates hypoplastic sand parameters from oedometer and triaxial test data and is provided online at soilmodels.com; the validation of the algorithm with different sands is reported in the same study. Automatic calibration reduces the sensitivity to the scope of the test set but does not relieve the user of the need to check the physical plausibility of the results: the suitability of the resulting h_s–n pair to the stress range of the problem and of the α–β pair to the density range must be checked in every case.

THE INTERGRANULAR STRAIN APPROACH

Limitations of the Basic Model at Small Strains

The basic hypoplastic model of the structure of Equation (7), although successful for monotonic loading, exhibits two systematic defects when the loading direction changes repeatedly (Niemunis and Herle, 1997). The first is that, in a small-amplitude closed strain cycle, the stress accumulates by an amount of the order of $2\mathrm{N} \parallel \Delta\varepsilon \parallel$ per cycle; in stress cycles, the strain increases by an almost constant amount in each cycle. Known as ratcheting, this excessive accumulation contradicts the accumulation observed in real soils, which decreases rapidly from cycle to cycle (Wichtmann and Triantafyllidis, 2016). The second is that the model predicts far too low a stiffness immediately after a change of direction; that is, the high, approximately elastic stiffness of the small-strain region cannot be reproduced. These defects arise because the state variables of the basic model (σ, e) carry no information about the most recent deformation *direction*: the model does not "remember" the path it has followed (Niemunis and Herle, 1997).

The Intergranular Strain Concept

Niemunis and Herle (1997) proposed a new, micromechanically inspired tensorial state variable to remedy this shortcoming: the intergranular strain δ (IS). Conceptually, δ represents the part of the macroscopic strain corresponding to the small and largely reversible deformation of the intergranular contact regions, rather than to the (permanent) rearrangement of the grain skeleton. The norm of δ is bounded by R: in monotonic deformation δ rapidly turns towards the direction of the strain rate and its norm saturates at R; upon a change of direction, the contact deformation is first reversed (the approximately elastic stage), and the skeleton rearrangement begins afterwards. By defining the normalised magnitude $\rho = \parallel \delta \parallel / R$ and the direction $\vec{\delta} = \delta / \parallel \delta \parallel$, the stiffness of the extended model is constructed by the following interpolation (Niemunis and Herle, 1997; Liao and Yang, 2022; Cui et al., 2024):

$$\mathcal{M} = [\rho^{\chi} m_T + (1-\rho^{\chi}) m_R]\mathsf{L} + \begin{cases} \rho^{\chi}(1-m_T)\left(\mathsf{L}:\vec{\delta}\right)\otimes\vec{\delta} + \rho^{\chi}\,\mathsf{N}\otimes\vec{\delta}, & \vec{\delta}:\mathrm{D} > 0 \\ \rho^{\chi}(m_R - m_T)\left(\mathsf{L}:\vec{\delta}\right)\otimes\vec{\delta}, & \vec{\delta}:\mathrm{D} \leq 0 \end{cases} \tag{19}$$

$$\mathring{\sigma} = \mathcal{M}:\mathrm{D} \tag{20}$$

The evolution of the intergranular strain is then defined by the following rule:

$$\dot{\delta} = \begin{cases} \left(\mathsf{I} - \vec{\delta}\otimes\vec{\delta}\,\rho^{\beta_r}\right):\mathrm{D}, & \vec{\delta}:\mathrm{D} > 0 \\ \mathrm{D}, & \vec{\delta}:\mathrm{D} \leq 0 \end{cases} \tag{21}$$

The three limiting cases of Equation (19) summarise the logic of the approach (Niemunis and Herle, 1997; Cui et al., 2024): (i) in monotonic deformation in the same direction as a saturated δ ($\rho = 1$, $\vec{\delta} \parallel \mathrm{D}$), the model reduces to the basic hypoplastic equation (6); (ii) upon a full reversal of direction ($\vec{\delta}:\mathrm{D} < 0$, 180°), the stiffness becomes $m_R\,\mathsf{L}$, the nonlinear term is deactivated, the behaviour is approximately elastic, and the stiffness is m_R times the monotonic value; (iii) upon a 90° turn of the path (neutral loading), the stiffness becomes $m_T\,\mathsf{L}$.

Small-Strain Stiffness and Hysteretic Behaviour

Immediately after a reversal of direction, the stiffness rises by the factor m_R; it remains approximately constant (an elastic plateau) until the strain exceeds the order of R, and then decays towards its monotonic value in the form of an S-curve controlled. This behaviour is consistent with the characteristics of experimental stiffness-decay curves (Atkinson et al., 1990; Niemunis and Herle, 1997). The decisive effect of the intergranular strain extension on cyclic loading is evident in undrained cyclic triaxial simulations: the basic model accumulates pore-water pressure at an unrealistically rapid rate and exhausts the initial effective stress within only a few cycles, producing ratcheting, whereas the extended model yields a more gradual accumulation consistent with experimental observations (Niemunis and Herle, 1997; Bayraktaroğlu, 2019). With respect to the real behaviour under cyclic loading, it is known that the accumulation of the IS model can be under-predicted under some conditions and over-predicted on some paths.

Additional Model Parameters and Their Determination

The extended model contains five additional parameters: R, m_R, m_T, β_r, and χ. R is the radius of the elastic-like region and its typical value is of the order of 10^{-4}. m_R is the stiffness multiplier after a 180° reversal; it can be estimated from the ratio of the small-strain shear modulus G_0 (from a bender-element or resonant-column test) to the monotonic stiffness. m_T is for a 90° turn and satisfies the condition $m_R > m_T > 1$; since its direct measurement is difficult, $m_T \approx m_R/2$ is usually taken (Niemunis and Herle, 1997; Bayraktaroğlu, 2019). β_r and χ control, respectively, the rate of evolution of δ and the rate of stiffness degradation, and are calibrated by fitting to the stiffness-decay curve. Because they require high-resolution local strain measurement, these five parameters are in practice mostly initialised from literature values and calibrated parametrically through simulations of cyclic tests. In the sets published for different sands, these values lie in the following ranges: R is mostly of the order of 10^{-5}–10^{-4}; m_R is about 2–8; m_T is about 1–6; β_r is typically 0.1–0.5; and the stiffness-degradation exponent χ is between 1 and 6 (Niemunis and Herle, 1997; Sturm, 2011; Liao and Yang, 2022; Bayraktaroğlu, 2019; Mašín, 2019).

Limitations and Recent Developments

The IS-augmented hypoplastic model, although it has become one of the standard tools for cyclic geotechnical problems, has well-documented limitations. Wichtmann et al. (2019) compared hypoplasticity+IS, Sanisand, and ISA models on a comprehensive monotonic and cyclic test database for Karlsruhe fine sand and showed that the IS model can systematically distort the accumulation rate over large numbers of cycles and the behaviour on certain stress paths. Liao and Yang (2022) revealed two fundamental defects of the model in undrained cyclic shearing: the effective-stress reduction stops at a level far from zero (a butterfly-shaped effective-stress path cannot be produced), and on circular/figure-of-eight multidirectional loading paths the condition $\vec{\delta}:\mathrm{D} < 0$ never occurs, so the pore-water pressure accumulates far too rapidly. The same study largely remedied these defects by adding a fabric variable inspired by Dafalias and Manzari (2004) and a new, bounding-surface-based unloading criterion. Wegener and Herle (2014) and Duque et al. (2020) proposed improvements to the IS formulation so that the accumulation remains realistic over repetitive cycles; Fuentes and Triantafyllidis (2015) developed the ISA family, which defines a yield surface in intergranular strain space, and Fuentes et al. (2020) developed the version of this family adapted to liquefaction analyses. For very large numbers of cycles ($N > 10^3$–10^7), the explicit HCA model (Niemunis et al., 2005), which gives the accumulation directly as a function of the number of cycles, is preferred over cycle-by-cycle (implicit) computation. For calcareous sands, where grain crushing is important, Cui et al. (2024) presented an extension that links the crushing index to the stress state and lets φ_c, the limiting void ratios, and α evolve with crushing. The effect of the fabric-variable extension proposed by Liao and Yang (2022) is seen in Figure 9: while the original IS model stops the effective-stress reduction at a level far from zero, the model augmented with the fabric effect and the new unloading criterion successfully reproduces the butterfly-shaped effective-stress path observed in the experiments and the mean effective stress approaching zero.

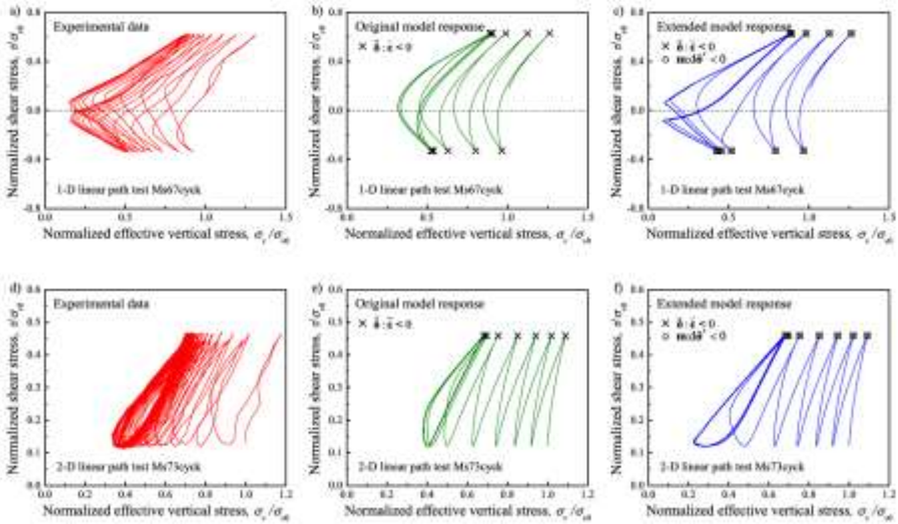

Figure 9: Comparison of experimental data and model simulations for effective stress path in (a–c) 1-D linear path test ms67cyck and (d–f) 2-D linear path test ms73cyck on Monterey No. 0/30 sand.
Source: Liao and Yang (2022)

GEOTECHNICAL ENGINEERING APPLICATIONS

Hypoplasticity is particularly powerful in problems where the prediction of deformation is critical and where the density–pressure state of the soil changes during the analysis. The fields of application are summarised below with representative examples from the literature.

Foundations and offshore structures: In settlement analyses of shallow and deep foundations, the model represents the variation of stiffness with stress and density automatically, and therefore provides an advantage over classical models, especially in scenarios involving loading and unloading. Sturm (2011) investigated, within a hypoplastic framework, the behaviour under cyclic horizontal loads of an innovative gravity-based foundation system for offshore wind turbines. Bayraktaroğlu (2019) carried out a three-dimensional coupled analysis of the same type of foundation system under 15 wave cycles, computing the pore-water pressure oscillations and differential settlements in the regions near the footing. For monopile and pile behaviour, Staubach et al. (2021) successfully back-analysed vibratory pile driving, including the pore-water pressure accumulation during driving, within a hydro-mechanically coupled CEL (Coupled Eulerian–Lagrangian) framework using hypoplasticity.

Excavations and retaining structures: In excavation problems, the representation of small-strain stiffness and stress-path dependence is decisive for a realistic computation of the settlement troughs behind the wall. Herle and Mayer (2009) computed the deformations of a deep underwater excavation in Berlin sand using hypoplastic parameters and compared them with measurements. von Wolffersdorff and Schwab (2009) analysed the behaviour of the Uelzen I ship lock (a chute structure) under long-term cyclic operating loads with the IS-augmented hypoplastic model, providing a validation of the model at real structural scale.

Tunnels: Tunnel excavation simultaneously mobilises strain ranges extending from very small to large and pronounced stress rotations. For shallow tunnels in sand, Hleibieh et al. (2014) computed the behaviour of a tunnel under earthquake loading with the IS-augmented hypoplastic model, in comparison with a centrifuge test; with clay hypoplasticity (Mašín, 2005), an extensive application literature on tunnel lining loads and surface settlements has developed (Mašín, 2019).

Slopes and embankments: The natural representation of softening and dilation enables a deformation-based assessment of slope stability. Bayraktaroğlu (2019) simulated the centrifuge test of a dyke section containing a liquefiable loose sand layer with a two-phase hypoplastic model, computing the pore-water pressure development during the earthquake and the subsequent dissipation phase, and emphasising the importance of updating the permeability. For problems of the static-liquefaction and flow-failure type, the hypoplastic representation of contractive behaviour in loose sand is particularly suitable (Fuentes et al., 2020).

Repeated and dynamic loading problems: In earthquake site response analysis, Reyes et al. (2009) showed that the IS-augmented hypoplastic model produces realistic hysteretic behaviour at large strains, beyond the equivalent-linear approach, in a one-dimensional site. In problems of the order of 10^5–10^7 cycles, such as machine, railway, and wind-turbine foundations, since cycle-by-cycle computation with the IS model is impractical, the HCA model (Niemunis et al., 2005), developed within the same framework as hypoplasticity, is used. For multidirectional (earthquake-like) shear paths, the Liao and Yang (2022) extension ensures the correct reproduction of the pore-water pressure accumulation rate.

Soil–structure interaction analyses: The cyclic shearing, local densification/loosening, and pore-water pressure accumulation at the foundation–soil interface can be represented with hypoplastic interface formulations and coupled analyses (Stutz, 2016; Bayraktaroğlu, 2019). The offshore foundation application of Bayraktaroğlu (2019), by establishing the structure–soil contact with frictional contact elements, provides an example of a full soil–structure interaction analysis. In problems of pile driving, vibration propagation, and interaction with neighbouring structures, hypoplasticity is also increasingly becoming a standard tool (Staubach et al., 2021).

COMPARISON OF HYPOPLASTICITY WITH OTHER CONSTITUTIVE MODELS

The choice of a soil constitutive model should not be based solely on the number of parameters or on ease of use. The strain level expected in the analysis, whether the loading is monotonic or cyclic, the stress path followed, and the test data available for calibration should be considered together. Because the Mohr–Coulomb, Hardening Soil, Modified Cam-Clay, and hypoplasticity models rest on different theoretical assumptions, the behavioural resolution they provide for the same geotechnical problem also varies considerably. The linear-elastic–perfectly-plastic Mohr–Coulomb model, owing to its limited number of parameters that are widely known in engineering practice, is useful particularly in analyses aimed at determining the collapse load or the factor of safety. However, because the elastic stiffness, strength, and dilation angle are assumed constant in the model, the stress-level- and initial-density-dependent behaviour of granular soils cannot be represented directly. Features such as the pre-failure reduction of stiffness, the irreversible strains that occur in loading–unloading cycles, post-peak softening, and the tendency towards a critical state also lie outside the scope of the standard formulation. For this reason, although the model may be adequate for bearing-capacity and general-stability problems, it may exhibit marked limitations in settlement, excavation-deformation, and cyclic-response analyses. The Hardening Soil model defines stress-level-dependent stiffness through a hyperbolic stress–strain relationship and accounts for the plastic strains arising from shear and from volumetric compression through different hardening mechanisms (Schanz et al., 1999). The separate definition of the small-strain shear modulus and of stiffness degradation in the HSsmall formulation provides an important advantage, especially in excavation, foundation, and retaining-structure analyses. However, the void ratio or relative density is not a fundamental state variable of the model. For this reason, representing different initial densities with the same parameter set is generally not possible, and recalibration may be required for each density state. Moreover, in the standard HS and HSsmall models the representation of post-peak softening and critical-state behaviour is limited. On the other hand, their elastoplastic structures based on yield surfaces allow stress-history and overconsolidation effects to be handled practically in engineering applications. The Modified Cam-Clay model and similar formulations based on critical-state mechanics were developed particularly to explain the relationship between the compression and shear behaviour of normally consolidated clays (Roscoe et al., 1958; Schofield and Wroth, 1968). Its definition of the critical-state concept within a systematic elastoplastic framework is the principal advantage of the model. Nevertheless, the direct application of the classical Cam-Clay approach to cohesionless soils is hampered by the pressure- and density-dependent behaviour of sands. The finite elastic region inside the yield surface, the development of peak strength in dilative sands, and the nonlinear isotropic compression behaviour of sands may not be explained with sufficient accuracy by the classical formulation. The SANISAND models developed for sands reduce a significant part of these limitations through a state parameter, moving surfaces, and advanced flow rules (Dafalias and Manzari, 2004; Taiebat and Dafalias, 2008). Comparisons under different stress paths reveal that the SANISAND family and hypoplastic models with the intergranular strain extension may exhibit different advantages under certain loading conditions (Wichtmann et al., 2019).

The von Wolffersdorff hypoplasticity model describes soil behaviour through a single incremental stress–strain relationship, without requiring a yield surface that explicitly separates elastic and plastic strains. In the model, the pressure effect is accounted for by barotropic factors and the density effect by pycnotropic factors. In this way, different initial void ratios and stress levels can be represented using essentially the same parameter set. The limiting-void-ratio relations proposed by Bauer (1996), together with the f_d state factor, establish a direct connection between peak strength, the dilation–contraction transition, strain softening, and the asymptotic tendency towards the critical state. While the eight parameters of the basic model can be determined from standard laboratory tests, five additional parameters are required for the intergranular strain extension (Herle and Gudehus, 1999; Niemunis and Herle, 1997). The addition of the intergranular strain variable to the model considerably improves the representation of the high initial stiffness in the small-strain region, of the stiffness change due to reversal of the loading direction, and of hysteretic cycles. Nevertheless, hypoplasticity and the intergranular strain extension do not by themselves solve all the problems of cyclic soil behaviour. In particular, at very large numbers of cycles the step-by-step computation of strain accumulation may entail a high computational cost; for such problems, high-cycle accumulation models may be more suitable (Niemunis et al., 2005). Nor should the standard formulation be expected to reliably reproduce, under every loading condition, full-liquefaction states approaching zero effective stress and butterfly-shaped cyclic stress paths (Wichtmann et al., 2019; Liao and Yang, 2022). Other important limitations of hypoplasticity are that natural anisotropy and fabric evolution are not directly defined in the basic model, that stress-history effects such as cementation and overconsolidation remain limited in the cohesionless-soil formulation, and that mesh dependence may arise in problems dominated by strain softening. Extended formulations that account for anisotropy and fabric development remedy part of these shortcomings (Yang et al., 2020; Liao and Yang, 2021, 2022). Furthermore, since the stress range used in calibrating the compression parameters such as h_s and n directly affects the model's predictions at high and low stress levels, the test data must be selected within a range appropriate to the analysis problem. In conclusion, hypoplasticity is distinguished from classical engineering models by combining pressure-dependent stiffness, the density effect, peak strength, dilation, softening, and critical-state behaviour within a single theoretical structure. In contrast, the Mohr–Coulomb model offers practical advantages in simple failure-oriented analyses, the HS/HSsmall models in excavation and settlement problems, and critical-state elastoplasticity particularly in modelling clay behaviour. Hypoplasticity should therefore be regarded not as an absolutely superior option for every problem, but as an approach that provides a higher capacity for representing behaviour in problems requiring detailed analysis of stress path, density, and cyclic response.

CONCLUSIONS AND RECOMMENDATIONS

In this chapter, the theoretical and applied principles concerning the representation of the stress–strain behaviour of cohesionless soils with hypoplastic constitutive models have been evaluated in an integrated manner. The nonlinear stiffness, permanent strain, density and stress-level effects, volumetric behaviour, peak strength, softening, and tendency towards a critical state observed in granular soils are seen not to be independent of one another. For these behaviours to be modelled reliably, the constitutive relationship used must encompass not only the failure state but the entire mechanical response extending from the onset of loading to large strains.

Unlike classical elastoplastic models, hypoplasticity operates without separating elastic and plastic strains into distinct components. The difference between loading and unloading arises from the incrementally nonlinear structure of the constitutive equation, rather than from a predefined yield criterion. This feature enables the irreversible soil behaviour that occurs even under small stress changes to be represented within a single mathematical relationship. The lack of a need for a yield surface, a plastic potential, and a separate hardening rule simplifies the theoretical structure; in return, it requires a correct understanding of the tensorial structure of the model and of the physical meanings of the state variables.

One of the most important advantages of the basic hypoplastic model developed for cohesionless soils is that it treats density and pressure effects within a common definition of state. The position of the current void ratio relative to the pressure-dependent limiting void ratios determines the stiffness, strength, and volumetric tendency of the soil. In this way, the peak strength, dilation, and softening that arise in a dense sand and the contraction and continuous hardening observed in a loose sand can be produced without the need for separate material models. The approach to the critical state at large strains, independently of the initial conditions, is likewise achieved within the same mathematical structure. This allows the model to examine different density and stress levels with a single consistent parameter set.

The engineering reliability of the model is directly related to the process of determining and validating the parameters. The basic parameters can be determined using data obtained from index, compression, and drained shear tests. However, the direct use in field analyses of the first parameter set computed from test results should not be considered sufficient. The parameters should first be checked at the element-test level, with the measured and computed curves evaluated together, and then tested with independent tests not used in the calibration. In particular, the selection of the parameters controlling the pressure- and density-dependent variation of stiffness in accordance with the stress range expected in the analysis is decisive for the accuracy of the results.

Although the basic hypoplastic model can represent granular soil behaviour in detail under monotonic loading conditions, it is not by itself sufficient for small-strain and repeated-loading problems. The addition of the intergranular strain variable to the model enables the remembering of the change in loading direction, the high initial stiffness after a reversal of direction, and a more realistic computation of cyclic hysteresis. This extension considerably reduces the excessive cyclic strain accumulation that can occur in the basic model. Nevertheless, in problems where the number of cycles is very large, where the loading direction changes continuously, or where the effective stress approaches zero, the predictive capacity of the standard extended model may remain limited. In such cases, advanced models focused on cyclic accumulation, fabric change, or liquefaction, appropriate to the nature of the problem, should be considered.

Hypoplastic models offer a framework that can be used in a wide variety of geotechnical problems, such as foundation and excavation deformations, tunnels, embankments and slopes, offshore structures, piles, repeatedly loaded infrastructure systems, and soil–structure interaction. The detailed behavioural representation provided by the model constitutes a marked advantage, especially in problems where the density and stress state of the soil changes considerably during the analysis. However, the use of an advanced constitutive model is not by itself sufficient for a reliable numerical analysis; the definition of the initial stress and void-ratio field, of the drainage and interface conditions, in accordance with the field situation, the stable execution of the numerical solution, and the keeping of the state variables within their physical validity limits are at least as decisive for the reliability of the results as the constitutive model itself.

Model selection should not be treated as the automatic preference for the most advanced formulation. In problems where only the collapse load or the general level of safety is investigated, models with fewer parameters may be sufficient; in routine settlement and excavation analyses, engineering models that account for stress-level-dependent stiffness may provide practical solutions. In contrast, in problems where density change, reversal of loading direction, small-strain stiffness, cyclic accumulation, or critical-state behaviour is decisive, hypoplasticity offers a more comprehensive description of behaviour. On the other hand, some limitations of the model should be borne in mind: natural anisotropy and fabric evolution are not directly included in the basic formulation; stress-history effects such as cementation and overconsolidation are represented in a limited way in the cohesionless-soil form; the solution may become sensitive to mesh size in problems dominated by strain softening; and the stress range in which the compression parameters are determined directly affects the model's predictions at different stress levels. For this reason, the appropriate model should be selected by considering together the aim of the analysis, the expected strain range, the type of loading, and the nature of the available test data.

It would be useful for future studies to focus on establishing validated parameter databases for local soils of different origin and granulometry. Extending experimental programmes to cover effects such as small-strain stiffness, cyclic mobility, anisotropy, grain crushing, and partial saturation will broaden the field of application of the models. In addition, the systematic investigation of parameter sensitivity, the making transparent of calibration procedures, and the comparison of different constitutive models on the same test data set are steps that will support model selection and reliability. In conclusion, hypoplasticity offers a powerful theoretical basis for explaining the state- and loading-path-dependent behaviour of cohesionless soils; with appropriate experimental calibration and careful numerical implementation, it becomes an effective tool in deformation-oriented geotechnical analyses.

REFERENCES

Atkinson, J. H., Richardson, D., and Stallebrass, S. E. (1990). Effect of recent stress history on the stiffness of overconsolidated soil. *Géotechnique*, *40*(4), 531–540. https://doi.org/10.1680/geot.1990.40.4.531

Bauer, E. (1996). Calibration of a comprehensive hypoplastic model for granular materials. *Soils and Foundations*, *36*(1), 13–26. https://doi.org/10.3208/sandf.36.13

Bayraktaroğlu, H. (2019). *Assessment of porosity-permeability variation on the response of sandy soils via hypoplasticity model* [Master's thesis, Middle East Technical University]. Ankara.

Casagrande, A. (1936). Characteristics of cohesionless soils affecting the stability of slopes and earth fills. *Journal of the Boston Society of Civil Engineers*, *23*(1), 1–32.

Cui, Y., Su, H., Jia, N., and Wang, T. (2024). Development of a modified hypoplastic model for calcareous sand considering particle crushing. *Engineering Geology*, *331*, 107432. https://doi.org/10.1016/j.enggeo.2024.107432

Dafalias, Y. F., and Manzari, M. T. (2004). Simple plasticity sand model accounting for fabric change effects. *Journal of Engineering Mechanics*, *130*(6), 622–634.

Duque, J., Mašín, D., and Fuentes, W. (2020). Improvement to the intergranular strain model for larger numbers of repetitive cycles. *Acta Geotechnica*, *15*(12), 3593–3604. https://doi.org/10.1007/s11440-020-01073-w

Ertek, M. K. (2020). *Kum zeminlerin davranışı için hipoplastisiteye dayalı bünye modellemesi* [Doctoral dissertation, Ondokuz Mayıs University]. Samsun.

Fuentes, W., and Triantafyllidis, T. (2015). ISA model: A constitutive model for soils with yield surface in the intergranular strain space. *International Journal for Numerical and Analytical Methods in Geomechanics*, *39*(11), 1235–1254. https://doi.org/10.1002/nag.2370

Fuentes, W., Wichtmann, T., Gil, M., and Lascarro, C. (2020). ISA-Hypoplasticity accounting for cyclic mobility effects for liquefaction analysis. *Acta Geotechnica*, *15*, 1513–1531. https://doi.org/10.1007/s11440-019-00846-2

Goldscheider, M. (1976). Grenzbedingung und Fließregel von Sand. *Mechanics Research Communications*, *3*(6), 463–468.

Gudehus, G. (1979). A comparison of some constitutive laws for soils under radially symmetric loading and unloading. In *Proceedings of the 3rd International Conference on Numerical Methods in Geomechanics*. Aachen: Balkema.

Gudehus, G. (1996). A comprehensive constitutive equation for granular materials. *Soils and Foundations*, *36*(1), 1–12. https://doi.org/10.3208/sandf.36.1

Gudehus, G., Amorosi, A., Gens, A., Herle, I., Kolymbas, D., Mašín, D., Muir Wood, D., Nova, R., Niemunis, A., Pastor, M., Tamagnini, C., and Viggiani, G. (2008). The soilmodels.info project. *International Journal for Numerical and Analytical Methods in Geomechanics*, *32*(12), 1571–1572. https://doi.org/10.1002/nag.675

Herle, I. (1997). *Hypoplastizität und Granulometrie einfacher Korngerüste* [Doctoral dissertation]. Veröffentlichungen des Institutes für Bodenmechanik und Felsmechanik der Universität Fridericiana in Karlsruhe, Heft 142.

Herle, I., and Gudehus, G. (1999). Determination of parameters of a hypoplastic constitutive model from properties of grain assemblies. *Mechanics of Cohesive-Frictional Materials*, *4*(5), 461–486.

Herle, I., and Mayer, P.-M. (2009). Calculation of deformations of an underwater excavation using parameters of Berlin sand from a hypoplastic model. *Bautechnik*, *86*(S1), 75–85. https://doi.org/10.1002/bate.200910044

Hleibieh, J., Wegener, D., and Herle, I. (2014). Numerical simulation of a tunnel surrounded by sand under earthquake using a hypoplastic model. Acta Geotechnica, 9(4), 631–640. https://doi.org/10.1007/s11440-013-0294-8

Holler, S. (2006). "Dynamisches Mehrphasenmodell mit hypoplastischer Materialformulierung der Feststoffphase." Cologne: Rheinisch-Westfälischen Technischen Hochschule Aachen.

Kadlíček, T., Janda, T., Šejnoha, M., Mašín, D., Najser, J., and Beneš, Š. (2022). Automated calibration of advanced soil constitutive models. Part I:

Hypoplastic sand. *Acta Geotechnica*, *17*(8), 3421–3438. https://doi.org/10.1007/s11440-021-01441-0

Kolymbas, D. (1977). A rate-dependent constitutive equation for soils. *Mechanics Research Communications*, *4*(6), 367–372.

Kolymbas, D. (1985). A generalized hypoplastic constitutive law. In *Proceedings of the 11th International Conference on Soil Mechanics and Foundation Engineering* (Vol. 5, p. 2626). San Francisco: Balkema.

Kolymbas, D. (1991). An outline of hypoplasticity. *Archive of Applied Mechanics*, *61*(3), 143–151.

Kolymbas, D. (2000). *Introduction to hypoplasticity*. Rotterdam: Balkema.

Kolymbas, D. (2012). Barodesy: A new hypoplastic approach. *International Journal for Numerical and Analytical Methods in Geomechanics*, *36*(9), 1220–1240.

Kolymbas, D. 2016. GEOTECHNIK: bodenmechanik, grundbau und tunnelbau. MORGAN KAUFMANN, Springer-Verlag Berlin Heidelberg.

Kolymbas, D., and Wu, W. (1990). Recent results of triaxial tests with granular materials. *Powder Technology*, *60*(2), 99–119.

Li, X. S., and Wang, Y. (1998). Linear representation of steady-state line for sand. *Journal of Geotechnical and Geoenvironmental Engineering*, *124*(12), 1215–1217.

Liao, D., and Yang, Z. X. (2021). Hypoplastic modeling of anisotropic sand behavior accounting for fabric evolution under monotonic and cyclic loading. *Acta Geotechnica*, *16*(7), 2003–2029.

Liao, D., and Yang, Z. X. (2022). Hypoplastic model for sand under multidirectional shearing conditions considering fabric change effect. *Soil Dynamics and Earthquake Engineering*, *155*, 107168. https://doi.org/10.1016/j.soildyn.2022.107168

Mašín, D. (2005). A hypoplastic constitutive model for clays. *International Journal for Numerical and Analytical Methods in Geomechanics*, *29*(4), 311–336.

Mašín, D. (2019). *Modelling of soil behaviour with hypoplasticity: Another way to the mechanics of granular materials*. Cham: Springer. https://doi.org/10.1007/978-3-030-03976-9

Matsuoka, H., and Nakai, T. (1974). Stress-deformation and strength characteristics of soil under three different principal stresses. *Proceedings of the Japan Society of Civil Engineers*, *232*, 59–70. https://doi.org/10.2208/jscej1969.1974.232_59

Miura, K., Maeda, K., and Toki, S. (1997). Method of measurement for the angle of repose of sands. *Soils and Foundations*, *37*(2), 89–96. https://doi.org/10.3208/sandf.37.2_89

Niemunis, A. (2003). *Extended hypoplastic models for soils* [Habilitation thesis]. Schriftenreihe des Institutes für Grundbau und Bodenmechanik der Ruhr-Universität Bochum, Heft 34.

Niemunis, A., and Herle, I. (1997). Hypoplastic model for cohesionless soils with elastic strain range. *Mechanics of Cohesive-Frictional Materials*, *2*(4), 279–299.

Niemunis, A., Wichtmann, T., and Triantafyllidis, T. (2005). A high-cycle accumulation model for sand. *Computers and Geotechnics*, *32*(4), 245–263.

Reyes, D. K., Rodriguez-Marek, A., and Lizcano, A. (2009). A hypoplastic model for site response analysis. *Soil Dynamics and Earthquake Engineering*, *29*(1), 173–184. https://doi.org/10.1016/j.soildyn.2008.01.003

Roscoe, K. H., Schofield, A. N., and Wroth, C. P. (1958). On the yielding of soils. *Géotechnique*, *8*(1), 22–53.

Schanz, T., and Vermeer, P. A. (1996). Angles of friction and dilatancy of sand. *Géotechnique*, *46*(1), 145–151.

Schanz, T., Vermeer, P. A., and Bonnier, P. G. (1999). The hardening soil model: Formulation and verification. In R. B. J. Brinkgreve (Ed.), *Beyond 2000 in computational geotechnics* (pp. 281–296). Rotterdam: Balkema.

Schofield, A. N., and Wroth, C. P. (1968). *Critical state soil mechanics*. London: McGraw-Hill.

Staubach, P., Machaček, J., Skowronek, J., and Wichtmann, T. (2021). Vibratory pile driving in water-saturated sand: Back-analysis of model tests using a hydro-mechanically coupled CEL method. *Soils and Foundations*, *61*(1), 144–159. https://doi.org/10.1016/j.sandf.2020.11.005

Sturm, H. (2011). Geotechnical performance of a novel gravity base type shallow foundation for offshore wind turbines. *geotechnik*, *34*(2), 85–96. https://doi.org/10.1002/gete.201100013

Stutz, H. H. (2016). *Hypoplastic models for soil-structure interfaces: Modelling and implementation* [Doctoral dissertation, Kiel University]. Kiel.

Taiebat, M., and Dafalias, Y. F. (2008). SANISAND: Simple anisotropic sand plasticity model. *International Journal for Numerical and Analytical Methods in Geomechanics*, *32*(8), 915–948.

Verdugo, R., and Ishihara, K. (1996). The steady state of sandy soils. *Soils and Foundations*, *36*(2), 81–91.

von Wolffersdorff, P.-A. (1996). A hypoplastic relation for granular materials with a predefined limit state surface. *Mechanics of Cohesive-Frictional Materials*, *1*(3), 251–271.

von Wolffersdorff, P.-A., and Schwab, R. (2009). The Uelzen I lock: Hypoplastic finite-element analysis of cyclic loading. *Bautechnik*, *86*(S1), 64–73. https://doi.org/10.1002/bate.200910043

Wegener, D., and Herle, I. (2014). Prediction of permanent soil deformations due to cyclic shearing with a hypoplastic constitutive model. *geotechnik*, *37*(2), 113–122.

Wichtmann, T., and Triantafyllidis, T. (2016). An experimental database for the development, calibration and verification of constitutive models for sand with focus to cyclic loading: Part I—Tests with monotonic loading and stress cycles. *Acta Geotechnica*, *11*(4), 739–761.

Wichtmann, T., Fuentes, W., and Triantafyllidis, T. (2019). Inspection of three sophisticated constitutive models based on monotonic and cyclic tests on fine sand: Hypoplasticity vs. Sanisand vs. ISA. *Soil Dynamics and Earthquake Engineering*, *124*, 172–183.

Wu, W. (1992). *Hypoplastizität als mathematisches Modell zum mechanischen Verhalten granularer Stoffe* [Doctoral dissertation]. Veröffentlichungen des Institutes für Bodenmechanik und Felsmechanik der Universität Fridericiana in Karlsruhe, Heft 129.

Wu, W., and Bauer, E. (1994). A simple hypoplastic constitutive model for sand. *International Journal for Numerical and Analytical Methods in Geomechanics*, *18*(12), 833–862. https://doi.org/10.1002/nag.1610181203

Wu, W., Bauer, E., and Kolymbas, D. (1996). Hypoplastic constitutive model with critical state for granular materials. *Mechanics of Materials*, *23*(1), 45–69. https://doi.org/10.1016/0167-6636(96)00006-3

Wu, W., and Kolymbas, D. (1990). Numerical testing of the stability criterion for hypoplastic constitutive equations. *Mechanics of Materials*, *9*(3), 245–253.

Wu, W., Lin, J., and Wang, X. (2017). A basic hypoplastic constitutive model for sand. *Acta Geotechnica*, *12*(6), 1373–1382. https://doi.org/10.1007/s11440-017-0550-4

Wu, W., and Niemunis, A. (1996). Failure criterion, flow rule and dissipation function derived from hypoplasticity. *Mechanics of Cohesive-Frictional Materials*, *1*(2), 145–163.

Yang, Z. X., Liao, D., and Xu, T. T. (2020). A hypoplastic model for granular soils incorporating anisotropic critical state theory. *International Journal for Numerical and Analytical Methods in Geomechanics*, *44*(6), 723–748.

Youd, T. L. (1972). Compaction of sands by repeated shear straining. *Journal of the Soil Mechanics and Foundations Division*, *98*(SM7), 709–725.

Shaking Table Testing in Geotechnical Earthquake Engineering: Similitude, Experimental Design, Applications, and Soil–Structure Interaction

Bayram ATEŞ[1*]

Mohammad Azim EIRGASH[2]

1- PhD, Civil Engineering Department, Karadeniz Technical University, 61080 Trabzon, Türkiye, Email: bayramates61@hotmail.com, ORCID: 0000-0002-1251-7053 (corresponding author)[*]
2- PhD, Civil Engineering Department, Karadeniz Technical University, 61080 Trabzon, Türkiye, Email: azim.eirgash@ktu.edu.tr, ORCID: https://orcid.org/0000-0001-5399-115X

ABSTRACT

The behavior of soils and soil-structure systems under seismic action is a complex and coupled phenomenon whose reliable prediction by theoretical and numerical means alone is difficult, owing to the nonlinear cyclic response of soil, the build-up of excess pore water pressure, liquefaction, and interactions arising from kinematic and inertial effects. Shaking table testing is one of the principal physical modeling methods that allows this behavior to be studied in the gravitational (1g) field under controlled and repeatable conditions and to be tracked through to failure. In this chapter, the theoretical foundations of the method and the experimental setup are examined in detail; the similitude rules and scaling, the components and technical characteristics of the shaking table system, the model soil containers (boxes) together with boundary effects, and the instrumentation are presented critically. Subsequently, seven fundamental application areas of geotechnical earthquake engineering, slope stability and landslides, retaining structures and reinforced-soil walls, soil liquefaction, piled and deep foundations, tunnels and buried structures, embankments-dams-shallow foundations, and soil-structure interaction and geotechnical seismic isolation are critically reviewed through the leading shaking table studies in the literature. The study emphasizes the capability of shaking table tests to investigate soil–structure interaction mechanisms, in revealing failure mechanisms, and in validating numerical models; it discusses the limitations arising from stress-level-dependent scale effects and from finite model boundaries, and it summarizes future research directions encompassing the integrated use of 1g and centrifuge testing, multi-component (three-directional) input motion, and advanced measurement techniques such as digital image correlation.

Keywords – Shaking table, physical modeling, geotechnical earthquake engineering, similitude rules, liquefaction, soil-structure interaction.

INTRODUCTION

Earthquakes are among the principal causes of the damage observed in the ground and in engineering structures that are either buried in or founded on soil. Under strong ground motion, soils exhibit a markedly nonlinear and elasto-plastic behavior in which the stress-strain relationship varies with amplitude and number of cycles; with increasing cyclic strain, the shear modulus decreases, the damping ratio rises, and in saturated loose granular soils excess pore water pressure accumulates, reducing the effective stress and thereby the strength and stiffness. In the limiting case, this process can lead to liquefaction, lateral spreading, and large permanent deformations. The coupled (solid-fluid interacting) behavior of the soil skeleton and pore water, the dependence of the material response on confining pressure and stress history, and the complexity of the interface and boundary conditions render the reliable prediction of these phenomena by closed-form solutions or numerical methods alone difficult. For this reason, physical modeling methods are employed in order to observe directly, under controlled and repeatable conditions, the behavior of geotechnical systems subjected to seismic action. One of the situations in which this difficulty emerges most conspicuously is soil-structure interaction. The motion transmitted to a structure during an earthquake is determined not by the free-field ground motion alone, but jointly by the stiffness of the soil surrounding the foundation, the kinematic constraint imposed on the foundation by the surrounding soil, and the feedback of the superstructure's inertial forces into the foundation-soil system. This coupled nature of kinematic and inertial interaction makes it essential to treat the superstructure-foundation-soil system as a whole, particularly in soft and liquefiable soils and in deep foundations. Because shaking table tests permit this system to be modeled together under realistic boundary conditions and with dense instrumentation, they occupy a central position in the experimental investigation of soil-structure interaction.

Two principal physical modeling approaches stand out in geotechnical earthquake engineering: shaking table tests conducted in the gravitational (1g) field and dynamic centrifuge tests conducted in an elevated gravity field. By testing the model in a gravity field of several tens of g and thereby reproducing within a small model the same effective stress level as in the prototype, centrifuge tests offer an advantage in the accurate scaling of stress-level-dependent soil behavior. Shaking table tests, by contrast, allow for much larger model dimensions, the accommodation of complex and multi-component structural models, rich instrumentation, and the direct observation of failure mechanisms. The two methods are complementary and, in contemporary practice, are most often used together in order to cross-validate one another's results and those of numerical models. The theoretical framework of the method and the principles of similitude have been treated in detail in the foundational monographs and methodological reviews of earthquake geotechnical engineering (Iai, 1989; Muir Wood et al., 2002; Towhata, 2008).

The application of shaking table tests to geotechnical problems has a long history; interest in the phenomenon of liquefaction, particularly following the 1964 Niigata earthquake, accelerated the investigation of the dynamic behavior of saturated sands through model tests. In subsequent years, experimental capabilities expanded considerably with developments such as servo-hydraulic actuation systems, multi-axis tables, and laminar shear boxes; today, facilities such as the three-directional E-Defense table, measuring 20 m × 15 m, make it possible to test soil-structure systems at near-full scale. Advances in measurement techniques have likewise increased the resolution of the method; tools such as miniature pore water pressure transducers, non-contact laser displacement sensors, and digital image correlation have made it possible to monitor in detail the full-field response of the soil during a test. The contemporary role of shaking table tests is not confined to the observation of phenomena alone. Because stress-level-dependent scale effects cannot be fully satisfied in reduced-scale 1g models, these tests are increasingly designed to generate controlled, high-quality reference data for the calibration and validation of three-dimensional, nonlinear numerical models. This integrated experiment-simulation approach contributes to the advancement of the performance-based earthquake engineering paradigm and of design codes for both geotechnical and structural systems.

The aim of this chapter is to review critically, in light of the current literature, the use of shaking table tests in geotechnical engineering. The chapter comprises two main parts: the first part critically addresses the theoretical foundations of the method and the experimental setup, the similitude rules and scaling, the components and equipment of the shaking table system, the model soil containers together with boundary effects, and the instrumentation; the second part evaluates the contributions of the method across its seven fundamental application areas through selected representative studies from each area.

THEORETICAL FOUNDATIONS OF SHAKING TABLE TESTS AND THE EXPERIMENTAL SETUP

Similitude Rules and Scaling

The extension to prototype behavior of the results obtained from a reduced-scale model test depends on establishing geometric, kinematic, and dynamic similarity between model and prototype through appropriate scaling factors. Within the framework of dimensional analysis (the Buckingham-Π theorem), complete similarity of a physical model is achieved only when all dimensionless numbers (for example, the stress-to-stiffness ratio and the inertial-to-gravitational force ratio) are held equal between model and prototype. The similitude rules that constitute the theoretical basis of shaking table tests were derived for saturated soil-structure-fluid systems in the 1g gravitational field in a work that is among the most fundamental references in the field (Iai, 1989). In that work, scaling factors were obtained from the equilibrium and continuity equations of the soil skeleton, pore water, pile and sheet-pile structures, and external water, and the assumption that the stress-strain relationship can be determined independently of confining pressure was shown to be valid at the moderate, pre-failure strain levels. The derived set of similitude relations is therefore applicable to deformation-oriented model tests rather than to ultimate stability conditions.

The Iai (1989) similitude rests on three mutually independent fundamental scaling factors: the geometric scaling factor (λ = prototype dimension/model dimension), the density scaling factor (usually taken as 1 when the same soil is used), and the strain scaling factor (λ_ε). The scaling factors of all other quantities are derived from these three. Since the gravitational acceleration is the same in the model and the prototype in the 1g field, the acceleration scaling factor is 1; stress, being proportional to the overburden pressure, scales with λ, and pore water pressure likewise scales with λ. In the simplest case, in which strain is not scaled ($\lambda_\varepsilon = 1$), dynamic time scales with $\lambda^{0.5}$, frequency with $\lambda^{-0.5}$, and displacement with λ. For stress-level-dependent granular soils, however, it is commonly assumed that strain scales as $\lambda_\varepsilon = \lambda^{0.5}$, on the grounds that the shear modulus of sand is proportional to the square root of the confining pressure; this case corresponds to the Type II similitude of Iai (Iai, 1989; Iai et al., 2005). Under the Type II rules, stiffness (shear modulus) scales with $\lambda^{0.5}$ (stress/strain), displacement with $\lambda^{1.5}$ (length × strain), dynamic time with $\lambda^{0.75}$, and frequency with $\lambda^{-0.75}$. For consistency of the seepage-related response, the same framework requires the coefficient of permeability to be scaled by $\lambda^{0.75}$, which in practice is achieved by using a pore fluid more viscous than water; if instead the same soil and pore water are used, diffusion-driven processes such as consolidation follow a slower time scale (of the order of $\lambda^{1.5}$ for $\lambda_\varepsilon = \lambda^{0.5}$, and λ^2 for $\lambda_\varepsilon = 1$), which cannot be satisfied simultaneously with the dynamic time scale.

Generalized scaling relations that unify the similitude rules of 1g and centrifuge tests within a common framework have also been proposed (Iai et al., 2005). In this approach, a large scaling factor (λ) is decomposed into the product ($\lambda = \mu\eta$) of an intermediate scale (μ), defined by the similitude rule in the 1g field, and the conventional centrifuge scale (η); the effective scaling limit of available centrifuge facilities can thereby be extended. A methodological appraisal of the design of shaking table model tests, container selection, and scaling difficulties has, in turn, been discussed comprehensively in the physical modeling literature (Muir Wood et al., 2002). The most fundamental difficulty of scaling is that different physical processes possess conflicting time scales. Whereas the dynamic time scale is $\lambda^{0.75}$ under the Type II similitude and $\lambda^{0.5}$ when strain is not scaled, the corresponding diffusion time scales are approximately $\lambda^{1.5}$ and λ^2, respectively, when the same soil and pore fluid are used. The impossibility of satisfying these two-time scales simultaneously in a single test is a critical limitation, particularly in liquefaction problems in which drainage during shaking is important. In practice, this conflict is addressed either by using a more viscous fluid in place of pore water (scaling of permeability) or by assuming that undrained conditions prevail during rapid seismic loading. In addition, because the same soil is used in 1g models, grain size cannot be scaled, which may give rise to grain-size effects in very small models; to limit this effect, it is recommended that the ratio of the characteristic model dimension to the mean grain diameter be kept sufficiently large.

The most important of these difficulties is that stress-level-dependent soil strength and stiffness differ in reduced-scale 1g models relative to the prototype; because granular soils can exhibit higher dilatancy and a larger angle of internal friction under low overburden pressure, the model behavior may deviate from that of the prototype. A common way of controlling this deviation is the "modeling of models" technique, in which the same prototype is tested at several model scales; agreement among the results at different scales indicates that the scale effects are at an acceptable level. Adjusting the model relative density so as to reproduce the normalized stress-strain response of the prototype at a given stress level (for example, by selecting a lower model relative density) is also a frequently adopted strategy. For all these reasons, in contemporary practice shaking table tests are most often designed to generate high-quality data for the validation of numerical models, and the experiment and simulation are carried out in an integrated manner.

Components and Technical Characteristics of the Shaking Table System

A shaking table system consists essentially of a rigid platform (the table) on which the model container is fixed, the servo-hydraulic actuators that drive this platform, the hydraulic power unit and pressure accumulators that supply the actuators with high-flow-rate oil, and a large-mass reaction foundation (reaction mass) that resists the reaction forces of the motion. Generally fabricated from steel or an aluminum alloy, the platform is designed to be strong enough to be regarded as rigid within its own plane, yet as light as possible in order to limit inertial forces. The reaction mass ensures the transmission of the dynamic forces generated by the table to the laboratory floor and the damping of unwanted vibrations; in large facilities, this mass can reach several tens of times the load carried by the table. A representative laboratory shaking table–laminar box assembly is shown in Figure 1.

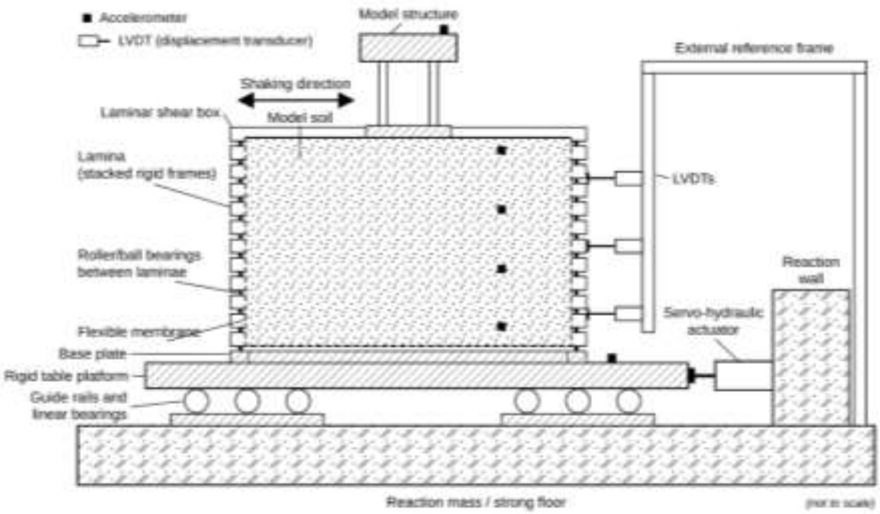

Figure 1: Schematic view of the shaking table system

Shaking tables are classified according to the number of degrees of freedom they provide. While many tables in university laboratories operate uniaxially (in a single horizontal direction), more advanced systems may be biaxial (two horizontal, or one horizontal and one vertical), triaxial, or six-degree-of-freedom (6-DOF), capable of generating three translational and three rotational components together. The performance of a shaking table is defined by the table dimensions, the maximum model weight it can carry (payload capacity), the maximum acceleration, velocity, and displacement (stroke) it can generate, and the frequency band over which it can operate (typically 0–50 Hz, and higher in some systems). These parameters are not independent of one another: for a given actuator, the motion is governed at low frequencies by the displacement (stroke) limit, at intermediate frequencies by the velocity limit, and at high frequencies by the acceleration (force) limit; as the carried model weight increases, the maximum attainable acceleration decreases. The weight of the model soil container and of the soil it holds is likewise a significant item that must be deducted from this payload capacity. The actuators are supplied from the hydraulic power unit through high-flow servo valves; pressure accumulators are added to the system to meet the high instantaneous flow rate required during sudden acceleration demands. Shaking tables operate under closed-loop servo control in order to reproduce a target ground motion accurately, and three-variable control, combining displacement feedback at low frequencies with velocity and acceleration feedback at intermediate and high frequencies, is widely preferred. However, because the mass and nonlinear behavior of the model container and the soil alter the dynamic response of the table-specimen system (control-structure interaction), the measured table motion may deviate from the target record; moreover, the actuator-oil resonance arising from the compressibility of the oil column can distort the response at a particular frequency. To remove these effects, the input signal is refined successively by means of iterative/offline waveform compensation techniques based on the measured transfer function of the system.

The difference in facility scale directly determines the achievable model size and hence the severity of the scale effects. With its 20 m × 15 m table, its model payload capacity reaching 12 MN (approximately 1200 ton), and its three-directional motion capability, the E-Defense facility permits the testing of near-full-scale and even full-scale structural and soil models; some of the pile-group–lateral-spreading tests reviewed in this chapter were also carried out at this facility (Motamed et al., 2013). The smaller tables in university laboratories (typically in the 1–6 m range), by contrast, require working with larger scaling factors; this increases the importance of the scaling difficulties discussed in the preceding subsection and renders the design of the laminar container even more critical.

Model Soil Containers and Boundary Effects

The reproduction, within a finite-sized model container, of the free-field behavior of a real soil medium of semi-infinite extent is one of the most critical design problems in shaking table testing. Rigid-walled boxes can give rise to wave reflections and unrealistic stress concentrations at the end faces along the shaking direction. Laminar (layered) shear boxes, developed to minimize these boundary effects, consist of numerous rigid frames that can slide freely relative to one another and can emulate the depth-varying shear (one-dimensional, 1-D) deformation mode of the soil. The design principles and boundary effects of the different container types (rigid, laminar, flexible shear stack) have been reviewed critically for both 1g and N-g conditions (Bhattacharya et al., 2012). From a technical standpoint, three fundamental container types are distinguished. Rigid-walled boxes are the easiest to fabricate; however, the horizontal stiffness of the walls, which differs from that of the soil, causes unrealistic stress concentrations and wave reflections at the end faces. Laminar shear boxes consist of independent frame layers that can slide relative to one another with almost no resistance on linear bearings or roller mechanisms; each layer can thus follow the free-field horizontal displacement at the corresponding depth, and the horizontal stiffness of the box is reduced to a negligible level. The flexible shear stack, in turn, is designed from alternately arranged rubber and aluminum rings so that the shear stiffness of the stack approximates that of the model soil. For rigid containers, L/H ratios greater than approximately four have been recommended to limit end-boundary effects; however, the adequacy of the container dimensions should be verified for the selected container type, soil stiffness, and frequency range (Bhattacharya et al., 2012; Turan et al., 2009; Bagheri and Eseller-Bayat, 2024).

The influence of container design and boundary conditions on test results has been studied intensively in the recent literature. In a study that directly compared a rigid box with a laminar shear box, the acceleration responses at the center of the box and near the wall in the laminar box were found to be very close to one another, and the laminar box was shown to emulate the infinite half-space (free-field) behavior more successfully than the rigid box (Kim et al., 2020). When the use of a rigid container is unavoidable, the choice of the absorbing materials placed at the artificial boundaries perpendicular to the shaking direction becomes important; in a test series that compared four different boundary conditions, a polyethylene foam layer was found to provide the best emulation, although this effect diminished with increasing earthquake intensity (Lei et al., 2020).

In a uniaxial laminar shear box designed for small shaking tables, tests conducted with a synthetic clay model soil demonstrated that the box could preserve one-dimensional (1-D) soil-column behavior without producing significant boundary effects and that the dynamic behavior of the model soil was consistent with cyclic laboratory tests (Turan et al., 2009). In subsequent years, the design of biaxial laminar shear boxes came to the fore; one example, a large-scale box with 16 layers, was developed for liquefaction research (Castelli et al., 2022). In a large biaxial laminar shear box intended for the study of saturated sand deposits under bidirectional seismic loading, stacked octagonal frames were designed to offer minimal resistance to shear motion, and empty-box and soil-column tests confirmed that the boundary effect was negligible (Fan et al., 2024). Further experimental studies on the fabrication and performance verification of laminar shear boxes also exist (Shi et al., 2021; Mittal and Samanta, 2025). In a comprehensive review and numerical verification study of laminar container performance, it was determined that the roller motion mechanism did not amplify the applied motion, whereas the flexible sealing element could undergo excessive deformation (Bagheri and Eseller-Bayat, 2024). The quantitative determination of free-field soil behavior is likewise a distinct research topic. In 1g tests conducted on a three-meter-high sand column, the settlement, dynamic properties, and shear modulus degradation relationships of the sand column were determined; the estimated parameters were shown to be effective in approximately reproducing the free-field response in numerical models (Xu et al., 2022).

Instrumentation and Test Configuration

In a typical shaking table test, the acceleration amplification at different elevations is measured with accelerometers placed within the model soil and structure; the development and dissipation of excess pore water pressure in saturated soils is measured with pore water pressure transducers; and the deformation field is measured with displacement transducers (LVDTs) and, increasingly in recent years, with image-based (digital image correlation) techniques. In structural models, the internal forces in the reinforcement and structural members are monitored with strain gauges, as illustrated by the representative accelerometer and strain-gauge layout presented by Zhu et al. (2021). Sinusoidal (harmonic) waves, sweep waves, Ricker wavelets, and real earthquake acceleration records (for example, the El Centro, Kobe, and Wenchuan records) are used as input motion; low-amplitude white-noise excitations applied before and after the test track the change in the model's natural frequency and damping ratio, and hence the progression of damage. This test configuration constitutes a common methodological framework across all of the application areas addressed in the following sections.

The technical selection of the measurement hardware directly affects the reliability of the test. For acceleration measurement, piezoelectric accelerometers are preferred in cases requiring a wide frequency band, whereas MEMS-type accelerometers are preferred for low-frequency motions with a direct-current (DC) component. The miniature pore water pressure transducers used in saturated soils must be equipped with high-air-entry porous stones so that they can follow rapid cyclic pressure changes without lag, and the measurement line must be saturated by careful de-airing. For the measurement of deformations, contact LVDTs as well as non-contact laser displacement sensors are used; for determining the shear-wave velocity at small strains, bender elements are used; and for full-field displacement maps, particle image velocimetry (PIV) and digital image correlation (DIC) are increasingly common. The low-amplitude white-noise excitations applied before and after the test allow the model's transfer function—and hence its natural frequency and damping ratio—to be identified (system identification); methods have also been developed for estimating the dynamic properties and shear modulus degradation relationships of the free-field sand column (Xu et al., 2022).

Comparison of 1g Shaking Table and Centrifuge Tests

The two fundamental avenues of physical modeling in geotechnical earthquake engineering, 1g shaking table and dynamic centrifuge tests, possess complementary strengths and weaknesses. By testing the model in an elevated gravity field, centrifuge tests can reproduce within a small model the same stress level as in the prototype; this is an important advantage for the accurate scaling of stress-level-dependent soil behavior. 1g shaking table tests, by contrast, allow for much larger model dimensions, the accommodation of complex structural geometries, rich instrumentation, and the direct observation of failure mechanisms. The generalized scaling approach that unites the similitude rules of the two methods under a common framework makes it possible, through the concept of two-stage scaling, to exploit the advantages of both methods (Iai et al., 2005). Indeed, the behavior of large pile groups in liquefiable soil has been studied by both 1g tests and centrifuge shaking table tests (Liu et al., 2018), while an international database on rocking shallow foundations has jointly evaluated five centrifuge and three 1g test series (Gavras et al., 2020). In contemporary practice, these two methods are increasingly used in an integrated manner in order to cross-validate one another's results and those of numerical models.

APPLICATIONS OF SHAKING TABLE TESTS IN GEOTECHNICAL EARTHQUAKE ENGINEERING

Slope Stability and Landslides

Earthquake-induced slope instabilities and landslides are among the areas in which shaking table tests are most intensively applied. These tests permit the direct observation of the variation of acceleration amplification with height, of the critical failure acceleration, and of the progression of failure mechanisms in both soil and rock slopes. In a large-scale shaking table model test, the seismic behavior of a 30° sand slope was investigated; the slope response was found to remain linear up to a certain acceleration level (approximately 0.4g), beyond which nonlinear behavior set in and the failure surface developed shallowly, confined to the slope face; this finding is consistent with field observations of earthquake-induced landslides (Lin and Wang, 2006). The validity of the Newmark sliding-block method, widely employed in predicting slope deformations, has likewise been tested through shaking table experiments. In tests carried out on clayey slope models, the displacements computed by rigid sliding-block analysis were found to range between 27% and 225% of the measured values, remaining on average at roughly 75% of the measured values across the entire test series; the method was shown to yield its most reliable results in large-deformation cases in which post-peak strength governs the response (Wartman et al., 2005).

The seismic behaviour of rock slopes, particularly of bedding-type and toppling-type slopes, has been studied in detail. For a bedded rock slope, the acceleration amplification factor was found to increase with slope height, nonlinear response initiated near the crest once the input acceleration exceeded 0.2g, and progressive failure developed through four stages (He et al., 2021). In an experiment comparing steeply bedded and toppling-type slopes, an abrupt amplification effect was observed under vertical acceleration beyond thresholds of 0.6g for the bedded slope and 0.4g for the toppling-type slope (Li et al., 2019). For a rock slope containing a weak interlayer, nonlinear response emerged once the input amplitude exceeded 0.3g, and the counter-bedding configuration exhibited superior seismic stability relative to the bedding-parallel configuration (Fan et al., 2016). In a steeply bedded rock slope, the acceleration amplification factor reached its maximum at a frequency of 25 Hz, and the slope failed in a four-stage tension–shear sliding mode (Dong et al., 2022). Similarly, for slopes on a loess plateau, the peak acceleration amplification factor in the vicinity of cracks was shown to reach as high as 3.6 at the slope shoulder (Wu et al., 2020). In another study conducted from an energy perspective, damage was shown to influence the dynamic response by lowering the natural frequency of the slope and by altering the energy-transmission coefficient (Miao et al., 2024). For slopes in permafrost regions, the failure surface was found to develop as an integral slip along the soil–ice interface (Sun et al., 2017).

The seismic performance of measures for reinforcing slopes has also been assessed by means of these experiments. When a soil slope with multiple slip surfaces was reinforced with double-row anti-slide piles, distinct pressure distributions developed on the front-row and rear-row piles, and the dynamic earth pressure proved more sensitive to damping than to acceleration (Wu and Pai, 2022). In a 1:70 scale model of a bridge foundation reinforced with anti-slide piles together with a gravel landslide, the rear-row piles were shown to mitigate the effect of the landslide thrust on the bridge foundation (Zhang, C. et al., 2020). In a 1:20 scale model of a slope reinforced with anchor cables and a lattice beam, the reinforcement system was found to stabilise the middle and lower portions of the slope effectively as long as the peak ground acceleration did not exceed 0.5g (Zhang, J. et al., 2020).

Retaining Structures and Reinforced Soil Walls

Retaining structures are among the most extensively investigated applications of shaking table testing in geotechnical earthquake engineering, a fact that reflects the interest in experimentally understanding the superior performance that reinforced soil (geosynthetic-reinforced) walls exhibit during earthquakes. In early studies comparing geosynthetic-reinforced soil walls with conventional types (gravity, leaning, and cantilever walls), shaking table and tilting table tests were used in combination to determine the critical seismic acceleration coefficients of the various wall types, which were then compared with the predictions of pseudo-static design methods (Koseki et al., 1998; Matsuo et al., 1998). In wrap-faced and segmental reinforced wall models, lateral movement was shown to begin after a horizontal acceleration of 0.25g for wrap-faced walls and 0.45g for segmental walls (Ramakrishnan et al., 1998). In a study comparing six different wall types under irregular excitation, rigid-faced reinforced soil walls were shown to exhibit markedly more ductile behaviour than conventional walls (Watanabe et al., 2003). A typical arrangement in such tests consists of the reinforced backfill placed within a rigid container, the modular block/panel facing at the front face, a toe boundary element, and accelerometers positioned at various elevations, LVDTs measuring facing displacement, and strain gauges mounted on the reinforcement.

In large-scale benchmark tests of modular-block-faced reinforced soil walls, walls 2.8 m in height were subjected to Kobe earthquake records at a maximum horizontal acceleration of first 0.4g and then 0.86g; during the initial shaking the walls deformed only slightly with negligible amplification, and with an amplification ratio of 1.35 the system outperformed the conventional walls that had been tested (Ling et al., 2005). In a series of small-scale tests aimed at isolating the influence of the facing and the toe boundary condition on the seismic response, the horizontally restrained toe was shown to carry a substantial portion of the total horizontal earth load (30%–60%, depending on the reinforcement configuration), and the rigid facing column was found to play a critical role in resisting dynamic loads (El-Emam and Bathurst, 2005; El-Emam and Bathurst, 2007).

The influence of reinforcement parameters has been examined critically in numerous studies. In reinforced wall models one meter in height, it was concluded that the key parameter governing the seismic behaviour and deformation mode is the stiffness of the reinforcement rather than the ultimate tensile strength on which current codes are based (Sabermahani et al., 2009). In geogrid-reinforced rigid walls with saturated sand backfill, the geogrid was found to reduce the development of excess pore water pressure, and long-duration, high-acceleration waves arriving from the far field were shown to produce a greater effect than near-field waves (Wang et al., 2015). For steel-strip reinforced walls, the plastic displacement threshold was shown to be approximately 0.5g, and a critical reinforcement-length-to-wall-height ratio of about 0.7 was proposed for seismic conditions (Yazdandoust, 2017; Cao et al., 2018). In studies examining geocell-faced walls, battered-face walls were shown to perform markedly better than vertical-face walls, and the frequency content of the input motion proved decisive for performance (Latha and Manju, 2016; Krishnaraj et al., 2023). Factors affecting the seismic behaviour of cantilever and gravity walls (Zhu et al., 2019; Wei et al., 2022), the effect of EPS composite backfill (Gao et al., 2017), the contribution of cohesive backfill (Nakajima et al., 2021), and comparisons of various geogrid-reinforced wall types (Krishna and Latha, 2007; Qu et al., 2022; Hossain et al., 2024; Akbar et al., 2024) also form part of the extensive literature in this area; Akbar et al. (2024), for example, presented a representative shaking table configuration for a geogrid-reinforced wall model.

Soil Liquefaction and Remediation against Liquefaction

The liquefaction of saturated loose sands under cyclic loading and the damage it causes constitute one of the most critical topics in geotechnical earthquake engineering. Shaking table tests make it possible to investigate, in a realistic manner, the development of excess pore water pressure, liquefaction, and the effectiveness of remediation methods against liquefaction. In one of the early studies in the field, tests conducted on a large 12 m × 12 m shaking table demonstrated the effectiveness of gravel drains in preventing the liquefaction of sand layers; the drains were found to markedly reduce the uplift forces acting on buried and partially buried structures (Sasaki and Taniguchi, 1982). Factors influencing the liquefaction resistance of sands, such as acceleration, frequency, and relative density, have likewise been studied critically (Varghese and Madhavi Latha, 2014).

Large-scale liquefaction tests have allowed direct measurement of pore water pressure development and post-liquefaction settlement (Moss et al., 2020). The liquefaction-induced settlement of shallow foundations resting on liquefiable ground (Jahed Orang et al., 2021) and liquefaction-triggered submarine slope failure (Feng et al., 2023) have been examined through such tests; the shaking table and laminar box arrangement together with the instrumentation layout used in the study by Jahed Orang et al. (2021). Among remediation methods against liquefaction, a sand–granulated rubber mixture backfill to prevent the flotation of buried pipes (Ecemis et al., 2021), a gravel backfill countermeasure against pipeline uplift verified through full-scale tests (Ko et al., 2023), the biological improvement of sand (enzyme-induced carbonate precipitation and microbial desaturation) (Zhou et al., 2023; Peng et al., 2026), and prefabricated vertical drains to mitigate re-liquefaction under repeated earthquakes (Padmanabhan and Shanmugam, 2024) have been evaluated through shaking table tests. A common finding of these studies is that appropriately designed remediation methods can markedly reduce the excess pore water pressure ratio and liquefaction-induced deformations.

Piled and Deep Foundations

The seismic behaviour of piled foundations, especially in liquefiable and laterally spreading soils, is another area in which shaking table tests have been intensively applied. The contributions of inertial and kinematic interaction to pile stresses in piles with embedded caps have been separated by means of large-scale tests (Tokimatsu et al., 2005). The interaction between a pile group and a bridge structure in liquefiable soil was examined in a laminar shear box using real earthquake records (Tang et al., 2010); the effect of liquefaction-induced lateral spreading on pile groups was measured through near-full-scale tests conducted at E-Defense, one of the largest shaking table facilities in the world (Motamed et al., 2013). A typical arrangement in these tests comprises a saturated sand layer within a laminar shear box, a pile group equipped with a pile cap and superstructure mass, and accelerometers, pore water pressure transducers, and strain gauges on the pile shaft placed at various depths.

In three-dimensional numerical studies validated by large-scale tests that compared pile–superstructure systems in liquefiable and non-liquefiable soils, the pile bending moment was shown to increase markedly at the liquefiable site, with the largest moment developing at the interface between the loose and dense sand layers (Hussein and El Naggar, 2022). The behaviour of pile groups behind a quay wall under lateral spreading (Tang et al., 2014), the seismic performance of battered piles (Chen et al., 2020), the behaviour of model pile foundations in saturated sand (Unsever et al., 2017), and the failure behaviour of pile-group–superstructure systems at laterally spreading sites (Pan et al., 2023; Ebeido et al., 2019) are among the principal studies in this area. The dynamic behaviour of a single pile embedded in silty sand (SM) was examined comparatively for dry and saturated conditions; under saturated conditions, the natural frequency of the pile–soil system was shown to decrease markedly (Song and Jeong, 2023). For liquefaction mitigation, the effectiveness of ground improvement with colloidal silica for pile foundations (Krishnan and Shukla, 2022) and the contribution of micropiles have also been investigated; the effectiveness of micropiles was found to depend strongly on the frequency of the input motion, with reductions of up to 76% in free-field surface accelerations achieved under certain conditions (Ghassemi et al., 2025). The behaviour of large pile groups in liquefiable soil has also been addressed through centrifuge shaking table tests (Liu et al., 2018). A common pattern emerging from these studies is that, at liquefiable sites, the relative contributions of inertial loading, loss of lateral soil support, and kinematic loading from lateral spreading depend on the pile–soil–superstructure configuration and on the stage of liquefaction development. In addition, the dynamic performance of caisson-type coastal structures under liquefiable backfill conditions has been examined within this scope; EPS composite soil replacement was shown to improve caisson stability by slowing the development of excess pore water pressure (Gao et al., 2024). The fact that a substantial proportion of piled-foundation studies were carried out together with validated numerical models demonstrates that shaking table tests are used not only for phenomenological observation but also for the development of reliable design tools.

Tunnels and Buried Structures

Because the seismic behaviour of buried structures is governed by the kinematic interaction of the surrounding soil, the study of tunnel and buried-structure models on the shaking table is of particular importance. The seismic response of utility tunnels has been studied through the integrated use of experiments and finite element analysis (Jiang et al., 2010); in the behaviour of multi-storey metro stations under pulse-like ground motions, the centre columns in particular were identified as damage-prone members (Chen et al., 2016). The response of long tunnels under non-uniform seismic input was investigated using a 1/60 scale tunnel model on a 40-m-long multi-point shaking table array; under non-uniform excitation, the tunnel joint deformations were shown to grow markedly relative to uniform excitation, indicating that this effect must be taken into account in the seismic design of long tunnels (Yu et al., 2018). In a typical arrangement in this area, a tunnel lining embedded in the model soil within a rigid or laminar container is instrumented with strain gauges placed around the lining and accelerometers distributed at various elevations within the soil; in fault-crossing studies, the container is designed as a split box in order to reproduce the relative fault movement.

The behaviour of fault-crossing tunnels has been addressed through experiments using a three-dimensional fault-slip apparatus. In a study examining the effect of normal fault slip, the peak acceleration of the lining was found to be controlled by the presence of the fault and the direction of seismic excitation rather than by the fault slip itself (Fan et al., 2020); in tests examining different fault dip angles, the dynamic response was shown to intensify as the fault dip angle decreased (Zhu et al., 2021; Zhu et al., 2024). For a shallow segmental tunnel model in sandy soil, a benchmark 1g experimental data set was produced using Ricker wavelets (Yuan et al., 2020). In 1/20 scale tests of a prefabricated T-junction utility tunnel, the stiffness difference between the two tunnels was found to cause pronounced strain concentration in the junction region (Liang et al., 2023). The uplift behaviour of tunnels at stratified liquefiable sites (Yao et al., 2023), utility tunnels in non-homogeneous soils (Darli et al., 2021), the behaviour of metro stations near valleys (Yu et al., 2023), and the response of buried pipelines of differing stiffness (Chen et al., 2025) complement the literature in this area. Two important patterns emerging in most of these studies are noteworthy. First, because the behaviour of buried structures is largely determined by the kinematic forcing of the surrounding soil, the relative stiffness difference between the structure and the soil leads to pronounced strain concentrations, particularly at junctions and discontinuities; for example, in T-junction tunnels the axial strain amplification was measured to increase several-fold (Liang et al., 2023). Second, liquefaction-induced stiffness degradation may reduce the transmission of some high-frequency components; however, the accompanying loss of effective stress, excess pore-pressure build-up, and soil–structure relative displacement can substantially increase tunnel uplift and deformation-joint demands (Yao et al., 2023). These findings underscore the central importance of free-field soil behaviour and of the soil–structure stiffness ratio in the seismic design of buried structures.

Embankments, Dams, and Shallow Foundations

The seismic behaviour of geotechnical structures such as embankments and dams, together with the performance of shallow foundations, is among the classical application areas of shaking table tests. In early tests of embankments resting on liquefiable sandy ground, the soil beneath the embankment was observed not to liquefy, whereas the free-field soil liquefied readily; the spiky acceleration responses were shown to arise from the cyclic mobility effect (Koga and Matsuo, 1990). The dynamic behaviour of railway embankment slopes was investigated using 1:8 scale models (Lin and Yang, 2013); the performance of unreinforced embankment slopes and of those reinforced with different numbers of geogrid layers was compared under Wenchuan earthquake records (Lin et al., 2015). For railway embankments on liquefiable ground, the effect of embankment height and non-liquefiable layer thickness on settlement was quantified; settlement was shown to fall to negligible levels once the non-liquefiable layer thickness reached approximately 1.5 times the embankment height (Ha et al., 2023).

The dynamic response characteristics of tailings dams have been measured at various shaking intensities to investigate their failure mechanisms (Jin et al., 2020; Alshawmar and Fall, 2021); the effectiveness of in-ground seismic isolation provided by geosynthetic liners at solid-waste landfill sites has been assessed (Mirhaji et al., 2019). With respect to shallow foundations, the seismic performance of foundations on partially saturated sands (Zeybek, 2022), the behaviour of grout-improved sandy gravel foundations (Wang et al., 2022), and the response of reinforced fills over soft clay (Hore et al., 2021) have been examined. The favourable performance features of rocking shallow foundations, such as re-centering with little damage and energy dissipation, have been compiled in a publicly available database that includes 200 model case histories and combines five centrifuge and three 1g shaking table test series (Gavras et al., 2020). A prominent finding in studies in this area is that the phenomenon of liquefaction develops differently in the embankment and in the free-field soil: the soil beneath the embankment can be more resistant to liquefaction than the free field owing to the additional overburden pressure produced by the surcharge, whereas liquefaction of the free-field soil can lead to settlement and cracking in the embankment (Koga and Matsuo, 1990). In tailings dams, the acceleration amplification factor was found to increase with dam height and to decrease with peak ground acceleration, while the pore water pressure and earth pressure responses were closely related to the Arias intensity (Jin et al., 2020). These observations reveal that, in the seismic design of geotechnical structures such as embankments and dams, the liquefaction behaviour of the underlying foundation soil, and not merely the structure itself, must be assessed in an integrated manner.

Soil–Structure Interaction and Geotechnical Seismic Isolation

The role of soil–structure interaction (SSI) in the seismic response of structures and the use of soil as a seismic isolation medium are attracting increasing interest in current research. In experiments conducted with a single-degree-of-freedom structural model, the influence of the frequency and amplitude of the input motion and of the nonlinear behaviour of the soil on the coupled dynamic response of the system was demonstrated (Biondi et al., 2015). Within the scope of geotechnical seismic isolation (GSI), compressible EPS (geofoam) buffer layers used to reduce the dynamic loads acting on rigid retaining walls were found to provide greater load reduction as the buffer density decreased; in the most favourable case, the maximum dynamic force reduction reached about 31% at a peak acceleration of 0.7g (Bathurst et al., 2007; Zarnani and Bathurst, 2007).

In the tests by Erdinçliler and Yıldız (2023), sand–EPS-bead isolation layers were placed around the foundation. Among the investigated configurations, the EPS40 mixture with a 15 cm layer thickness produced the most pronounced reductions in peak acceleration and inter-storey drift; the building model, the instrumentation, and the experimental stages of that study are shown in Figure 2. The isolation performance of the rubber–sand mixture was evaluated as a function of rubber content, layer depth ratio, and soil relative density; the effect was found to be more pronounced under loose soil conditions, although an increase in layer thickness was accompanied by larger settlements (Golestani Ranjbar and Seyedi Hosseininia, 2024). In the isolation of electrical transformers using mixtures containing recycled waste tyre rubber, an average reduction of 35% was achieved in the strain response, the most critical performance indicator (Li et al., 2025). Also examined in this area are the effectiveness of stone columns as a countermeasure against liquefaction (Qu et al., 2016), the seismic behaviour of helical soil-nailed walls (Mollaei et al., 2022), EPS composite soil replacement in caisson structures (Gao et al., 2024), and the effect of water level in caisson quay walls with fibre-reinforced backfill (Tan et al., 2026); in the last study, a rise in water level at an input acceleration of 0.6g was found to increase the horizontal displacement by at least 476% relative to the dry-backfill case. A striking common feature of current research on geotechnical seismic isolation is its turn, driven by sustainability concerns, towards recycled waste materials (particularly rubber granules obtained from scrap vehicle tyres). It is emphasised that, owing to their high energy-absorption capacity and low lateral stiffness, these mixtures can form an isolation layer beneath the foundation that reduces the acceleration transmitted to the superstructure, but that a balance must be struck between isolation effectiveness and the accompanying increase in settlement. These findings show that geotechnical seismic isolation is a promising field of application from the standpoint of both earthquake safety and waste recovery.

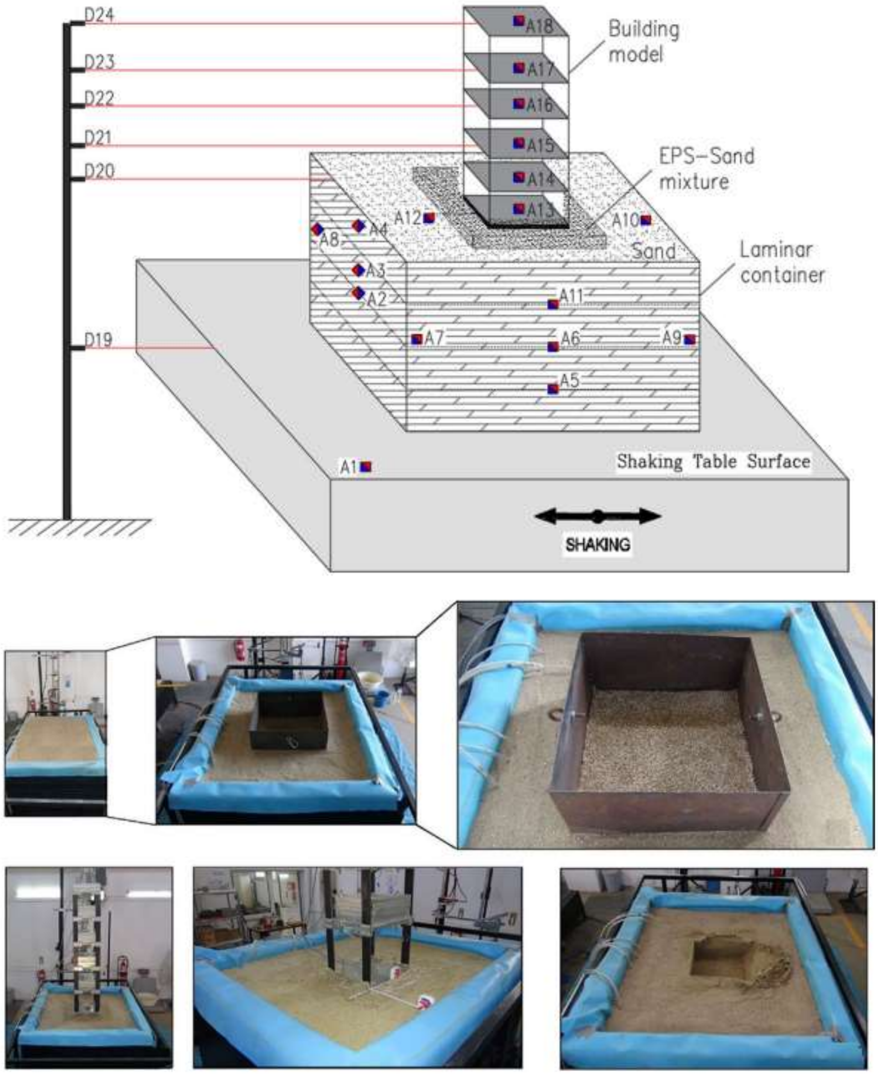

Figure 2: The building model and instrumentation, together with the various stages of experimental work
Source: Erdinçliler and Yildiz, 2023

GENERAL ASSESSMENT AND FUTURE RESEARCH DIRECTIONS

The literature reviewed in this chapter comprises 103 publications compiled in this chapter, which shows that shaking table tests have become an indispensable tool in almost every sub-field of geotechnical earthquake engineering. The principal strengths of the method are its capacity to accommodate large and complex model geometries, the direct observation it affords of failure mechanisms and progressive damage, its provision for rich instrumentation, and its generation of high-quality data for the validation of numerical models. Conversely, the inability to fully reproduce stress-level-dependent scale effects in the 1g domain, the boundary effects arising from finite model dimensions, and the sensitivity to the frequency content of the input motion are the principal limitations that require caution when extrapolating the results to the prototype.

Several common trends stand out from the compiled literature. First, laminar and biaxial shear box designs appear to be evolving continuously towards a more realistic simulation of free-field behaviour by reducing boundary effects. Second, in an increasing number of recent studies, shaking table tests are combined with numerical analyses, including three-dimensional nonlinear simulations, for calibration and validation purposes. Third, sustainability-oriented topics, such as geotechnical seismic isolation with recycled materials (waste tyre rubber, EPS) and biological ground improvement methods, are observed to be among the most dynamic research themes of recent years.

Several directions can be foreseen for future research. The prominent research needs include the comparative and complementary use of 1g shaking table and centrifuge tests in order to better control scale effects; the application of input motion as a multi-component (triaxial) and spatially variable excitation; the wider adoption of advanced measurement techniques such as digital image correlation and distributed fibre-optic sensing; and the investigation of the effect of the variable water-level conditions associated with climate change on the seismic performance of coastal and offshore structures. Furthermore, in Türkiye, in the light of the devastating earthquakes experienced in the recent past, conducting model tests representative of local soil conditions and the building stock at national shaking table facilities will make an important contribution both to the improvement of design codes and to the validation of numerical models under local conditions.

CONCLUSION

In this chapter, the use of shaking table tests in geotechnical engineering has been reviewed critically, starting from the theoretical foundations of the method and proceeding through seven principal application areas. The review has established that similitude rules and container design are the fundamental elements that determine the reliability of the method, and that in each of the areas of slope stability, retaining structures, liquefaction, piled foundations, tunnels, embankments, and soil–structure interaction, shaking table tests offer concrete contributions to the understanding of failure mechanisms and the development of design methods. Although the method's limitations regarding scale and boundary effects persist, its integrated use with numerical models and the advances in measurement techniques position shaking table tests, in future research, as one of the most valuable research tools in geotechnical earthquake engineering. The comprehensive bibliography compiled in this chapter is expected to serve as a reference for researchers and practitioners interested in the subject.

REFERENCES

Akbar, M., Pan, H., Huang, J., Arshid, M. U., Khan, Q. U. Z., Ou, G. and Ahmed, B. (2024). Seismic response comparison of various geogrid reinforced earth-retaining walls: based on shaking table and 3D FE analysis. *Scientific Reports*, 14, Article 24168. https://doi.org/10.1038/s41598-024-64203-4

Alshawmar, F. and Fall, M. (2021). Dynamic response of thickened tailings in shaking table testing. *International Journal of Geo-Engineering*, 12, Article 28.

Bagheri, O. and Eseller-Bayat, E. E. (2024). Laminar soil container's performance study for dynamic laboratory tests: comprehensive review and numerical verification. *KSCE Journal of Civil Engineering*, 28(7), 2705-2721. https://doi.org/10.1007/s12205-024-1122-4

Bathurst, R. J., Zarnani, S. and Gaskin, A. (2007). Shaking table testing of geofoam seismic buffers. *Soil Dynamics and Earthquake Engineering*, 27(4), 324-332. https://doi.org/10.1016/j.soildyn.2006.08.003

Bhattacharya, S., Lombardi, D., Dihoru, L., Dietz, M. S., Crewe, A. J. and Taylor, C. A. (2012). Model container design for soil-structure interaction studies. *Role of Seismic Testing Facilities in Performance-Based Earthquake Engineering (Springer, book chapter)*, GGEE 22, 135-158. https://doi.org/10.1007/978-94-007-1977-4_8

Biondi, G., Massimino, M. R. and Maugeri, M. (2015). Experimental study in the shaking table of the input motion characteristics in the dynamic SSI of a SDOF model. *Bulletin of Earthquake Engineering*, 13(6), 1835-1869. https://doi.org/10.1007/s10518-014-9696-8

Cao, L. C., Fu, X., Wang, Z. J., Zhou, Y. Y., Liu, F. C. and Zhang, J. J. (2018). Seismic responses of the steel-strip reinforced soil retaining wall with full-height rigid facing from shaking table test. *Journal of Mountain Science*, 15(5), 1137-1152. https://doi.org/10.1007/s11629-017-4598-2

Castelli, F., Grasso, S., Lentini, V. and Sammito, M. S. V. (2022). Design of a biaxial laminar shear box for 1g shaking table tests. *Geotechnics*, 2(2), 467-487. https://doi.org/10.3390/geotechnics2020023

Chen, Z. Y., Chen, W., Li, Y. Y. and Yuan, Y. (2016). Shaking table test of a multi-story subway station under pulse-like ground motions. *Soil Dynamics and*

Earthquake Engineering, 82, 111-122. https://doi.org/10.1016/j.soildyn.2015.12.002

Chen, W., Ma, J., Cao, S., Wang, Q. and Wang, M. (2020). Shaking table test study on seismic performance of inclined pile foundations in liquefiable soil. *Environmental Earth Sciences*, 79(17), Article 398. https://doi.org/10.1007/s12665-020-09139-4

Chen, H., Cui, J., Li, Y., Ouyang, Z., Huang, X. and Shan, Y. (2025). Seismic response analysis of buried pipelines with varying stiffness by shaking table tests. *Earthquake Engineering and Engineering Vibration*, 24(2), 583-594. https://doi.org/10.1007/s11803-025-2322-8

Darli, C., M., Tang, A., Huang, D. and Zhang, J. (2021). Large scale shaking table model test and analysis on seismic response of utility tunnel in non-homogeneous soil. *Earthquake Engineering and Engineering Vibration*, 20(2), 505-515. https://doi.org/10.1007/s11803-021-2035-6

Dong, J., Wang, C., Huang, Z., Yang, J. and Xue, L. (2022). Shaking table model test to determine dynamic response characteristics and failure modes of steep bedding rock slope. *Rock Mechanics and Rock Engineering*, 55(6), 3645-3658. https://doi.org/10.1007/s00603-022-02822-x

Ebeido, A., Elgamal, A., Tokimatsu, K. and Abe, A. (2019). Pile and pile-group response to liquefaction-induced lateral spreading in four large-scale shake-table experiments. *Journal of Geotechnical and Geoenvironmental Engineering*, 145(10), 04019080. https://doi.org/10.1061/(ASCE)GT.1943-5606.0002142

Ecemis, N., Valizadeh, H. and Karaman, M. (2021). Sand-granulated rubber mixture to prevent liquefaction-induced uplift of buried pipes: a shaking table study. *Bulletin of Earthquake Engineering*, 19(7), 2817-2838. https://doi.org/10.1007/s10518-021-01091-3

Erdincliler, A. and Yildiz, O. (2023). Shaking table tests on geotechnical seismic isolation for medium-rise buildings using EPS beads-sand mixtures. *Bulletin of Earthquake Engineering*, 21(8), 3851-3877. https://doi.org/10.1007/s10518-022-01587-6

El-Emam, M. M. and Bathurst, R. J. (2005). Facing contribution to seismic response of reduced-scale reinforced soil walls. *Geosynthetics International*, 12(5), 215-238. https://doi.org/10.1680/gein.2005.12.5.215

El-Emam, M. M. and Bathurst, R. J. (2007). Influence of reinforcement parameters on the seismic response of reduced-scale reinforced soil retaining walls. *Geotextiles and Geomembranes*, 25(1), 33-49. https://doi.org/10.1016/j.geotexmem.2006.09.001

Fan, G., Zhang, J., Wu, J. and Yan, K. (2016). Dynamic response and dynamic failure mode of a weak intercalated rock slope using a shaking table. *Rock Mechanics and Rock Engineering*, 49(8), 3243-3256. https://doi.org/10.1007/s00603-016-0971-7

Fan, L., Chen, J., Peng, S., Qi, B., Zhou, Q. and Wang, F. (2020). Seismic response of tunnel under normal fault slips by shaking table test technique. *Journal of Central South University*, 27(4), 1306-1319. https://doi.org/10.1007/s11771-020-4368-0

Fan, Z., Yuan, Y., Cudmani, R., Deng, J., Chrisopoulos, S., Vogt, S. and Niebler, M. (2024). Large biaxial laminar shear box for 1-g shaking table tests on saturated sand. *Soil Dynamics and Earthquake Engineering*, 183, 108756. https://doi.org/10.1016/j.soildyn.2024.108756

Feng, X., Ye, B., He, J., Miao, H. and Lin, C. (2023). Shaking table test on underwater slope failure induced by liquefaction. *Soils and Foundations*, 63, 101357. https://doi.org/10.1016/j.sandf.2023.101357

Gao, H., Hu, Y., Wang, Z., Wang, C. and Chen, G. (2017). Shaking table tests on the seismic performance of a flexible wall retaining EPS composite soil. *Bulletin of Earthquake Engineering*, 15(12), 5481-5510. https://doi.org/10.1007/s10518-017-0189-4

Gao, H., Ji, Z., Zhang, X., Zhang, S., Wang, Z. and Shen, G. (2024). Evaluation of the effects of EPS composite soil replacement on the dynamic performance of caisson structure using shaking table tests. *Earthquake Engineering and Engineering Vibration*, 23(4), 829-843. https://doi.org/10.1007/s11803-024-2275-3

Gavras, A. G., Kutter, B. L., Hakhamaneshi, M., Gajan, S., Tsatsis, A., Sharma, K. et al. (2020). Database of rocking shallow foundation performance: dynamic shaking. *Earthquake Spectra*, 36(2), 960-982. https://doi.org/10.1177/8755293019891727

Ghassemi, S., Ekraminia, S. S., Hajialilue-Bonab, M., Tohidvand, H. R., Azarafza, M. and Derakhshani, R. (2025). Innovative insights into micropile seismic response: shaking table tests reveal critical dependencies and liquefaction mitigation. *Bulletin of Engineering Geology and the Environment*, 84(4), Article 206. https://doi.org/10.1007/s10064-025-04225-y

Golestani Ranjbar, E. and Seyedi Hosseininia, E. (2024). Seismic performance of rubber-sand mixture as a geotechnical seismic isolation system using shaking table test. *Soil Dynamics and Earthquake Engineering*, 177, Article 108395. https://doi.org/10.1016/j.soildyn.2023.108395

Ha, I. S., Oh, I. T. and Yoo, M. (2023). Analysis of factors affecting railway settlement of embankment section due to liquefaction using 1-g shaking table model tests. *KSCE Journal of Civil Engineering*, 27(7), 2822-2833. https://doi.org/10.1007/s12205-023-2133-2

He, J., Qi, S., Zhan, Z., Guo, S., Li, C., Zheng, B. et al. (2021). Seismic response characteristics and deformation evolution of the bedding rock slope using a large-scale shaking table. *Landslides*, 18(8), 2835-2853. https://doi.org/10.1007/s10346-021-01682-w

Hore, R., Chakraborty, S. and Ansary, M. A. (2021). Seismic response of embankment on soft clay based on shaking table test. *International Journal of Geosynthetics and Ground Engineering*, 7(1), Article 3. https://doi.org/10.1007/s40891-020-00246-7

Hossain, M. Z., Hore, R. and Ansary, M. A. (2024). Model tests of reinforced soil retaining sand walls by shaking table test. *Arabian Journal of Geosciences*, 17, Article 166. https://doi.org/10.1007/s12517-024-11965-w

Hussein, A. F. and El Naggar, M. H. (2022). Seismic behaviour of piles in non-liquefiable and liquefiable soil. *Bulletin of Earthquake Engineering*, 20(1), 77-111. https://doi.org/10.1007/s10518-021-01244-4

Iai, S. (1989). Similitude for shaking table tests on soil-structure-fluid model in 1g gravitational field. *Soils and Foundations*, 29(1), 105-118. https://doi.org/10.3208/sandf1972.29.105

Iai, S., Tobita, T. and Nakahara, T. (2005). Generalised scaling relations for dynamic centrifuge tests. *Geotechnique*, 55(5), 355-362. https://doi.org/10.1680/geot.2005.55.5.355

Jahed Orang, M., Motamed, R., Prabhakaran, A. and Elgamal, A. (2021). Large-scale shake table tests on a shallow foundation in liquefiable soils. *Journal of Geotechnical and Geoenvironmental Engineering*, 147(1). https://doi.org/10.1061/(ASCE)GT.1943-5606.0002427

Jiang, L., Chen, J. and Li, J. (2010). Seismic response of underground utility tunnels: shaking table testing and FEM analysis. *Earthquake Engineering and Engineering Vibration*, 9(4), 555-567. https://doi.org/10.1007/s11803-010-0037-x

Jin, J., Ding, Q., Cui, H., Zhang, P., Xiao, X. and Lv, X. (2020). Dynamic response characteristics of a tailing dam determined by shaking-table tests. *Arabian Journal of Geosciences*, 13(18), Article 897. https://doi.org/10.1007/s12517-020-05878-7

Kim, H., Kim, D., Lee, Y. and Kim, H. (2020). Effect of soil box boundary conditions on dynamic behavior of model soil in 1 g shaking table test. *Applied Sciences*, 10(13), 4642. https://doi.org/10.3390/app10134642

Ko, Y. Y., Tsai, T. Y. and Jheng, K. Y. (2023). Full-scale shaking table tests on soil liquefaction-induced uplift of buried pipelines for buildings. *Earthquake Engineering & Structural Dynamics*, 52(5), 1486-1510. https://doi.org/10.1002/eqe.3826

Koga, Y. and Matsuo, O. (1990). Shaking table tests of embankments resting on liquefiable sandy ground. *Soils and Foundations*, 30(4), 162-174. https://doi.org/10.3208/sandf1972.30.4_162

Koseki, J., Munaf, Y., Tatsuoka, F., Tateyama, M., Kojima, K. and Sato, T. (1998). Shaking and tilt table tests of geosynthetic-reinforced soil and conventional-type retaining walls. *Geosynthetics International*, 5(1-2), 73-96. https://doi.org/10.1680/gein.5.0115

Krishna, A. M. and Latha, G. M. (2007). Seismic response of wrap-faced reinforced soil-retaining wall models using shaking table tests. *Geosynthetics International*, 14(6), 355-364. https://doi.org/10.1680/gein.2007.14.6.355

Krishnan, J. and Shukla, S. (2022). Shake table testing of liquefaction mitigation efficiency on pile foundations in sand stabilised with colloidal silica. *Natural Hazards*, 111(3), 2317-2341. https://doi.org/10.1007/s11069-021-05139-0

Krishnaraj, P., Manju, G. S. and Latha, G. M. (2023). Physical and numerical shaking table studies on geocell-reinforced retaining walls. *International Journal of Geosynthetics and Ground Engineering*, 9(5), Article 62. https://doi.org/10.1007/s40891-023-00482-7

Latha, G. M. and Manju, G. S. (2016). Seismic response of geocell retaining walls through shaking table tests. *International Journal of Geosynthetics and Ground Engineering*, 2(1), Article 7. https://doi.org/10.1007/s40891-016-0048-4

Lei, M., Zhou, B., Lin, Y., Chen, F., Shi, C. and Peng, L. (2020). Model test to investigate reasonable reactive artificial boundary in shaking table test with a rigid container. *Journal of Central South University*, 27(1), 210-220. https://doi.org/10.1007/s11771-020-4289-y

Li, L., Ju, N., Zhang, S. and Deng, X. (2019). Shaking table test to assess seismic response differences between steep bedding and toppling rock slopes. *Bulletin of Engineering Geology and the Environment*, 78(1), 519-531. https://doi.org/10.1007/s10064-017-1186-1

Li, S., Tsang, H. H. and Cheng, Y. (2025). Shaking table tests on geotechnical seismic isolation of electrical transformers using recycled tire rubber-soil mixtures.

Construction and Building Materials, Article 143886. https://doi.org/10.1016/j.conbuildmat.2025.143886
Liang, J., Zhang, J., Dong, B., Xu, A. and Ba, Z. (2023). Shaking table tests on the seismic performance of prefabricated T-shaped cross utility tunnel. *Structures*, 58, 105516. https://doi.org/10.1016/j.istruc.2023.105516
Lin, M. L. and Wang, K. L. (2006). Seismic slope behavior in a large-scale shaking table model test. *Engineering Geology*, 86(2-3), 118-133. https://doi.org/10.1016/j.enggeo.2006.02.011
Lin, Y. L. and Yang, G. L. (2013). Dynamic behavior of railway embankment slope subjected to seismic excitation. *Natural Hazards*, 69(1), 219-235. https://doi.org/10.1007/s11069-013-0701-3
Lin, Y. L., Leng, W. M., Yang, G. L., Li, L. and Yang, J. S. (2015). Seismic response of embankment slopes with different reinforcing measures in shaking table tests. *Natural Hazards*, 76(2), 791-810. https://doi.org/10.1007/s11069-014-1517-5
Ling, H. I., Mohri, Y., Leshchinsky, D., Burke, C., Matsushima, K. and Liu, H. (2005). Large-scale shaking table tests on modular-block reinforced soil retaining walls. *Journal of Geotechnical and Geoenvironmental Engineering*, 131(4), 465-476. https://doi.org/10.1061/(ASCE)1090-0241(2005)131:4(465)
Liu, X., Wang, R. and Zhang, J. M. (2018). Centrifuge shaking table tests on 4x4 pile groups in liquefiable ground. *Acta Geotechnica*, 13(6), 1405-1418. https://doi.org/10.1007/s11440-018-0699-5
Matsuo, O., Tsutsumi, T., Yokoyama, K. and Saito, Y. (1998). Shaking table tests and analyses of geosynthetic-reinforced soil retaining walls. *Geosynthetics International*, 5(1-2), 97-126. https://doi.org/10.1680/gein.5.0116
Miao, S., Su, L., Zhang, C., Liu, Z., Wang, B. and Dong, Z. (2024). Dynamic response characteristics and damage failure process of bedding rock slope in shaking table test. *Bulletin of Engineering Geology and the Environment*, 83(9), Article 358. https://doi.org/10.1007/s10064-024-03843-2
Mirhaji, V., Jafarian, Y., Baziar, M. H. and Jafari, M. K. (2019). Seismic in-soil isolation of solid waste landfill using geosynthetic liners: shaking table modeling of Tehran landfill. *International Journal of Civil Engineering*, 17(2), 205-217. https://doi.org/10.1007/s40999-017-0232-5
Mittal, V. and Samanta, M. (2025). Performance of a laminar shear box for cohesionless soil under seismic excitations. *Geotechnical and Geological Engineering*, 43(2), Article 60. https://doi.org/10.1007/s10706-024-02973-4
Mollaei, R., Yazdandoust, M. and Askari, F. (2022). Seismic evaluation of helical soil-nailed walls using shaking table testing. *Soil Dynamics and Earthquake Engineering*, 163, 107331. https://doi.org/10.1016/j.soildyn.2022.107331
Moss, R. E. S., Honnette, T. R. and Jacobs, J. S. (2020). Large-scale liquefaction and postliquefaction shake table testing. *Journal of Geotechnical and Geoenvironmental Engineering*, 146(12). https://doi.org/10.1061/(ASCE)GT.1943-5606.0002400
Motamed, R., Towhata, I., Honda, T., Tabata, K. and Abe, A. (2013). Pile group response to liquefaction-induced lateral spreading: E-Defense large shake table test. *Soil Dynamics and Earthquake Engineering*, 51, 35-46. https://doi.org/10.1016/j.soildyn.2013.04.007
Muir Wood, D., Crewe, A. and Taylor, C. (2002). Shaking table testing of geotechnical models. *International Journal of Physical Modelling in Geotechnics*, 2(1), 1-13. https://doi.org/10.1680/ijpmg.2002.020101

Nakajima, S., Ozaki, T. and Sanagawa, T. (2021). 1g shaking table model tests on seismic active earth pressure acting on retaining wall with cohesive backfill soil. *Soils and Foundations*, 61(5), 1251-1272. https://doi.org/10.1016/j.sandf.2021.06.014

Padmanabhan, G. and Shanmugam, G. K. (2024). Performance assessment of prefabricated vertical drains in mitigating soil reliquefaction subjected to repeated seismic events using shaking table experiments. *Frontiers of Structural and Civil Engineering*, 18(3), 411-427. https://doi.org/10.1007/s11709-024-1057-3

Pan, R., Xu, C., Jia, K., Dou, P. and Kamran, I. (2023). Large-scale shaking table test and three-dimensional numerical simulation research on earthquake seismic failure response of laterally spreading site-pile group-superstructure system. *Bulletin of Earthquake Engineering*, 21(10), 4789-4819. https://doi.org/10.1007/s10518-023-01713-y

Peng, Y., Yang, Y., Zhang, S., Hu, J., Ren, J. and Xue, X. (2026). Seismic response of liquefiable marine sand treated by microbially induced desaturation through shaking table tests. *Buildings*, 16(7), 1463. https://doi.org/10.3390/buildings16071463

Qu, M., Xie, Q., Cao, X., Zhao, W., He, J. and Jin, J. (2016). Model test of stone columns as liquefaction countermeasure in sandy soils. *Frontiers of Structural and Civil Engineering*, 10(4), 481-487. https://doi.org/10.1007/s11709-016-0355-9

Qu, H., Huang, X., Gao, Y., Zhang, Z. and Wang, C. (2022). Shaking table test of subgrade slope reinforced by gravity retaining wall with geogrids. *Earthquake Engineering and Engineering Vibration*, 21(3), 715-727. https://doi.org/10.1007/s11803-022-2108-1

Ramakrishnan, S., Budhu, M. and Britto, A. (1998). Laboratory seismic tests of geotextile wrap-faced and geotextile-reinforced segmental retaining walls. *Geosynthetics International*, 5(1-2), 55-71. https://doi.org/10.1680/gein.5.0114

Sabermahani, M., Ghalandarzadeh, A. and Fakher, A. (2009). Experimental study on seismic deformation modes of reinforced-soil walls. *Geotextiles and Geomembranes*, 27(2), 121-136. https://doi.org/10.1016/j.geotexmem.2008.09.009

Sasaki, Y. and Taniguchi, E. (1982). Shaking table tests on gravel drains to prevent liquefaction of sand deposits. *Soils and Foundations*, 22(3), 1-14. https://doi.org/10.3208/sandf1972.22.3_1

Shi, W., Chen, W., Lin, Y. and Wu, Y. (2021). Fabrication and testing of a laminar shear soil box for a shaking-table test. *Practice Periodical on Structural Design and Construction*, 26(4), 04021030. https://doi.org/10.1061/(ASCE)SC.1943-5576.0000600

Song, S. and Jeong, S. (2023). Dynamic analysis of a single pile embedded in SM soil using 1-g shaking table tests. *Ocean Engineering*, 285, 115416. https://doi.org/10.1016/j.oceaneng.2023.115416

Sun, H., Niu, F., Zhang, K. and Ge, X. (2017). Seismic behaviors of soil slope in permafrost regions using a large-scale shaking table. *Landslides*, 14(4), 1513-1520. https://doi.org/10.1007/s10346-017-0823-x

Tan, J., Geng, X., Ren, F., Huang, Q. and Shen, C. (2026). Influence of water level on seismic behavior of caisson quay walls with fiber-reinforced calcareous sand backfill. *Acta Geotechnica*, 21, 1773-1792. https://doi.org/10.1007/s11440-025-02823-4

Tang, L., Ling, X., Xu, P., Gao, X. and Wang, D. (2010). Shake table test of soil-pile groups-bridge structure interaction in liquefiable ground. *Earthquake Engineering and Engineering Vibration*, 9(1), 39-50. https://doi.org/10.1007/s11803-009-8131-7

Tang, L., Zhang, X., Ling, X., Su, L. and Liu, C. (2014). Response of a pile group behind quay wall to liquefaction-induced lateral spreading: a shake-table investigation. *Earthquake Engineering and Engineering Vibration*, 13(4), 741-749. https://doi.org/10.1007/s11803-014-0263-8

Tokimatsu, K., Suzuki, H. and Sato, M. (2005). Effects of inertial and kinematic interaction on seismic behavior of pile with embedded foundation. *Soil Dynamics and Earthquake Engineering*, 25(7-10), 753-762. https://doi.org/10.1016/j.soildyn.2004.11.018

Towhata, I. (2008). Geotechnical Earthquake Engineering. *Springer Series in Geomechanics and Geoengineering (book)*. https://doi.org/10.1007/978-3-540-35783-4

Turan, A., Hinchberger, S. D. and El Naggar, M. H. (2009). Design and commissioning of a laminar soil container for use on small shaking tables. *Soil Dynamics and Earthquake Engineering*, 29(2), 404-414. https://doi.org/10.1016/j.soildyn.2008.04.003

Unsever, Y. S., Matsumoto, T., Esashi, K. and Kobayashi, S. (2017). Behaviour of model pile foundations under dynamic loads in saturated sand. *Bulletin of Earthquake Engineering*, 15(4), 1355-1373. https://doi.org/10.1007/s10518-016-0029-y

Varghese, R. M. and Madhavi Latha, G. (2014). Shaking table tests to investigate the influence of various factors on the liquefaction resistance of sands. *Natural Hazards*, 73(3), 1337-1351. https://doi.org/10.1007/s11069-014-1142-3

Wang, L., Chen, G. and Chen, S. (2015). Experimental study on seismic response of geogrid reinforced rigid retaining walls with saturated backfill sand. *Geotextiles and Geomembranes*, 43(1), 35-45. https://doi.org/10.1016/j.geotexmem.2014.11.006

Wang, T., Liang, Y., Zhang, X. and Chen, S. (2022). Investigation of the seismic behavior of grouted sandy gravel foundations using shaking table tests. *Frontiers of Structural and Civil Engineering*, 16, 1196-1211. https://doi.org/10.1007/s11709-022-0865-6

Wartman, J., Seed, R. B. and Bray, J. D. (2005). Shaking table modeling of seismically induced deformations in slopes. *Journal of Geotechnical and Geoenvironmental Engineering*, 131(5), 610-622. https://doi.org/10.1061/(ASCE)1090-0241(2005)131:5(610)

Watanabe, K., Munaf, Y., Koseki, J., Tateyama, M. and Kojima, K. (2003). Behaviors of several types of model retaining walls subjected to irregular excitation. *Soils and Foundations*, 43(5), 13-27. https://doi.org/10.3208/sandf.43.5_13

Wei, M., Luo, Q., Feng, G., Wang, T. and Jiang, L. (2022). Shaking table tests on a cantilever retaining wall with reinforced and unreinforced backfill. *Journal of Zhejiang University-SCIENCE A*, 23(11), 900-916. https://doi.org/10.1631/jzus.A2200192

Wu, Z., Zhao, D., Che, A., Chen, D. and Liang, C. (2020). Dynamic response characteristics and failure mode of slopes on the loess tableland using a shaking-

table model test. *Landslides*, 17(7), 1561-1575. https://doi.org/10.1007/s10346-020-01373-y
Wu, H. and Pai, L. (2022). Shaking table test for reinforcement of soil slope with multiple sliding surfaces by reinforced double-row anti-slide piles. *Journal of Mountain Science*, 19(5), 1419-1436. https://doi.org/10.1007/s11629-021-7046-2
Xu, C., Jiang, Z., Du, X., Deng, L. and Li, Z. (2022). Property estimation of free-field sand in 1-g shaking table tests. *Earthquake Engineering and Engineering Vibration*, 21(3), 591-604. https://doi.org/10.1007/s11803-022-2105-4
Yao, A., Tian, T., Gong, Y. and Li, H. (2023). Shaking table tests of seismic response of multi-segment utility tunnels in a layered liquefiable site. *Sustainability*, 15(7), Article 6030. https://doi.org/10.3390/su15076030
Yazdandoust, M. (2017). Investigation on the seismic performance of steel-strip reinforced-soil retaining walls using shaking table test. *Soil Dynamics and Earthquake Engineering*, 97, 216-232. https://doi.org/10.1016/j.soildyn.2017.03.011
Yu, H., Yan, X., Bobet, A., Yuan, Y., Xu, G. and Su, Q. (2018). Multi-point shaking table test of a long tunnel subjected to non-uniform seismic loadings. *Bulletin of Earthquake Engineering*, 16(2), 1041-1059. https://doi.org/10.1007/s10518-017-0223-6
Yu, H., Wang, Z., Zhang, Z., Song, Y., Liu, S. and Jiang, W. (2023). Shaking table test for near-valley subway station - Part II: Seismic response of the station. *Soil Dynamics and Earthquake Engineering*, 172, 108065. https://doi.org/10.1016/j.soildyn.2023.108065
Yuan, Y., Yang, Y., Zhang, S., Yu, H. and Sun, J. (2020). A benchmark 1 g shaking table test of shallow segmental mini-tunnel in sand. *Bulletin of Earthquake Engineering*, 18(11), 5383-5412. https://doi.org/10.1007/s10518-020-00909-w
Zarnani, S. and Bathurst, R. J. (2007). Experimental investigation of EPS geofoam seismic buffers using shaking table tests. *Geosynthetics International*, 14(3), 165-177. https://doi.org/10.1680/gein.2007.14.3.165
Zeybek, A. (2022). Shaking table tests on seismic performance of shallow foundations resting on partially saturated sands. *Arabian Journal of Geosciences*, 15, Article 774. https://doi.org/10.1007/s12517-022-10032-6
Zhang, C., Jiang, G., Lei, D., Asghar, A., Su, L. and Wang, Z. (2020). Large-scale shaking table test on seismic behaviour of anti-slide pile-reinforced bridge foundation and gravel landslide: a case study. *Bulletin of Engineering Geology and the Environment*, 79(2), 1303-1316. https://doi.org/10.1007/s10064-020-02006-3
Zhang, J., Niu, J., Fu, X., Cao, L. and Xie, Q. (2020). Shaking table test of seismic responses of anchor cable and lattice beam reinforced slope. *Journal of Mountain Science*, 17(5), 1251-1268. https://doi.org/10.1007/s11629-019-5712-4
Zhou, Y., Zhang, Y., Geng, W., He, J. and Gao, Y. (2023). Evaluation of liquefaction resistance for single- and multi-phase SICP-treated sandy soil using shaking table test. *Acta Geotechnica*, 18(11), 6007-6025. https://doi.org/10.1007/s11440-023-02008-x
Zhu, H. W., Yao, L. K. and Li, J. (2019). Influence factors on the seismic behavior and deformation modes of gravity retaining walls. *Journal of Mountain Science*, 16(1), 168-178. https://doi.org/10.1007/s11629-018-5009-z

Zhu, D., Zhu, Z., Zhang, C. and Xie, X. (2021). Shaking table test on the tunnel dynamic response under different fault dip angles. *Symmetry*, 13(8), Article 1375. https://doi.org/10.3390/sym13081375

Zhu, D., Zhu, Z., Dai, L., Zhang, C. and Wang, B. (2024). Seismic response mechanism of near fault tunnel: theoretical analysis and shaking table test. *KSCE Journal of Civil Engineering*, 28(7), 2681-2693. https://doi.org/10.1007/s12205-024-0924-8

Artificial Intelligence for Automated Construction Schedule Generation: A Recommendation-Based Directed Graph Framework

Bayram ATEŞ[1]

Mohammad Azim EIRGASH[2*]

1- PhD, Civil Engineering Department, Karadeniz Technical University, 61080 Trabzon, Türkiye, Email: bayramates61@hotmail.com, ORCID: 0000-0002-1251-7053
2- PhD, Civil Engineering Department, Karadeniz Technical University, 61080 Trabzon, Türkiye, Email: azim.eirgash@ktu.edu.tr, ORCID: https://orcid.org/0000-0001-5399-115X (corresponding author)*

ABSTRACT

Construction activity sequencing is a fundamental component of project planning because it directly influences project duration, cost, resource utilization, and overall project performance. Conventional scheduling methods rely heavily on expert judgment and the manual definition of precedence relationships, making schedule development labor-intensive, time-consuming, and susceptible to inconsistency and human error. Recent advances in artificial intelligence and graph-based machine learning provide new opportunities to automate this process by learning activity dependencies from historical project data. This chapter presents a recommendation-based directed graph framework for automated construction schedule generation. Construction schedules are represented as directed acyclic graphs (DAGs), where activities are modeled as nodes and precedence relationships as directed edges. Instead of treating activity sequencing as a multi-class classification problem, the proposed framework formulates it as a recommendation task that generates ranked successor activities by exploiting graph topology and learned structural relationships. To establish the methodological foundation, the chapter reviews graph representations, recommendation systems, association rule mining, graph embedding techniques (DeepWalk and node2vec), and graph neural network architectures, including Graph Convolutional Networks (GCN), Graph Attention Networks (GAT), and GraphSAGE. An illustrative benchmark case involving seven construction activities demonstrates the framework workflow. The generated activity sequence is validated using the Critical Path Method (CPM), producing a feasible schedule with a duration of 69 days and a total cost of $228,400. As a proof of concept, the GAT model achieves the highest successor prediction recommendation similarity score (0.95) among the evaluated GNN models. Overall, the proposed framework provides a practical foundation for intelligent, data-driven, and automated construction schedule generation in future research and real-world applications.

Keywords – Construction scheduling; Activity sequencing; Artificial intelligence; Recommendation systems; Directed graph; Graph embedding; DeepWalk; node2vec; Graph Neural Networks; Automated schedule generation.

INTRODUCTION

Construction activity sequencing, the process of determining the logical order in which project tasks are executed, is a cornerstone of project planning and control. The quality of the schedule directly influences project duration, cost, resource utilization, and overall project success. Despite the widespread adoption of commercial scheduling tools such as Primavera P6 and Microsoft Project, the definition of precedence relationships remains a predominantly manual activity, relying heavily on the expertise of experienced schedulers (Yao et al., 2024; Zhang et al., 2026). This manual process is not only time-consuming but also inherently subjective, leading to inconsistencies across projects and organizations.

The construction industry is increasingly generating vast amounts of digital data from Building Information Modeling (BIM), enterprise resource planning (ERP) systems, project management platforms, and field sensors. These historical schedules encapsulate valuable knowledge about typical activity sequences and dependencies across different project types, yet this knowledge is rarely exploited in a systematic manner (Zhang et al., 2026; Al-Sinan et al., 2024). Artificial intelligence (AI) provides an unprecedented opportunity to mine this data and automatically generate scheduling recommendations (Yao et al., 2024; Boje et al., 2020).

Among the various AI paradigms, graph-based machine learning has emerged as particularly suitable for construction scheduling because project networks naturally map to directed graphs (Al-Sinan et al., 2024). Activities correspond to nodes, and precedence relationships become directed edges. In such a graph, the problem of predicting the next activity given the current one can be framed as a link prediction task, a classic problem in network science (Grover and Leskovec, 2016; Perozzi et al., 2014).

Traditional machine learning approaches often model activity prediction as multi-class classification, where the model chooses a single "correct" successor. However, this formulation suffers from several drawbacks: (i) historical datasets are highly sparse, with many activity pairs appearing only rarely (Amer et al., 2021); (ii) class imbalance is severe because some successors are far more common than others; and (iii) in practice, multiple successors may be feasible, and a single deterministic answer is often insufficient for planners who need to consider project-specific constraints (Boje et al., 2020; Amer et al., 2021).

To address these challenges, a recommendation-based directed graph framework is suggested. Instead of classifying a single successor, we rank candidate activities by their likelihood of following the current activity (Amer et al., 2021). This ranking approach aligns with real-world planning, where schedulers evaluate a set of plausible next steps before making a final choice. The framework leverages both shallow graph embedding techniques (Perozzi et al., 2014; Grover and Leskovec, 2016) and deep Graph Neural Networks (Kipf and Welling, 2017; Hamilton et al., 2017) to learn structural patterns from historical schedules (Zhou et al., 2020; Wu et al., 2021; Boje et al., 2020). Recent advances in artificial intelligence (AI), graph representation learning, and recommendation systems offer a paradigm shift. Rather than viewing activity sequencing as a static, manual drafting task, it can be modeled as an intelligent data-driven automation process (Le and Jeong, 2020). Construction schedules inherently possess a network topology. By representing historical project data as directed graphs, machine learning models can extract underlying patterns, contextual dependencies, and standard structural transitions between construction phases.

This chapter presents a recommendation-based directed graph framework for automating construction schedule generation by reformulating activity sequencing as a recommendation problem rather than a single-label classification task. The framework integrates directed graph modeling, graph embedding techniques, and Graph Neural Networks (GCN, GAT, and GraphSAGE) to learn structural dependencies among construction activities and recommend the most probable successor activities. A step-by-step demonstration using a benchmark 7-activity project illustrates graph construction, node feature representation, embedding learning, successor prediction, and Critical Path Method (CPM)-based project duration and cost evaluation, demonstrating the potential of graph learning for intelligent construction scheduling.

BACKGROUND: CONSTRUCTION SCHEDULING AND GRAPH THEORY

Construction Scheduling Fundamentals

Construction scheduling is the process of defining the sequence, duration, and resource allocation for all activities required to complete a project (PMI, 2021). The most widely used technique is the Critical Path Method (CPM), which models the project as a network of activities with deterministic durations and precedence relationships (PMI, 2021). The longest path through the network, the critical path, determines the minimum project duration. Program Evaluation and Review Technique (PERT) extends CPM by incorporating uncertainty using three duration estimates (optimistic, most likely, pessimistic). Activity networks are typically represented using Activity on Node (AON) diagrams, where nodes represent activities and arrows denote precedence (Feng et al. 1997; PMI, 2021). The most common precedence relationship is Finish to Start (FS), but others (Start to Start, Finish to Finish, Start to Finish) can also be represented. Despite their widespread use, traditional methods are labour-intensive, project-specific, and unable to learn from past projects (Yao et al., 2024; Al-Sinan et al., 2024). They also assume unlimited resources, which rarely holds in practice (Kerzner, 2022).

Recommendation-Based Graph Learning Framework

This chapter presents a recommendation-based graph learning framework for automating construction activity sequencing. Traditional construction scheduling relies heavily on planners manually defining precedence relationships between activities based on their knowledge and experience. Although effective for experienced practitioners, this process is time-consuming, subjective, and difficult to standardize across different projects and organizations (Yao et al., 2024; Le and Jeong, 2020). The suggested framework addresses these limitations by learning activity dependencies directly from historical construction schedules. Instead of manually specifying which activity should follow another, the framework predicts the most probable successor activities using recommendation algorithms and graph learning techniques, thereby enabling semi-automatic or fully automatic schedule generation.

The framework begins with data collection and preprocessing, where historical construction schedules from completed projects are collected and standardized. Each schedule consists of construction activities and their corresponding precedence relationships. Before model development, the schedules are cleaned, normalized, and encoded to ensure consistent activity naming and representation across projects. This preprocessing stage improves data quality and enables the learning algorithms to identify meaningful scheduling patterns rather than inconsistencies caused by heterogeneous data sources (Al-Sinan et al., 2024; Amer et al., 2023). Each construction schedule is subsequently represented as a Directed Acyclic Graph (DAG), where nodes correspond to construction activities and directed edges represent finish-to-start precedence relationships. Since construction schedules generally do not contain cyclic dependencies, DAGs provide a natural mathematical representation of project workflows and have been widely adopted for project scheduling and network analysis (PMI, 2021; Cormen et al., 2009). The graph is further represented using an adjacency matrix, allowing graph learning algorithms to efficiently model the structural dependencies among project activities.

The activity sequencing problem is then reformulated as a recommendation problem. Similar to recommender systems used in e-commerce and multimedia applications, the objective is to recommend the most appropriate successor activities based on historical scheduling patterns rather than predicting a single deterministic outcome (Ricci et al., 2015). Given the current activity, the framework produces a ranked list of feasible successor activities together with confidence scores, providing planners with multiple scheduling alternatives that can accommodate variations in site conditions, resource availability, and managerial preferences. To learn these activity relationships, the framework first investigates Association Rule Mining (ARM), which discovers frequently occurring precedence patterns from historical schedules. ARM extracts rules such as Foundation Concrete → Columns and evaluates their reliability using statistical measures including support, confidence, and lift (Agrawal et al., 1993; Agrawal and Srikant, 1994). Although ARM provides interpretable recommendations, it primarily captures local co-occurrence relationships and is less effective at modeling complex structural dependencies within large construction networks. To overcome these limitations, the framework incorporates graph embedding techniques, namely DeepWalk (Perozzi et al., 2014) and node2vec (Grover and Leskovec, 2016). DeepWalk generates multiple random walks over the activity graph and applies the Skip-Gram model to learn low-dimensional node embeddings that preserve graph topology. Node2vec extends DeepWalk by introducing biased random walks controlled by the return parameter (p) and the in-out parameter (q), enabling the model to capture both local neighborhood information and global structural relationships (Grover and Leskovec, 2016). These embedding techniques transform graph nodes into informative vector representations that can be directly utilized by downstream machine learning models. The framework further investigates three representative Graph Neural Network (GNN) architectures: Graph Convolutional Networks (GCN) (Kipf and Welling, 2017), Graph Attention Networks (GAT) (Veličković et al., 2018), and GraphSAGE (Hamilton et al., 2017). GCN aggregates information from neighboring activities through graph convolution operations to learn structural representations of project activities. GAT extends this concept by incorporating an attention mechanism that automatically assigns different importance weights to neighboring activities, enabling the network to focus on the most influential precedence relationships. GraphSAGE introduces neighborhood sampling and aggregation strategies that significantly improve computational scalability while preserving local graph structure, making it suitable for large construction project networks.

THEORETICAL FOUNDATIONS

To construct an AI-driven scheduling recommendation engine, it is necessary to integrate concepts from graph theory, network embeddings, and recommendation system architectures. This section establishes the theoretical foundations underpinning the utilized framework.

Graph Representation of Construction Schedules

A project activity network is represented as a directed graph G = (V, E), where $V = \{v_1, v_2, \ldots\ldots v_n\}$ denotes the set of project activities (nodes) and $E \subseteq V \times V$ denotes the set of directed precedence relationships (edges) between activities. A directed edge $(vi,vj) \in E$ indicates that activity v_i must be completed before activity v_j can begin. This graph representation provides the structural basis for the subsequent graph learning models. The edge set E is a subset of all possible ordered pairs of vertices in V.

The structural topology of ***G*** is mathematically encoded via an adjacency matrix $A \in R^{n \times n}$, where the expression

$$A_{ij} = \begin{Bmatrix} 1, & if\ (v_{i,} v_j) \in E\ , \\ 0, & otherwise \end{Bmatrix} \quad (1)$$

defines the adjacency matrix of a graph.

Where A_{ij} is the element in the ***i***-th row and ***j***-th column of the adjacency matrix A.

• $(v_{i,}v_j)$ denotes a possible edge between vertices v_i and v_j.

• E is the set of all edges in the graph.

Hence,

• If there is an edge connecting v_i and v_j, then

$$A_{ij} = 1$$

• If there is no edge between them, then

$$A_{ij} = 0$$

The adjacency matrix records whether two vertices are directly connected. A value of 1 indicates a connection, while a value of 0 indicates no connection. Hence, in Graph Machine Learning, the adjacency matrix is the fundamental representation of a graph. It encodes the graph's connectivity and serves as the primary input for graph embedding methods and Graph Neural Networks (GNNs), enabling them to learn structural relationships among nodes.

Graph Embedding Techniques

Graph embedding is a technique that transforms a graph into a low-dimensional vector space while preserving the graph's structural information. Instead of representing each construction activity solely by its individual attributes (such as duration, cost, or trade type), graph embedding also captures the sequential and dependency relationships among activities across historical project schedules.

Step 1. Construct the Similarity Graph

Each construction activity is represented as a node (V), while precedence relationships are represented as directed edges (E). The graph is represented as

$$G = (V, E) \tag{2}$$

Step 2. Create the Adjacency Matrix

The graph is converted into an adjacency matrix using Equation (1).

The adjacency matrix records whether two nodes are directly connected and serves as the primary input for graph embedding algorithms.

Step 3. Generate Random Walks

A random walker begins at a given node and iteratively moves to one of its neighboring nodes according to predefined transition probabilities. These random walks capture both local neighborhood information and global structural relationships within the graph.

$$P_{(v_{t+1} = v_j \mid v_t = v_j)} = \begin{Bmatrix} \frac{1}{deg^{+}(v_i)}, & if\ (v_{i,}v_j) \in\ E\ , \\ 0, & otherwise \end{Bmatrix} \tag{3}$$

Step 4. Learn Node Embeddings

The sequences generated by the random walks are treated as sentences, where each node corresponds to a word. Algorithms such as DeepWalk or Node2Vec use the Skip-Gram (Word2Vec) model to learn a low-dimensional embedding for each node. The embedding function is

$$f: V \to R^d$$

where

$$d \ll |V|$$

meaning that each node is represented by a compact vector of dimension d, which is much smaller than the total number of nodes.

Step 5. Form the Embedding Matrix

The learned node embeddings form the matrix

$$Z \in R^{|V| \times d},$$

where each row represents the embedding vector of one construction activity.

Step 6. Integrate with Machine Learning

The graph embedding features are concatenated with the original construction scheduling variables to form an enhanced feature set,

$$X_{final} = [X_{construction}, Z_{embedding}]$$

which is then used as node features for graph neural networks or recommendation models.

GRAPH NEURAL NETWORKS (GNNS)

GNNs directly ingest graph topologies and node features, executing localized convolutions or aggregations to update node states. GCN, GAT, and GraphSAGE were selected because they represent three widely adopted graph learning paradigms with complementary neighborhood aggregation mechanisms, enabling a comprehensive evaluation of recommendation performance.

Graph Convolutional Networks (GCN)

GCNs extend the convolution operation to graph-structured data by aggregating information from neighboring nodes. The layer-wise propagation rule is expressed as:

$$\mathbf{H}^{(l+1)} = \sigma\left(\mathbf{D}^{\sim -\frac{1}{2}}\mathbf{A}^{\sim}\mathbf{D}^{\sim -\frac{1}{2}}\mathbf{H}^{(l)}\mathbf{W}^{(l)}\right) \tag{4}$$

where $\mathbf{A}^{\sim}=\mathbf{A}+\mathbf{I}_n$ denotes the adjacency matrix with self-loops, $\mathbf{D}^{\sim}$is the corresponding diagonal degree matrix with entries $\mathbf{D}_{\tilde{ii}} = \sum_j A_{\tilde{ij}}$, $\mathbf{W}^{(l)}$ is the trainable weight matrix at layer l, $\sigma(\cdot)$ represents a nonlinear activation function (e.g., ReLU), and $\mathbf{H}^{(l)}$ is the node feature matrix. The normalization term ensures numerical stability and prevents features from high-degree nodes from dominating the aggregation process. Consequently, each node learns an updated representation by combining its own features with those of its neighboring nodes.

Graph Attention Networks (GAT)

GATs improve upon GCNs by assigning different importance weights to neighboring nodes through a self-attention mechanism. Instead of treating all neighbors equally, GAT learns adaptive attention coefficients that quantify the contribution of each neighboring node. The attention coefficient between node $\boldsymbol{i}$ and node $\boldsymbol{j}$ is computed as:

$$a_{ij} = \frac{\exp(LeakyReLU(a^{\mathrm{T}}[W\boldsymbol{h}_i \,||W\mathbf{h}_j\,]))}{\sum_{k\in N_i}\exp(LeakyReLU(a^{\mathrm{T}}[W\mathbf{h}_i\,\,||W\mathbf{h}_k\,]))} \tag{5}$$

- a_{ij} is the normalized attention coefficient between nodes i and j;
- a is the learnable attention weight vector;
- W is the shared trainable weight matrix;
- $\mathbf{h}_i$ and $\mathbf{h}_j$ are the feature vectors of nodes i and j, respectively;
- $[\cdot \parallel \cdot]$denotes vector concatenation;
- Ni represents the neighborhood of node i;
- LeakyReLU is the activation function applied before normalization.

The updated node representation is obtained as

$$\mathbf{h}_i^{(l+1)} = \sigma\left(\sum_{j\in \boldsymbol{N}_i} a_{ij}\mathbf{W}_{hj}^{(l)}\right) \tag{6}$$

By assigning larger attention weights to more informative neighbors, GAT captures heterogeneous relationships within the graph and often achieves superior representation learning compared with uniform aggregation methods.

GraphSAGE

GraphSAGE (Sample and Aggregate) is designed to improve scalability for large graphs by sampling a fixed-size neighborhood rather than aggregating information from all adjacent nodes. This sampling strategy significantly reduces computational complexity while preserving local structural information. The neighborhood aggregation is defined as

$$\mathbf{h}_{N_i}^{(l+1)} = \mathrm{AGGREGATE}^{(l)}\left(\left\{\mathbf{h}_j^{(l)} : j \in N_i\right\}\right) \tag{7}$$

In here, l denotes the layer index, while AGGREGATE$^{(l)}$ represents the neighborhood aggregation function, followed by the node update

$$\mathbf{h}_i^{(l+1)} = \sigma\left(\mathbf{W}^l\left[\mathbf{h}_i^{(l)} \,||\, \mathbf{h}_{N_i}^{(l+1)}\right]\right). \tag{8}$$

The aggregation function can be implemented using operations such as mean aggregation, max pooling, or LSTM-based aggregation. By learning from a sampled neighborhood, GraphSAGE efficiently generates inductive node embeddings that generalize well to unseen nodes and large-scale graphs. Table 1 shows the comparison of the GNN models.

Table1: Comparison of GNN Models

Model	Aggregation Strategy	Main Advantage	Limitation
GCN	Uniform aggregation from all neighboring nodes	Simple, computationally efficient, and effective for many graph learning tasks	Assumes all neighbors contribute equally
GAT	Attention-weighted aggregation	Learns the relative importance of neighboring nodes, producing more expressive representations	Higher computational cost due to the attention mechanism
GraphSAGE	Sample-and-aggregate	Highly scalable and supports inductive learning on large graphs	Performance depends on the neighborhood sampling strategy

Figure 1 illustrates the overall workflow of the utilized recommendation-based construction scheduling framework, which integrates graph representation learning and GNNs to recommend successor activities and automatically generate feasible construction schedules. The framework consists of five sequential stages: (1) data preparation, (2) graph construction, (3) model training, (4) successor recommendation, and (5) schedule generation. The first stage, Data Preparation, involves collecting and preprocessing historical construction scheduling data. Each project activity is assigned a unique identifier and standardized description, while precedence relationships are extracted from historical schedules. Data cleaning and preprocessing are then performed to remove inconsistencies and organize the activity information into a structured format suitable for graph-based learning. In the second stage, Graph Construction, the construction project is represented as a Directed Acyclic Graph (DAG). Each activity is modeled as a node, whereas each precedence constraint is represented as a directed edge connecting predecessor and successor activities. The resulting graph is further transformed into an adjacency matrix that mathematically describes the connectivity among activities. This graph representation preserves the logical sequencing of construction operations and serves as the primary input for the learning models. The third stage, model training and successor prediction, employs a Graph Attention Network (GAT) to learn informative representations of construction activities from the project graph. By assigning adaptive attention weights to neighboring activities, the GAT captures both local precedence relationships and the overall project structure. These learned node embeddings provide a rich representation of activity dependencies and are subsequently used to predict the most appropriate successor activities for a given construction task. During the fourth stage, Successor Recommendation, the trained model receives the current activity as input and estimates the likelihood of all feasible successor activities. The predicted successors are ranked according to their recommendation scores, producing a Top-K recommendation list together with confidence values. This ranking assists planners in identifying the most suitable activities to execute next while maintaining logical project sequencing. Finally, in the Schedule Generation stage, the recommended successor activities are assembled into a complete construction schedule while satisfying all precedence constraints. The generated schedule can subsequently be reviewed by project planners and refined by considering additional practical constraints such as resource availability, project duration, equipment allocation, and managerial preferences. This final stage transforms the activity recommendations into an executable project schedule that supports practical construction planning.

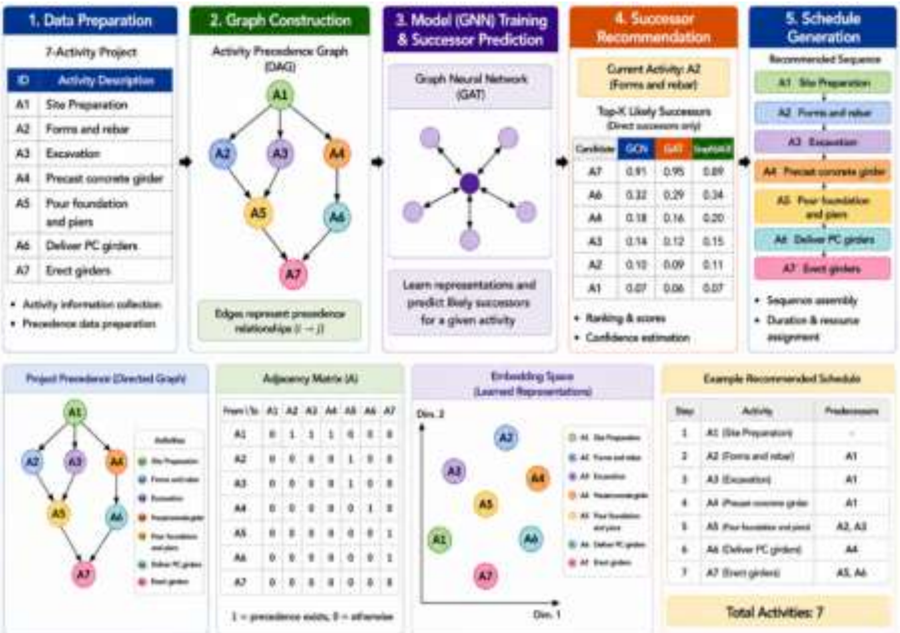

Figure 1: Overall Framework of Recommendation-Based construction scheduling framework

ILLUSTRATIVE EXAMPLE: 7-ACTIVITY CONSTRUCTION PROJECT

The network, presented by Feng et al. (1997) and depicted in Figure 2, consists of 7 activities with a logical relationship of finish-to-start (FS), providing 3 to 5 possible options. Table 2 displays the potential activity options, along with their corresponding durations and costs. The complexity of the problem leads to [3^5 x 4^1 x 5^1] = 4860 possible solutions, with a daily indirect cost of $1500.

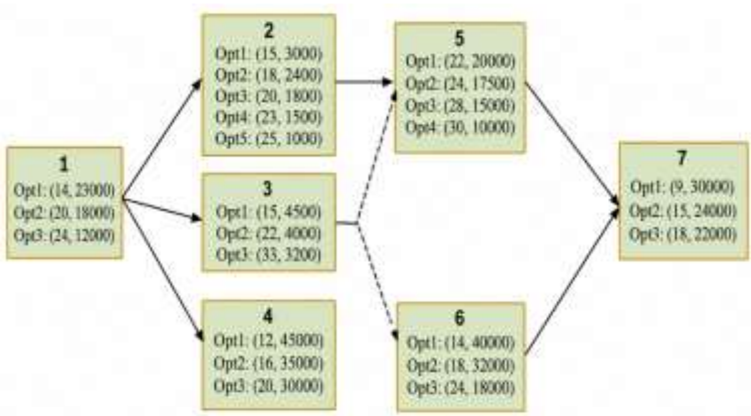

Figure 2: Network configuration of 7-activity test example

Table 2: Options for 7- activity project

Activity Description	Activity number	Precedent activity	Option / Mode	Duration (days)	Direct cost ($)
Site Preparation	A_1	-	1 2 3	14 20 24	23000 18000 12000
Forms and rebar	A_2	1	1 2 3 4 5	15 18 20 23 25	3000 2400 1800 1500 1000
Excavation	A_3	1	1 2 3	15 22 33	4500 4000 3200
Precast concrete girder	A_4	1	1 2 3	12 16 20	45000 35000 30000
Pour foundation and piers	A_5	2,3	1 2 3 4	22 24 28 30	20000 17500 15000 10000
Deliver PC girders	A_6	4	1 2 3	14 18 24	40000 32000 18000
Erect girders	A_7	5,6	1 2 3	9 15 18	30000 24000 22000

For the case example, any design variable (activity) in a solution shows the related activity execution option. For example, for the first solution the initial population is X=[1 2 2 3 2 3 1]. The first design variable value is 1, and it refers to the 1st option of the first activity. From Figure 2, it can be inferred that the randomly selected execution option offers resource utilization as 14 days, and $23,000. Following the same way, options values are assigned to other design variables, and then the CPM is implemented to detect the project duration as 69 days, and $228,400.

Graph Construction and Representation

The 7-activity project is modeled as a Directed Acyclic Graph (DAG) with the following precedence relationships. The graph, shown in Figure 3, contains 7 nodes and 8 directed edges, representing a typical construction workflow from site preparation to girder erection. Figure 3 presents the directed graph representation of the 7-activity construction project.

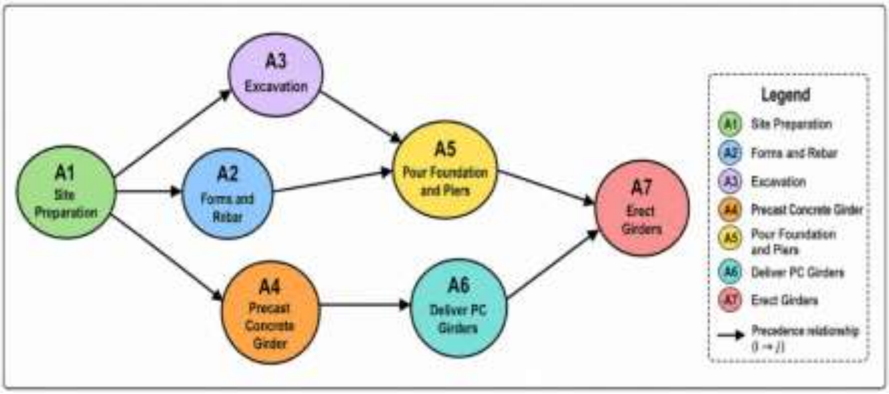

Figure 3: Directed graph of 7-activity construction project

Figure 4 presents the adjacency matrix representation of the directed acyclic graph (DAG) corresponding to the seven-activity construction project. In this matrix, each row represents a predecessor activity, while each column represents a potential successor activity. A value of 1 indicates that a direct precedence relationship exists from the activity in the row to the activity in the column, whereas a value of 0 indicates that no direct dependency exists. This binary representation provides a compact and mathematically convenient description of the project network for graph-based analysis. The matrix captures the logical workflow of the project. Activity A_1 is the initial activity and directly precedes A_2, A_3, and A_4, as indicated by the three entries with a value of 1 in the first row. Activities A_2 and A_3 both precede A_5, representing the convergence of two parallel branches. Similarly, A_4 directly precedes A_6, while both A_5 and A_6 lead to the final activity A_7. The last row contains only zeros because A_7 is the terminal activity and has no successors. Representing the project as an adjacency matrix offers several advantages for graph-based machine learning. Unlike graphical network diagrams, the matrix can be directly processed by graph embedding algorithms such as DeepWalk and node2vec, as well as Graph Neural Networks (GCN, GAT, and GraphSAGE). The adjacency matrix serves as the primary structural input, enabling these models to learn connectivity patterns, capture activity dependencies, and predict the most probable successor activities. Consequently, it forms the foundation of the utilized recommendation-based framework for automated construction schedule generation.

Pred.	A1	A2	A3	A4	A5	A6	A7	Succ.
A1	0	1	1	1	0	0	0	
A2	0	0	0	0	1	0	0	
A3	0	0	0	0	1	0	0	
A4	0	0	0	0	0	1	0	
A5	0	0	0	0	0	0	1	
A6	0	0	0	0	0	0	1	
A7	0	0	0	0	0	0	0	

Note: 1 = direct precedence (row precedes column), 0 = no direct precedence.

Figure 4: Adjacency matrix of 7-activity project

This section presents the implementation of Graph Convolutional Networks (GCN), Graph Attention Networks (GAT), and GraphSAGE to illustrate their applicability.

Application of GNNs to the 7-Activity Project Network

To demonstrate the capability of GNNs in learning structural dependencies within construction schedules, three representative architectures, namely GCN, GAT, and GraphSAGE, are applied to the benchmark 7 activity project. In this framework, each project activity is represented as a node, while the precedence relationships between activities form the directed edges of the graph. The objective is to learn informative node embeddings that capture both the engineering characteristics of each activity and the topological structure of the project network.

Graph Representation

The project network is modeled as a directed graph

$$G = (V, E)$$

where

$$V = \{A_1, A_2, A_3, A_4, A_5, A_6, A_7\}$$

denotes the set of project activities and

$$E = \{A_1, A_2), (A_1, A_3), (A_1, A_4), (A_2, A_5), (A_3, A_5), (A_4, A_6), (A_5, A_7), (A_6, A_7)\}$$

represents the precedence constraints. The corresponding adjacency matrix is

$$A = [0, 1, 1, 1, 0, 0, 0]$$

$$
\begin{matrix}
[0, 0, 0, 0, 1, 0, 0] \\
[0, 0, 0, 0, 1, 0, 0] \\
[0, 0, 0, 0, 0, 1, 0] \\
[0, 0, 0, 0, 0, 0, 1] \\
[0, 0, 0, 0, 0, 0, 1] \\
[0, 0, 0, 0, 0, 0, 0]
\end{matrix}
$$

This matrix completely describes the project topology and serves as the graph input to the GNN models.

Node Feature Matrix

Each activity is characterized by engineering attributes extracted from Table 2. For demonstration purposes, three features are assigned to every node:

- Activity duration
- Direct construction cost
- Number of available execution options

The initial node feature matrix $H^{(0)}$ in Table 3 is constructed using one selected execution option for each activity to demonstrate the graph representation and GNN computation process. These selected options are not intended to represent optimal choices. In practice, the initial node features may also be derived from average values across all execution options, the most representative option, or multiple feature sets corresponding to different execution scenarios.

Table 3: Initial node feature matrix $H^{(0)}$

Activity	**Duration (days)**	**Direct Cost ($)**	**Execution Options**
A_1	14	23,000	3
A_2	18	2,400	5
A_3	22	4,000	3
A_4	20	30,000	3
A_5	24	17,500	4
A_6	24	18,000	3
A_7	9	30,000	3

Graph Convolutional Network (GCN)

GCN updates the representation of each activity by aggregating information from its neighboring activities and itself. The propagation rule is Example: Activity A_5 is directly connected to

- predecessor A_2,
- predecessor A_3,
- successor A_7.

After introducing self-loops, the updated embedding of Activity A_5 is computed by aggregating information from

$$\{A_2, A_3, A_5, A_7\}$$

Consequently,

$$h_5^{(1)} = f(h_2, h_3, h_5, h_7).$$

Thus, the learned representation of Activity A_5 contains not only its own engineering properties but also information propagated from adjacent activities.

Graph Attention Network (GAT)

Unlike GCN, the GAT adaptively assigns different importance to neighboring activities through an attention mechanism. The attention coefficient between activity ***i*** and activity ***j*** is calculated using Equation (5). As an illustrative example, the learned attention coefficients associated with Activity A_5 are presented in Table 4.

It is worth to mention that the numerical values presented in the following tables are illustrative examples intended to demonstrate the computational workflow of the proposed framework and should not be interpreted as results obtained from training on a large historical dataset

Table 4. Learned attention coefficients associated with Activity A_5

Neighbour	**Attention**
A_2	0.42
A_3	0.28
A_7	0.18
Self	0.12

The updated node embedding becomes

$$h_5^{(1)} = 0.42\mathbf{h}_2 + 0.28\mathbf{h}_3 + 0.18\mathbf{h}_7 + 0.12\mathbf{h}_5.$$

This indicates that the model automatically identifies Activity A2 as having the greatest influence on Activity A_5.

GraphSAGE

GraphSAGE improves scalability by sampling only a subset of neighboring activities.

For the present 7-node network, all neighboring activities can be aggregated directly. However, in large-scale construction projects involving hundreds or thousands of activities, GraphSAGE randomly samples only a fixed number of neighbors, significantly reducing computational cost while preserving local structural information.

Learned Node Embeddings

After two graph neural network layers, every activity is represented by a low-dimensional embedding vector,

$$Z = [\, z_1, z_2, \ldots, z_7]^T \quad (9)$$

An illustrative embedding matrix is given in Table 5.

Table 5. Illustrative embedding matrix for 7-activity project

Activity	Embedding (example)
A_1	[0.31, 0.62, 0.48, …]
A_2	[0.42, 0.54, 0.36, …]
A_3	[0.44, 0.51, 0.34, …]
A_4	[0.39, 0.68, 0.29, …]
A_5	[0.73, 0.81, 0.45, …]
A_6	[0.61, 0.66, 0.38, …]
A_7	[0.90, 0.75, 0.22, …]

These embeddings jointly encode the activity attributes and the structural relationships within the project network.

Successor recommendation using node embeddings

It should be noted that the present study employs a single synthetic project network to demonstrate the feasibility of the utilized framework. The model is trained and evaluated on the same project instance; therefore, the results should be interpreted as a proof-of-concept verification rather than evidence of predictive generalization. Consequently, the reported values in Table 6 represent cosine similarity scores between the embedding of Activity A5 and those of the candidate successor activities. These scores indicate the relative strength of the learned relationships and should not be interpreted as probabilities; therefore, they are not expected to sum to one. A comprehensive assessment of generalization would require multiple independent project datasets with appropriate training, validation, and testing splits or cross-validation, which is left for future research. GNN architectures for Activity A_5. All models assign the highest probability to Activity A_7, correctly identifying it as the most likely successor in the project network.

Table 6 presents the cosine similarity scores between the embedding vector of Activity A5 and those of its candidate successor activities obtained using the utilized graph learning models. Cosine similarity measures the degree of similarity between two embedding vectors, where higher values indicate stronger structural and semantic relationships learned from the project graph. As expected, all models assign the highest similarity score to Activity A7, correctly identifying it as the true successor of Activity A5 in the project network. Among the graph embedding techniques, node2vec achieves the highest similarity score (0.93), outperforming DeepWalk (0.88) due to its biased random-walk strategy, which effectively captures both local neighborhood information and broader structural patterns within the graph.

Among the graph neural network models, (GAT) provides the highest similarity score (0.95), followed by GCN (0.91). The superior performance of GAT can be attributed to its attention mechanism, which adaptively assigns higher importance to the most relevant neighboring activities during representation learning. In contrast, candidate activities A6 and A4 receive substantially lower similarity scores across all models, indicating weaker structural relationships with Activity A5 and confirming that they are less appropriate successor recommendations. Overall, these results demonstrate that both graph embedding techniques and graph neural networks successfully capture the precedence structure of the project network, while GAT produces the most discriminative node representations for successor recommendation in this illustrative example.

Table 6: Cosine similarity scores between Activity A5 and candidate successor activities obtained using utilized models.

Candidate Successor	**DeepWalk**	**node2vec**	**GCN**	**GAT**
A7	**0.88**	**0.93**	**0.91**	**0.95**
A6	0.35	0.31	0.32	0.29
A4	0.22	0.19	0.18	0.16

For all three GNN models, Activity A7 receives the highest prediction score and is therefore correctly identified as the immediate successor of Activity A_5. Among GNNs, GAT performed best.

PROJECT DURATION AND COST EVALUATION BASED ON GNN RECOMMENDATIONS

After GCN, GAT, and GraphSAGE are trained on the 7-activity project network, the learned node embeddings are used to predict successor activities. The recommended precedence structure is then evaluated using the CPM to obtain the project duration and cost corresponding to a specific activity-option vector. This process demonstrates how the learned graph representations can be directly utilized to generate feasible schedules that feed the multi-objective optimization module.

1) Project Network and GNN Predictions

The project network (Figure 2) contains 7 activities with the following precedence relationships:

$$A_1 \rightarrow A_2,\ A_1 \rightarrow A_3,\ A_1 \rightarrow A_4,$$
$$A_2 \rightarrow A_5,\ A_3 \rightarrow A_5,\ A_4 \rightarrow A_6,$$
$$A_5 \rightarrow A_7,\ A_6 \rightarrow A_7.$$

All three GNN models (GCN, GAT, and GraphSAGE) correctly identify the ground-truth successors for each activity. For example, after Activity A1 is instantiated, Activities A2, A3, and A4 are identified as its immediate successor activities according to the project precedence relationships. Similarly, after Activity A2 is instantiated, Activity A5 is correctly recommended as its successor. These results demonstrate that the utilized GNN models successfully learn the underlying precedence structure of the construction project. Table 7 depicts the Top-1 and Top-2 successor prediction performance comparison of the ML techniques.

Table 7: Top-1 and Top-2 predicted successor activities for each project activity using GCN, GAT, and GraphSAGE

Activity	**Successors**	**GCN Top-1**	**GCN Top-2**	**GAT Top-1**	**GAT Top-2**	**GraphSAGE Top-1**
A_1	A_2, A_3, A_4	A_2	A_2, A_3	A_2	A_2, A_3	A_2
A_2	A_5	A_5	A_5	A_5	A_5	A_5
A_3	A_5	A_5	A_5	A_5	A_5	A_5
A_4	A_6	A_6	A_6	A_6	A_6	A_6
A_5	A_7	A_7	A_7	A_7	A_7	A_7
A_6	A_7	A_7	A_7	A_7	A_7	A_7
A_7	-	-	-	-	-	-

2) Learned Node Embeddings

After two graph convolution layers, each activity is represented by an embedding vector of dimension d = 8. Example embeddings are listed below. Table 8 represents the example node embeddings for the ML techniques.

Table 8: Example node embeddings

Activity	**GCN Embedding**	**GAT Embedding**	**GraphSAGE Embedding**
A_1	[0.32,0.45,0.81,0.12,0.33,0.22,0.41,0.19]	[0.35,0.47,0.79,0.15,0.31,0.24,0.42,0.21]	[0.30,0.43,0.80,0.10,0.34,0.20,0.40,0.18]
A_2	[0.41,0.22,0.65,0.33,0.28,0.17,0.36,0.14]	[0.46,0.25,0.68,0.31,0.30,0.19,0.37,0.16]	[0.40,0.20,0.63,0.28,0.26,0.16,0.33,0.13]
A_3	[0.44,0.20,0.63,0.27,0.32,0.16,0.35,0.15]	[0.49,0.23,0.66,0.27,0.34,0.17,0.36,0.16]	[0.43,0.21,0.62,0.23,0.30,0.15,0.32,0.14]
A_4	[0.28,0.59,0.71,0.21,0.27,0.31,0.30,0.18]	[0.29,0.61,0.74,0.20,0.28,0.32,0.31,0.19]	[0.27,0.58,0.69,0.18,0.26,0.29,0.28,0.17]
A_5	[0.73,0.81,0.45,0.39,0.46,0.35,0.48,0.27]	[0.78,0.83,0.49,0.41,0.47,0.36,0.51,0.28]	[0.70,0.79,0.42,0.36,0.43,0.33,0.45,0.25]
A_6	[0.62,0.54,0.34,0.40,0.41,0.29,0.37,0.22]	[0.64,0.56,0.37,0.42,0.42,0.30,0.38,0.23	[0.60,0.52,0.33,0.37,0.38,0.27,0.35,0.21]
A_7	[0.91,0.74,0.25,0.48,0.56,0.33,0.40,0.24]	[0.93,0.76,0.27,0.50,0.57,0.34,0.42,0.25]	[0.89,0.72,0.24,0.46,0.54,0.31,0.38,0.22]

3) Selected Activity-Option Vector

The schedule selected for CPM evaluation is

$$\mathbf{X} = [1, 2, 2, 3, 2, 3, 1]$$

Moreover, Table 9 indicates the selected durations and direct costs.

Table 9: Selected durations and direct costs

Activity	Description	Option	Duration (days)	Direct Cost ($)
A_1	Site Preparation	1	14	23,000
A_2	Forms and Rebar	2	18	2,400
A_3	Excavation	2	22	4,000
A_4	Precast Concrete Girder	3	20	30,000
A_5	Foundation and Piers	2	24	17,500
A_6	Deliver PC Girders	3	24	18,000
A_7	Erect Girders	1	9	30,000

5) Critical Path Analysis (CPM)

Three feasible execution paths are obtained:

Path 1

$$A_1 \rightarrow A_2 \rightarrow A_5 \rightarrow A_7$$
$$T_1 = 14 + 18 + 24 + 9 = 65 \text{ days}$$

Path 2

$$A_1 \rightarrow A_3 \rightarrow A_5 \rightarrow A_7$$
$$T_2 = 14 + 22 + 24 + 9 = 69 \text{ days}$$

Path 3

$$A_1 \rightarrow A_4 \rightarrow A_6 \rightarrow A_7$$
$$T_3 = 14 + 20 + 24 + 9 = 67 \text{ days}$$

Therefore,

$$T_{project} = \max(T_1, T_2, T_3) = 69 \text{ days}$$

The critical path is

$$A_1 \rightarrow A_3 \rightarrow A_5 \rightarrow A_7$$

6) Project Cost Calculation

The total direct cost is

$$C_{direct} = 23000 + 2400 + 4000 + 30000 + 17500 + 18000 + 30000 = \$124{,}900.$$

An indirect cost of $1500/day,

$$C_{indirect} = 69 \times 1500 = \$103{,}500.$$

Hence,

$$C_{total} = C_{direct} + C_{indirect} = 124{,}900 + 103{,}500 = \$228{,}400.$$

Table 10 illustrates the summary of schedule evaluation for the 7-activity implemented problem. It should be mentioned that a specific activity-option vector X = [1, 2, 2, 3, 2, 3, 1] was selected from the solution space. This particular combination was chosen because it represents a typical construction sequence with realistic durations and costs. In practice, the framework would learn to recommend such combinations from historical data rather than requiring manual selection. The following CPM analysis illustrates how the framework's recommendations can be evaluated in terms of project duration and cost.

Table 10. Summary of schedule evaluation

Metric	Value
Selected activity-option vector	[1, 2, 2, 3, 2, 3, 1]
Critical path	$A_1 \rightarrow A_3 \rightarrow A_5 \rightarrow A_7$
Project duration	69 days
Total direct cost	\$124,900
Total indirect cost	\$103,500
Total project cost	\$228,400

The CPM analysis is performed using the reference precedence network adopted from Feng et al. (1997) to illustrate the scheduling workflow. The graph learning models are evaluated based on their ability to reproduce the existing precedence relationships rather than to generate a new project network. For demonstration purposes, CPM is applied to the reference project network after evaluating the graph learning models. Therefore, the CPM results should be interpreted as an illustrative scheduling example rather than a validation of model-generated precedence relationships.

CONCLUSION

This chapter presented a recommendation-based graph framework for intelligent construction activity sequencing by integrating graph representation learning with Graph Neural Networks (GNNs). Historical construction schedules were represented as directed acyclic graphs (DAGs), where activities were modeled as nodes and precedence relationships as directed edges. The proposed framework comprised five key stages: data preprocessing, graph construction, graph representation learning, successor activity recommendation, and schedule generation, providing a unified decision-support approach for automated construction planning. The methodology was demonstrated using a benchmark seven-activity construction project comprising 7 activities, 8 precedence relationships, and 4,860 feasible activity–option combinations. The project network was represented as both a directed graph and an adjacency matrix, enabling the application of GCN, GAT, and GraphSAGE models. The learned node representations captured both engineering attributes and structural dependencies, facilitating successor activity recommendation. Among the graph learning models, node2vec achieved the highest cosine similarity score (0.93) among the graph embedding techniques, while GAT achieved the highest cosine similarity score (0.95) among the GNN models. The recommended successor relationships were subsequently evaluated using the Critical Path Method (CPM), resulting in a feasible construction schedule with a project duration of 69 days and a total project cost of $228,400. These results demonstrate the feasibility of the proposed framework for graph-based construction schedule generation.

Despite these encouraging results, the present study should be regarded as an illustrative proof of concept rather than a comprehensive validation of the proposed methodology. The framework was demonstrated using a single benchmark project, and the reported cosine similarity scores were intended to illustrate the computational workflow rather than establish predictive generalization. Consequently, the predictive performance and generalizability of the proposed framework remain to be validated using multiple real-world construction projects with independent training, validation, and testing datasets together with appropriate recommendation evaluation metrics. Furthermore, comprehensive quantitative comparisons with additional graph learning and recommendation approaches are required to establish the robustness, scalability, and practical applicability of the proposed methodology.

Future research should focus on extending and validating the proposed framework using large-scale construction projects containing hundreds or thousands of activities. The predictive capability of the framework can be enhanced by incorporating richer node and edge attributes, including resource availability, equipment utilization, workspace constraints, safety indicators, and spatial information obtained from Building Information Modeling (BIM) and Digital Twin technologies. Additional improvements may be achieved through adaptive and online learning, reinforcement learning, explainable artificial intelligence (XAI), hybrid graph learning architectures integrating Graph Neural Networks with Large Language Models (LLMs), and transfer learning using graph foundation models. Furthermore, integrating the recommendation framework with multi-objective optimization algorithms, such as Rao, Jaya, Grey Wolf Optimizer (GWO), and other metaheuristic methods, would enable simultaneous optimization of project duration, cost, quality, safety, sustainability, and resource utilization, ultimately supporting the development of intelligent, fully automated construction scheduling systems for next-generation digital construction and BIM-enabled project management.

REFERENCE

Agrawal, R., Imieliński, T., & Swami, A. (1993). Mining association rules between sets of items in large databases. *Proceedings of the ACM SIGMOD International Conference on Management of Data*, 207–216. https://doi.org/10.1145/170035.170072

Agrawal, R., & Srikant, R. (1994). Fast algorithms for mining association rules. Proceedings of the 20th International Conference on Very Large Data Bases (VLDB), 487–499.

Al-Sinan, M. A., Bubshait, A. A., & Aljaroudi, Z. (2024). Generation of Construction Scheduling through Machine Learning and BIM: A Blueprint. Buildings, 14(4), 934. https://doi.org/10.3390/buildings14040934

Amer, F., Golparvar-Fard, M., & Brilakis, I. (2021). Modeling dynamic construction work template from existing scheduling records via sequential machine learning. Advanced Engineering Informatics, 47, 101236.

Amer, F., Jung, Y., & Golparvar-Fard, M. (2023). Construction schedule augmentation with implicit dependency constraints and automated generation of lookahead plan revisions. Automation in Construction, 156, 104896.

Boje, C., Guerriero, A., Kubicki, S., & Rezgui, Y. (2020). Towards a semantic Construction Digital Twin: Directions for future research. Automation in Construction, 114, 103179.

Cormen, T. H., et al. (2009). Introduction to Algorithms (3rd ed.). MIT Press.

Feng, C.-W., Liu, L., & Burns, S. A. (1997). Using genetic algorithms to solve construction time-cost trade-off problems. Journal of Computing in Civil Engineering, 11(3), 184–189.

Grover, A., & Leskovec, J. (2016). node2vec: Scalable feature learning for networks. Proceedings of the 22nd ACM SIGKDD International Conference on Knowledge Discovery and Data Mining, 855–864.

Hamilton, W. L., Ying, R., & Leskovec, J. (2017). Inductive representation learning on large graphs. Advances in Neural Information Processing Systems (NeurIPS), 30.

Kerzner, H. (2022). Project Management: A Systems Approach to Planning, Scheduling, and Controlling. Wiley.

Kipf, T. N., & Welling, M. (2017). Semi-supervised classification with graph convolutional networks. International Conference on Learning Representations (ICLR).

Le, C., & Jeong, H. D. (2020). Artificial Intelligence Framework for Developing a Critical Path Schedule Using Historical Daily Work Report Data. Construction Research Congress 2020, 575–584. https://doi.org/10.1061/9780784482889.059

Perozzi, B., Al-Rfou, R., & Skiena, S. (2014). DeepWalk: Online learning of social representations. Proceedings of the 20th ACM SIGKDD International Conference on Knowledge Discovery and Data Mining, 701–710.

PMI (Project Management Institute). (2021). A Guide to the Project Management Body of Knowledge (PMBOK® Guide) (7th ed.). Project Management Institute.

Ricci, F., Rokach, L., & Shapira, B. (2015). Recommender Systems Handbook. Springer.

Veličković, P., Cucurull, G., Casanova, A., Romero, A., Liò, P., & Bengio, Y. (2018). Graph attention networks. International Conference on Learning Representations (ICLR).

Wu, Z., Pan, S., Chen, F., Long, G., Zhang, C., & Yu, P. S. (2021). A comprehensive survey on graph neural networks. IEEE Transactions on Neural Networks and Learning Systems, 32(1), 4–24.

Yao, Y., Tam, V. W. Y., Wang, J., Le, K. N., & Butera, A. (2024). Automated construction scheduling using deep reinforcement learning with valid action sampling. Automation in Construction, 166, 105622.

Zhang, W., Wang, Z., Yang, Z., & Cai, Z. (2026). BIM-based construction scheduling optimization through graph neural network-driven spatial semantic reasoning. Journal of Industrial Information Integration, 51, 101088.

Zhou, J., Cui, G., Hu, S., Zhang, Z., Yang, C., Liu, Z., Wang, L., & Sun, M. (2020). Graph Neural Networks: A Review of Methods and Applications. AI Open, 1, 57–81. https://doi.org/10.1016/j.aiopen.2021.01.001

Gabion-Based Structures for Rockfall Protection: Behaviour, Design and Applications

Bayram ATEŞ[1*]

Mehmet Ali KALAYLI[2]

1- Dr.; Karadeniz Technical University, Faculty of Engineering, Department of Civil Engineering, 61030, Trabzon, Türkiye. bayramates61@hotmail.com, ORCID No: 0000-0002-1251-7053 (corresponding author)[*]

2- Dr.; Kırıkkale University, Faculty of Engineering, Department of Civil Engineering, 71000, Kırıkkale, Türkiye. mehalkal777@gmail.com, ORCID No: 0000-0003-2776-4740

ABSTRACT

Owing to its sudden onset, high kinetic energy, and hard-to-predict recurrence, rockfall is among the most common mass movements threatening life and property in mountainous and rugged terrain. This chapter first addresses the definition and mechanism of rockfall and presents documented examples from rural areas, provincial and district centres, engineering structures, and protected heritage sites in the light of the recent literature. Active protection methods (controlled breaking and stacking of hazardous blocks, covering slope faces with steel meshes, and in-place anchoring of large blocks with woven cable nets) and passive methods (flexible barriers, channel/static barriers, reinforced-earth barriers and retaining structures, and passive surface draping with wire mesh) are then introduced, together with current detection approaches based on unmanned aerial vehicle photogrammetry, geophysical surveys and two- and three-dimensional trajectory simulations. As the focus of the study, the geometric and material properties of gabion walls, their static verification as gravity structures, and the theoretical basis of their design under impact are described through the Swiss ASTRA contact-force model, the increase of the compression modulus under successive strikes, and a displacement-based design approach built on a two-degree-of-freedom idealisation. Finally, recent experimental and numerical studies on the impact performance of gabion and gabion-faced barriers are evaluated comparatively, and implications for design practice are drawn. Open research needs, such as the absence of a standard design code, wire corrosion, and long-term durability, are also highlighted.

Keywords – Rockfall, passive protection structures, gabion wall, impact loading, rockfall mitigation, energy dissipation.

INTRODUCTION

In the literature, rockfall is defined as a slope instability that develops when jointed rock blocks in source areas at the upper parts of steep slopes lose their stability and start moving downslope, gaining velocity and energy as they travel (Varnes, 1978; Hutchinson, 1988; Akın et al., 2020). Unlike other mass movements, a rockfall usually affects a narrow corridor; however, because a block that has remained in place for years can be mobilised within seconds once the triggering factors coincide, and because the event develops with very high kinetic energy at unpredictable intervals, there is practically no opportunity for intervention at the moment of failure (Wyllie and Mah, 2004; Akın et al., 2020). The mass of moving blocks may range from a few kilograms to tens of tonnes, and every year such blocks cause traffic interruptions, damage to structures and vehicles, and occasionally loss of life.

Owing to its morphological and climatic characteristics, Türkiye is among the countries where rockfall disasters occur frequently; in terms of the number of events and of people affected, the Eastern Anatolia, Eastern Black Sea and Western Black Sea regions rank first (Gökçe et al., 2008). Rockfall activity is known to increase at high elevations where precipitation is abundant, freeze–thaw cycles are frequent and seismicity is high (Wyllie, 2015). Indeed, after the 6 February 2023 Kahramanmaraş earthquakes, more than five thousand seismically triggered rockfalls and similar coseismic slope failures were documented, demonstrating how widespread the rockfall hazard is in regions of high seismicity (Görüm et al., 2023).

The entire body of engineering work aimed at eliminating the hazard posed by potentially falling rocks is referred to as rockfall mitigation. Mitigation involves quantifying the magnitude of the risk, estimating the damage that falling blocks could cause and developing alternative remedial solutions, and it requires the cooperation of disciplines such as geological, civil, mining and geomatics engineering together with archaeology and urban planning (Nasery and Çelik, 2020; Nasery, 2025). In this chapter, the rockfall phenomenon is treated starting from its mechanism; after examples from different land uses, active and passive mitigation methods and current detection techniques are summarised, the design and performance of gabion walls as a protective measure are examined, as they stand out for their economy and high energy-dissipation capability.

FORMATION OF ROCKFALL AND MOTION BEHAVIOUR

The occurrence of rockfall is generally explained by the combined influence of slope inclination and topography, the discontinuity pattern and strength of the rock mass, and triggering factors such as earthquakes, rainfall, freeze–thaw and human activity. The first factor is the discontinuities that develop in the source rock mass. Discontinuities may form over geological time through weathering and tectonism, or within seconds during an earthquake; the discontinuity network is a 'living' system. The second factor is the inclined surface. As the slope angle increases, the downslope component of the weight vector grows and block motion becomes easier; friction between block and surface, and the morphology, material and cover of the surface, also control the motion (Dorren, 2003; Wyllie, 2015). According to the classical relationship established by Ritchie (1963), the likelihood of motion becomes significant at slope angles of about 30°; blocks tend to roll on slopes of 30°–45°, to roll with bouncing between 45° and 60°, and to fall freely on slopes of 60°–90° (Figure 1). The third factor comprises the triggering forces that initiate motion: removal of the material beneath a block by rainfall, surface runoff or avalanches; ice pressure developing in cracks during freeze–thaw; the thrust of plant roots growing within discontinuities and the leverage exerted by wind through tree trunks; animal activity; lightning strikes; blasting vibrations from mining and construction; and earthquakes (Nasery, 2025).

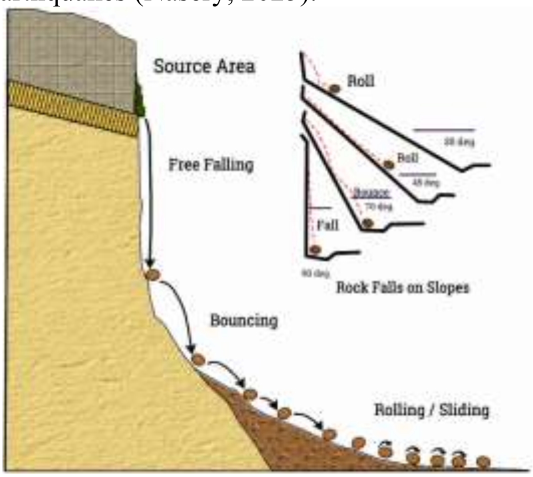

Figure 1: Rockfall motion modes as a function of slope angle
Source: Ritchie (1963)

After detachment, and depending on the topography, a block passes through free-fall, bouncing (rebound), rolling, and sliding phases, individually or in succession, and comes to rest where its energy is exhausted (Dorren, 2003; Volkwein et al., 2011). The main parameters controlling the trajectory are the restitution coefficients of the ground (normal Rn and tangential Rt), the rolling friction coefficient (k), and the mass, shape, and initial conditions of the block. The restitution coefficient is the fundamental parameter defining how much energy a block retains when it rebounds from a surface (Bozzolo and Pamini, 1986), and it can be determined by block-drop tests, back-analysis of the traces of fallen blocks, or coefficient tables in the literature. Block shape also exerts a strong control on trajectory behaviour: spherical blocks have the highest rolling and acceleration potential, massive blocks with rounded edges are easily mobilised on inclined surfaces, sharp-edged and flat blocks predominantly slide, and slab-shaped blocks can only slide (Nasery, 2025). Recording block-shape classes in field inventories is therefore important for constructing realistic scenarios. The total kinetic energy of a moving block is written as the sum of its translational and rotational components:

$$E_k = \frac{1}{2}\, m\, v^2 + \frac{1}{2}\, I\, \omega^2 \tag{1}$$

Here m denotes the block mass, v the translational velocity, I the mass moment of inertia, and ω the angular velocity. The energy, velocity, and bounce-height values used in design are obtained from trajectory analyses. To give an idea of scale, two-dimensional analyses carried out for a 15-tonne design block at 20 critical sections in the Sille Valley indicated that, at the most unfavourable section, a block reaching the road may attain a total kinetic energy of 6000 kJ, a velocity of 27.5 m/s and a bounce height of 25.65 m, whereas at the slope toe where the barrier line was proposed the demand remained below 2805 kJ, 18.4 m/s and 4.03 m, respectively (Nasery, 2025). These magnitudes directly dictate the order of demand for which the protection structure is to be selected and dimensioned.

EXAMPLES OF ROCKFALL IN DIFFERENT LAND USES

Protection and intervention strategies against rockfall vary according to the physical, social, and economic characteristics of the affected area. In this context, rockfall situations are examined separately for rural areas, densely populated provincial and district centres, engineering structures, and protected heritage sites.

In Rural Areas

Rural areas are regions of low population density consisting of agricultural land, pasture and mountainous terrain, and because of their rugged morphology rockfall is quite common there (Baillifard et al., 2004). Events that do not affect human life are generally left without intervention; when settlements or public investments are affected, mitigation decisions are based on cost–benefit analysis. In some cases it is more economical to expropriate and evacuate a settlement of a few dwellings than to remediate tonnes of rock; by contrast, where an immovable common heritage is at stake, as in the case of the Sümela Monastery, costly mitigation investments become unavoidable. An important advantage of rural terrain is that the area can be evacuated when necessary, and thanks to the low building density, rock mitigation, an inherently hazardous operation, can be carried out at lower risk than in city centres or heritage sites (Nasery, 2025).

In Provincial and District Centres

Provincial and district centres in Türkiye have grown considerably, particularly under the influence of rural migration accelerating from the 1950s onwards, and settlement areas have gradually expanded into zones exposed to natural hazards. In this process, the rockfall hazard was not always adequately assessed before development, and in some cases the danger became evident only after the urban fabric had formed. Rockfall not only threatens existing residential areas but can also directly influence the growth directions of cities, transport links and new zoning decisions. For this reason, identifying the rockfall hazard in areas to be opened for settlement in advance, and implementing the necessary protective measures before construction begins, offers a more effective approach both technically and economically. When dwellings, infrastructure systems, public investments and private property values in urbanised areas are considered together, mitigation and protection works against rockfall in most cases emerge as the more rational solution in terms of long-term risk reduction.

Documented urban examples from Türkiye include a hazard assessment based on two-dimensional trajectory analyses and a protective fence proposal for the settlement around Afyonkarahisar Castle (Topal et al., 2007); a study around Ankara Citadel in which ditches and rock bolts were found impractical because of the dense settlement pattern and catch barriers were recommended instead (San et al., 2020); a rockfall risk map of the Kilis city centre produced with geographic information systems and remote sensing (Çelik and Gülersoy, 2017); and a hazard assessment for the steep slopes surrounding the Ermenek (Karaman) district centre (Taga and Zorlu, 2017). In some cases, such as Zonguldak, blocks detaching from slopes directly above houses have been reported to reach dwellings and development areas, even bringing evacuation onto the agenda (Nasery, 2025). In Hemşin (Rize), blocks detaching from a steep rock slope broke through the rear wall of a sports facility at the slope toe and travelled into the building (Figure 2).

Figure 2: The Hemşin (Rize) rockfall case: the source rock slope and the affected sports facility (top), and the blocks that entered the building (bottom)
Source: Muhçu (2024)

In Engineering Structures

Rockfall disasters are frequent along high-budget facilities such as highways, railways, tunnels, and dams, because in these structures, the alignment cannot be relocated according to the risk. Slope cutting for road platforms in mountainous terrain creates new discontinuities along kilometers of alignment, while dams are, for reasons of cost, placed in narrow and steep valleys that exhibit the most rockfall-prone morphologies. Although most events end with material damage, injuries and fatalities are relatively frequent on highway slopes where the natural hillside has been disturbed. Since it is impossible to protect the entire road network of Türkiye, which exceeds 400,000 kilometres, prioritisation is made on the basis of criteria such as traffic volume and block-fall frequency (Nasery, 2025). At dams, falling blocks both accelerate reservoir sedimentation and may damage the embankment, spillway, tunnels, and power structures.

Examples concerning engineering structures in the literature include the determination of the optimum barrier location and height on the Zonguldak–Kilimli highway by trajectory analyses (Keskin et al., 2020); the three-dimensional performance assessment of a roadside rock-catch ditch at Ürgüp–Akköy, where the ditch was found insufficient along certain stretches (Akın et al., 2019); experimental studies of rock sheds, common on Swiss mountain roads, under block impact (Labiouse et al., 1994; Labiouse et al., 1996); and prototype tests on the ultimate impact resistance of prestressed concrete rock sheds (Kishi et al., 2002). Reinforced concrete impact walls used to protect roads and settlements at slope toes in densely built hilly regions such as Hong Kong, together with the gabion cushion layers placed in front of them, are also current applications under this heading (Perera and Lam, 2023).

In Protected Heritage Sites

In heritage sites, the rockfall hazard must be evaluated, unlike for conventional engineering structures, in terms of both life safety and the preservation of cultural assets. Since part of the historical and archaeological areas are located on steep slopes, in rock-hewn spaces, in valleys or in positions integrated with natural rock masses, weathering, crack propagation, earthquake effects and climatic processes can weaken block stability there over time. Increasing visitor numbers today make the consequences of this hazard even more significant. Rockfall measures to be implemented in heritage sites should therefore be planned by jointly considering engineering safety, compatibility with the cultural fabric, visual impact, minimum intervention and long-term monitoring.

Mitigation works in heritage sites involve difficulties of their own. Investigations on inaccessible slopes are carried out by industrial climbers, and the discovery of previously unknown artefacts on slopes that could not be entered before may halt the works. Vibration-generating operations are avoided; where unavoidable, they are performed at low intensities and the structures are continuously monitored. Because destructive methods such as drilling can hardly ever be used owing to the risk of damaging historical remains, geophysical methods come to the fore. In addition, the sites must be closed to visitors for the duration of the works, and the requirement not to disturb the historical silhouette restricts the choice of materials (Nasery et al., 2023; Nasery, 2025). A comparable example at the international scale is the rockfall hazard and risk assessment developed for the cliffs above the historical settlement of Monemvasia in Greece (Saroglou et al., 2012); similar assessments have been made for Kastamonu Castle and for Safranbolu, a UNESCO World Heritage site (Nasery, 2025). These findings show that protection design in heritage sites serves not only life safety but also the continuity of cultural assets.

MITIGATION AND PROTECTION METHODS AGAINST ROCKFALL

The remediation and intervention method to be applied differs according to the risk level at the site, the morphology of the region, the protection status of the area and its intended use. Protective works are basically divided into two groups, active and passive: in active methods the blocks are prevented from moving and are stabilised in place, whereas in passive methods motion is partly or fully allowed and the block is stopped before creating a hazard or is guided to safe areas (Turner and Schuster, 2012; Akın et al., 2020). The same installation may fall into either group depending on how it is anchored. Safety and economy are considered together in method selection, and risk rating systems also define measure groups according to the risk level. The classification developed by Saroglou et al. (2012) for the historical settlement of Monemvasia, which divides slopes into five classes according to a weighted risk score and assigns indicative measure groups to each class, is summarised in Table 1.

Table 1: Slope classification according to rockfall risk and recommended measure groups

Risk Class	Weighted Score (1–100)	Risk	Recommended Protection Measures
I	≤ 20	Very Low	No measures required; occasional spot interventions may be applied.
II	21–40	Low	Measures of limited extent.
III	41–60	Medium	Light measures: bolts, meshes, removal of unstable blocks, simple light fences.
IV	61–80	High	Combined application of active (bolts, anchors) and passive (mesh, cables, buttress walls, fences, block removal) measures.
V	81–100	Very High	Critical stability state; extensive and strong combination of active and passive measures; residual risk is accepted.

Source: Saroglou et al. (2012)

Active Methods: Stabilising the Blocks in Place

Active protection methods are applications that aim to control the rockfall hazard at its source. In these methods, the hazardous blocks are fixed in place, strengthened, or removed in a controlled manner. Active measures offer economical and effective solutions, especially at sites where the number of hazardous blocks is limited and the rockfall source is concentrated at specific locations. The success of the application, however, depends on the correct identification of all potentially loose blocks at the site; even a single overlooked block may allow the hazard to persist. Active systems built with appropriate engineering design and correct material selection can provide long-term safety and can also serve as complementary measures that increase the effectiveness of passive protection structures.

Controlled Breaking and Stacking of Hazardous Blocks

Where the hazardous blocks are below certain volumes or can be reduced to such volumes with safety precautions, one of the most effective mitigation methods is breaking and stacking. Blocks are fragmented with hydraulic breakers or with pyrotechnic cartridges and chemical expanding agents, and are then hauled away or brought down along a controlled path so that the slope is cleared. Breaking is performed in three categories: in fully controlled breaking, the block is wrapped so that it cannot move before fragmentation and the fragments remain within the containment works; in rebound-controlled breaking, the block is not fixed, but its surface is covered with steel mesh or a membrane to prevent fragments from scattering; and in free breaking, the fragments are directed straight to a safe area. Where the lower elevations are unsuitable for clearing, the fragments are stacked on the slope in suitable areas of reduced gradient, if necessary, using mortar. The strongest aspects of the method are that it requires no imported material, that the equipment can be reused, and that the hazardous rock is completely eliminated; the need for temporary protection, transport restrictions, and the requirement for experience are its main limitations. In Türkiye, fully controlled breaking at the Ancient Port of Assos and rebound-controlled breaking applied to hazardous blocks of several thousand tonnes at the Sümela Monastery are documented applications of the method (Nasery et al., 2023; Nasery et al., 2024).

Covering the Slope Face with Steel Meshes

On source rock masses spread over a wide area, slope faces that may become hazardous as discontinuities propagate can be protected by covering them with prefabricated steel meshes, panel meshes, or ring nets. The method is particularly preferred on steep slopes with large elevation differences. Galvanised hexagonal-mesh steel nets with wire diameters of 2–3 mm, or ring nets with ring diameters of 10–50 cm, may be used; the nets can be supplied ready-made or woven on site from cables laid transversely and longitudinally. Three types of anchors operate in the system: crest anchors installed above the slope in zones of few discontinuities, which carry the nets; surface anchors that tie the system to the face and restrain block movement; and toe anchors that allow small material sifting down inside the net to accumulate at the lower elevation. In dimensioning, the cables and surface anchors are verified in tension, and the crest anchors, which act perpendicular to the cable, in shear; snow load must also be taken into account because mesh-covered faces retain snow (Seferoğlu et al., 2016). Anchor depth should be selected to provide effective embedment beyond the depth of the discontinuities. Regular removal of detached material (debris) pressing on the net, which may otherwise cause wire failures through fatigue, is the principal maintenance requirement of the method.

In-Place Anchoring of Large Blocks with Woven Cable Nets

At some sites, fixing large hazardous blocks in place may be a safer solution than removing them. Controlled breaking may create additional risks, especially where a historical structure, a road, a settlement, or a sensitive land use lies immediately below the block. In this case, the volume, weight, and geometry of the block and the strength properties of the rock mass are determined, and a suitable restraint system is designed for actions such as snow, wind, and earthquake. While prefabricated steel meshes may suffice for small and regular blocks, steel cable nets woven in place to fit the rock surface are preferred for large blocks of irregular geometry. Where necessary, wire meshes of smaller aperture are placed inside the system to prevent the fall of small fragments. The cable-and-net assembly is connected to sound bedrock with anchors and bolts, so that the block is held safely in place.

Passive Methods: Stopping and Guiding After Motion

Passive protection systems are applied not to prevent the movement of rock blocks but to reduce potential damage by safely stopping or guiding the blocks once motion has begun. They offer a suitable solution, particularly over large areas, where all potentially hazardous blocks cannot be identified or where intervention at the source zone is technically and economically difficult. These systems can protect a defined downslope region independently of the individual blocks in the source area. To remain functional, however, they must be regularly inspected and maintained: deformations caused by previous rockfalls, material accumulating behind the system or a reduction of the effective protection height may lead to loss of performance in subsequent events. In selecting the appropriate system, the velocity, energy and bounce height that the blocks may attain during motion and their possible travel distance are considered; the energy-dissipation capacity of the structure, its cost, and the space required for its installation are further criteria governing design and siting.

Flexible Barriers with Brake Elements

Flexible (energy-dissipating) barriers are systems composed of steel posts, special steel nets stretched between the posts, and brake elements that dissipate the impact energy by elongating; they are used to stop accelerated blocks without harming the surroundings. Manufactured with certified capacities ranging from 100 kJ up to 10,000 kJ, these systems offer the flexibility of being installed at almost any position on a slope; in Europe, their design and testing principles have been standardized by the ETAG 027 guideline (EOTA, 2008). The deformation of the system during impact reduces the damage transferred to the structure; however, the dissipating elements may need to be replaced after every significant impact, which increases operating costs (Wyllie, 2015). The reduction in the number of manufacturers, the increase in cost as capacity grows, and the shortening of the barrier length caused by impacts are weaknesses of the system. Three main criteria govern the design: the energies, velocities, and bounce heights to be attained along the travel paths. Since a block travelling faster than about 35 m/s may perforate the net, flexible barriers should be positioned in sections where velocities remain below this threshold (Çelik and Nasery, 2021). The barrier height is determined by multiplying the largest bounce height at the relevant section by an appropriate safety factor, for which a value of 1.5 is recommended in the literature (Plassiard and Donzé, 2010). Grading the capacity along the alignment is an important source of economy.

Channel (Static) Barriers for Narrow Valleys

Channel barriers, originally developed to retain material carried by flash floods from narrow valleys, are also used in rockfall mitigation thanks to their structural features. Where a distinct narrow valley exists on the slope, and it has been verified that all potentially falling blocks will be funnelled into it, this system, also known as a 'debris barrier' or 'static barrier', is preferred. It consists of prefabricated steel meshes and high-strength steel cables with tensile strengths of the order of 1770–2160 MPa. The density and aperture of the cable-woven net are selected according to the anticipated rainfall and block size; horizontal and vertical nets are connected with special clips, and the system is anchored to sound bedrock on both sides and at the base. A fine-aperture prefabricated wire mesh is placed inside the woven net to retain small fragments. An important advantage of the system, which can be built in one or several tiers according to site conditions, is that water from the stream bed can pass freely through it; if desired, energy dissipators can be added so that the barrier stretches downstream during impact and retains the material effectively. In the Sille Valley project, sections of intense block accumulation were identified by sensitivity analyses for blocks directed into the dry stream beds, and repeated three-dimensional analyses on the barrier-equipped model confirmed that 4 m high channel barriers placed at the narrowest sections of the valleys were able to stop all of the blocks (Nasery, 2025).

Passive Surface Draping with Wire Mesh

In mesh-based rockfall measures, the character of the application depends on how the mesh is connected to the slope. If the mesh is fixed with anchors placed at regular intervals over the face and block movement is restrained at the source, the system is regarded as active protection. If, by contrast, the mesh is supported only at the crest and, where necessary, at the toe, so that it prevents rock fragments from bouncing freely and leaving the slope in an uncontrolled manner, it functions as passive draping. In passive draping systems, small and medium-sized detached fragments are guided between the mesh and the rock face and travel in a controlled fashion down to the slope toe. The method offers a practical solution, especially on wide, steep faces with a high density of discontinuities. System performance is directly related to a suitable anchor layout, adequate mesh strength, steel cable reinforcement, and the regular removal of material accumulating at the toe.

Rigid Systems: Reinforced-Earth Barriers and Retaining Walls

In rockfall control, some protection structures are used to stop falling blocks within a defined zone, to guide them, or to limit their travel distance. Such systems generally have no separate energy-dissipating element and can be built of reinforced concrete, stone, steel, earthfill, or gabions. Working in a manner similar to conventional retaining walls, these structures provide effective and practicable solutions, particularly for low-energy rockfall events. Where the fall height is large, block sizes grow or impact energies increase, systems with higher energy-absorption capacity are needed. In this context, reinforced-fill barriers, rock-catching earth structures, and gabion walls are prominent passive protection alternatives. Gabion walls are widely preferred engineering solutions for rockfall risk reduction owing to their flexible behaviour, drainage capability, use of local materials, and easy adaptation to the site. Composed of wire cages filled with soil, stone, or similar natural materials, these systems form an effective line of defence against blocks of high kinetic energy (Oggeri and Peila, 2000; Nomura et al., 2002; Ronco et al., 2009). Since it has been shown that the energy-dissipation capacity increases as the grain size of the infill decreases, fine-grained fills may be preferred in impact-oriented applications (Lambert and Kister, 2018). Reinforced-earth barriers behave reliably under high-energy or successive impacts; their cross-sections are dimensioned on the basis of the total kinetic energy of the blocks expected to strike them, and in these respects they can be advantageous over flexible barriers in the very high energy classes (Ronco et al., 2009; Lambert and Bourrier, 2013).

In practice, rock-catching reinforced-earth barriers are built with a front face inclined forward at about 67°, in contrast to conventional vertical gabion walls (Peila et al., 2007; Lambert and Bourrier, 2013). The cage wires are laid in U-shaped layers and filled with compacted soil; to prevent erosion, air- and water-permeable UV-resistant liners are placed inside the cages where possible, and the structure is vegetated, with topsoil spread on the face and hydroseeding, so that it blends into the landscape. Thanks to the weight of the fill, the system acts as a gravity wall. For these structures, referred to in the literature as 'reinforced embankments', no standard dimensioning code exists yet, mainly because fine-grained fills exhibit non-linear stress–strain behaviour and undergo large deformations under impact. Full-scale tests have therefore been carried out to understand the behaviour, and their results have been introduced into the literature (Peila et al., 2007; Ronco et al., 2009; Lambert and Bourrier, 2013; Çelik, 2023).

CURRENT ROCKFALL DETECTION AND ANALYSIS STUDIES

Correct selection and dimensioning of the protection structure depend on correct identification of the risk. In current practice, the detection process starts with the production of a high-resolution three-dimensional digital model of the terrain. Unmanned aerial vehicle (UAV) photogrammetry and LiDAR scanning, combined with centimetre-level GNSS/RTK positioning, are used to produce base maps, dense point clouds, triangulated irregular networks (TIN) and digital elevation models (DEM). In the digital oblique photogrammetry campaign of the Sille Valley, 1375 high-resolution photographs were captured in flights at an altitude of 105 m with 90% overlap, based on nine ground control points surveyed with CORS-GNSS at 2 cm accuracy; a cloud of about 97.4 million points and a triangulated mesh of 50 million faces yielded resolutions of 2.89 cm/pixel for the orthophoto and 5.45 cm/pixel for the DEM, with maximum deviations at the control points of 3.7 cm horizontally and 6.9 cm vertically. Planning the flights close to sunrise and sunset to reduce shadowing was also recommended in the same study (Nasery, 2025). This level of accuracy is critical in rocky terrain for the realism of stability and trajectory analyses. Because destructive methods such as drilling cannot be used in heritage sites, geophysical techniques such as multi-channel electrical resistivity tomography (ERT) and seismic refraction surveys come to the fore in characterising subsurface conditions.

Trajectory (rockfall) analyses are the step in which detection studies are linked to protection-structure design. Two-dimensional analyses provide the travel distance, bounce height, velocity and kinetic energy of blocks along selected sections, and have been used in the studies of Afyonkarahisar

Castle (Topal et al., 2007), Ermenek (Taga and Zorlu, 2017) and Ankara Citadel (San et al., 2020). Three-dimensional stochastic analyses, using a Monte-Carlo approach, vary the initial conditions, the ground restitution coefficients (Rn, Rt) and the friction coefficient (k) probabilistically to generate the spreading area, the travel paths and the energy–velocity–bounce envelopes; the variability, limit-velocity and lateral/vertical deviation inputs of the parameters are defined probabilistically according to the lithological diversity (Kara, 2020). Comparative studies have shown that two-dimensional analyses estimate the kinetic energy higher — on the safe side — than three-dimensional ones (Akın et al., 2024). In addition, regional risk mapping with GIS and remote sensing (Çelik and Gülersoy, 2017), hazard rating systems (Saroglou et al., 2012) and finite-element prediction of the damage that falls would cause to structures (ABAQUS and ANSYS applications for the damage analysis of registered buildings and the capacity verification of protection structures) complete the current detection–assessment chain. The energy, velocity and bounce values thus obtained constitute the direct input for the siting, height and capacity design of the gabion walls addressed in the next section.

DESIGN AND IMPACT PERFORMANCE OF GABION WALLS

Gabion walls are flexible and permeable gravity structures formed by filling cages woven from galvanised double-twisted wire with stone. Having a wide range of uses including retaining walls, noise screens, stream training works and slope protection (Perera and Lam, 2023), gabions appear in rockfall mitigation in three distinct roles: (i) as an independent gravity barrier against blocks of low to medium energy, (ii) as a cushion layer in front of reinforced concrete impact walls, preventing punching and delaying momentum transfer, and (iii) as the facing element of rock-catching reinforced-earth barriers. Their ability to slow falling rocks and absorb their energy, together with their environmentally friendly and aesthetic appearance, is frequently emphasised in the literature (Ramli et al., 2013; Lambert and Bourrier, 2013).

General Form, Geometry, and Material Properties

Gabion units are box-shaped cage systems formed of wire mesh to hold the stone fill together. Generally manufactured as rectangular prisms, the cages are made of double-twisted, hexagonal-mesh mild steel wire to increase flexibility and strength. Depending on the service environment, the steel is produced with galvanised, Galfan, galvanised+PVC, Galfan+PVC, or polymer coating; galvanised wire is preferred in dry environments and galvanised+PVC wire in wet and corrosive ones, and thanks to these coatings, the service life of gabion baskets reaches roughly 20–120 years (Uray, 2014). In practice, the wire diameter varies between 2.0 and 4.0 mm and the mesh aperture between 6×8, 8×10, and 10×12 cm, larger apertures being paired with larger wire diameters. The most common module size in experimental and full-scale studies is 2×1×1 m; baskets longer than 2 m are divided into 1 m cells with intermediate panels called diaphragms, so that the desired size is achieved without sacrificing strength (Uray, 2014). Ersalman (2023) reports that four different wire components are used in gabion manufacture (mesh wire, edge/frame wire, lacing wire and lacing ring) and that, according to the specification, the lacing wire must have the same tensile strength as the double-twisted mesh and a diameter of at least 2.2 mm, while the lacing ring must carry a tensile strength of at least 2 kN (Figure 3).

The gabion fill stone should be hard, unweathered and resistant to freeze–thaw and abrasion, and should be sized so that it cannot escape through the mesh aperture yet allows dense packing within the basket. Ersalman (2023) reports grain sizes of 100–150 mm for mattress gabions and 125–250 mm for basket gabions. Angular and rough stones provide high interlocking and internal friction, whereas excessively flat stones may create oriented voids and local force chains; rounded grains increase permeability but are more easily rearranged under impact. Typical unit weights given by Uray (2014) are about 17 kN/m^3 for pumice, 22 kN/m^3 for soft limestone, 23 kN/m^3 for sandstone, 26 kN/m^3 for granite and hard limestone, and 29 kN/m^3 for basalt. This variation shows that, for walls of identical external geometry, the total weight — and hence the sliding and overturning resistance — can change considerably with the rock type.

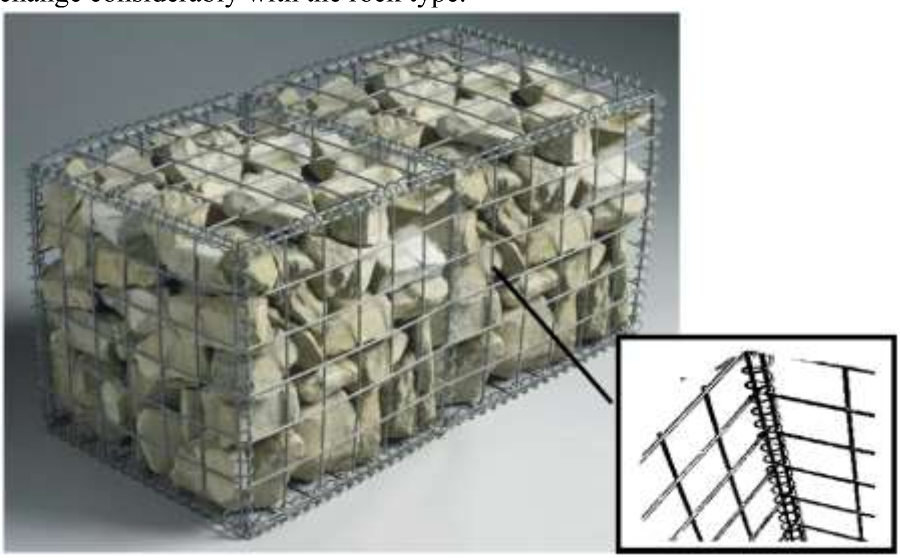

Figure 3: Wire mesh panel of a gabion basket and the spiral-wire lacing detail
Source: Uray (2014)

The main reasons why gabions are preferred as protection structures are their flexible behaviour with a large deformation capacity; their high permeability, which prevents water pressure from building up behind them; the fact that the fill stone can usually be obtained easily near the construction site; their modularity, which allows damaged cells to be repaired or replaced in place; their low initial and operating costs; and their vegetation-friendly, environmentally compatible appearance (Ramli et al., 2013; Nasery, 2025). Mechanically, the gabion is a composite material in which the wire cage and the granular fill act together; since manufacturing methods, fills, and standards vary from region to region, it is recommended that the stiffness parameters be determined by project-specific tests. For this purpose, an unconfined compression test is performed on a representative gabion cell, and the compression modulus (ME) is obtained (Agostini, 1987; Perera and Lam, 2023).

Static and Theoretical Design Principles

Since a gabion wall is a gravity structure resting on the ground, the classical retaining-wall verifications are the starting point of design: safety against sliding, overturning, and global (slope) failure must be ensured, and the base pressures must not exceed the allowable bearing capacity of the soil (TS 7994, 1990; Uray, 2014). In the sliding check, the lateral thrust tending to displace the wall along a horizontal sliding plane is compared with the resultant of the resisting friction, cohesion, and passive earth thrust (Figure 4); the friction coefficient is usually taken as $f = \tan\varphi$ and the computed factor of safety is required to be at least 1.5 (Uray, 2014). In the overturning check, the overturning moment of the active earth pressure about the toe is compared with the restoring moment of the wall self-weight and the passive thrust; a factor of safety of at least 1.5 is again required. In the global (slope) failure check, circular or planar slip surfaces enclosing the wall and the surrounding soil are trialled, the minimum factor of safety is found and compared with a limit value generally between 1.2 and 1.3 (Uray, 2014). Ersalman (2023) has likewise shown that the safety factors remain above the 1.5 limit under various blast/impact loads. Gabion-specific internal stability checks comprise the verification of the tensile capacities of the cage and lacing (seam) wires and of the inter-cell sliding friction; according to the specification, the tensile strength of the standard wire mesh is of the order of 200 kN/m and the connection strength about 70 kN/m (Ersalman, 2023). As regards wall geometry, building the wall with a batter of 6–10° to improve sliding stability, selecting the base width between one half and two thirds of the wall height, and keeping the total height below 10 m are recommended (Uray, 2014).

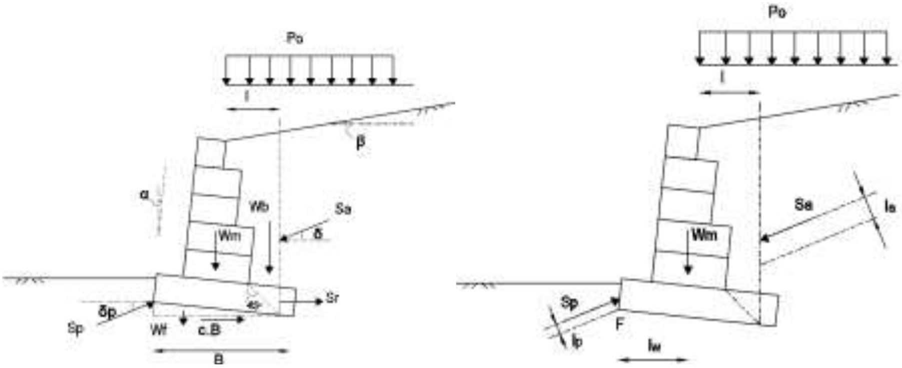

Figure 4: Forces acting on a gabion retaining wall in the sliding (left) and overturning (right) checks
Source: Uray (2014)

Design under impact requires, beyond the static checks, the modelling of the block–cushion–structure interaction. The design demand consists of the kinetic energy computed with Equation (1) and the velocity and bounce values obtained from the trajectory analyses. For the maximum contact force between the block and the gabion cushion, the empirical relationship given in the Swiss road authority guideline for granular cushions on rock sheds (ASTRA, 2008), which has been shown to be sufficiently accurate for gabion cushions as well, may be used (Perera et al., 2021; Perera and Lam, 2023):

$$F_{c,max} \approx 2.8 \cdot e^{-0.5} \cdot r^{0.7} \cdot M_E^{0.4} \cdot \tan\varphi_k \cdot \left(\frac{mv_0^2}{2}\right)^{0.6} \tag{2}$$

Here m is the mass of the striking block, v_0 the impact velocity, e the thickness of the (gabion) cushion, r the radius of the spherical impactor, ME the compression modulus of the cushion, and φ_k the internal friction angle of the fill grains. The recommendations of the Swiss guideline are based on the pioneering experimental study in which a value of ME = 3200 kPa was reported from a plate-loading test on a gravel cushion (Labiouse et al., 1996). The relationship was derived for vertical impact; for horizontal impact scenarios, it is recommended that the coefficient 2.8 be reduced to 1.8 (Perera et al., 2021; Perera and Lam, 2023). For a given impact scenario (with velocity, mass, cushion thickness, and impactor diameter fixed), all terms other than ME can be lumped into a single constant:

$$F_c = C_{ME} \cdot M_E^{0,4} \tag{3}$$

The impact force applied to a granular cushion is transmitted to the base through force chains that develop radially within the layer; the number and stability of the force chains are highest near the impact point. Under successive impacts, additional force chains develop because of the increased confinement and the cushion stiffens; this mechanism forms the physical basis of the multiple-strike behaviour of the gabion cushion (Zhang et al., 2017).

Gabion Walls under Rock Impact: Recent Experimental and Numerical Studies

The experimental literature on the impact behaviour of gabions has grown markedly over the past decade. Ng et al. (2016) examined the response of a gabion layer placed in front of a rigid barrier to successive large-scale boulder strikes; in that work, however, the multiple-strike effect was treated qualitatively and was not converted into a quantitative design rule (Perera and Lam, 2023). Perera et al. (2021), through single-strike full-scale tests on a reinforced concrete wall protected by a gabion cushion, quantified the substantial reductions in contact force and wall deflection demand and validated predictive relationships. On the reinforced-earth front, Peila et al. (2007) and Ronco et al. (2009) developed design approaches based on full-scale tests; Lambert and Bourrier (2013) compiled the design principles of this structural class; Bourrier et al. (2011) demonstrated the contribution of multi-scale modelling, and Breugnot et al. (2016) that of coupled discrete–continuum models to the design of cellular protection structures. At the material scale, Zhang et al. (2022) classified the failure modes of gabion cells experimentally; at the system scale, Mummadisingh and Sengupta (2023) investigated the dynamic performance of a gabion wall, and Yue et al. (2024) the seismic behaviour of slopes with gabion-reinforced retaining walls through shaking-table tests.

One of the most comprehensive experimental programmes in this field was carried out by Perera and Lam (2023). The starting point of that study was the absence in the literature of a rational design method describing how the gabion buffer (cushion) layer placed in front of reinforced concrete rockfall barriers behaves under repeated impact; earlier studies had either considered a single strike or treated repeated strikes only qualitatively. To close this gap, the authors devised a two-stage experimental programme: in the first stage, small-scale drop tests on the gabion fill material tracked how the contact force changes under repeated impacts, while in the second stage, horizontal pendulum blows were applied to a full-scale reinforced concrete wall fronted by a gabion layer, and the momentum transfer and wall displacement demand were measured. In the first stage, cubic gabion boxes with 100 mm edges, 1:5 scale models of the common 500 mm gabion box, were fabricated from double-twisted hexagonal mesh with 0.56 mm wire diameter and 13 mm aperture. To generalise the effect of fill roughness, two fills of distinctly different mechanical properties were selected: rounded, smooth-surfaced pebbles (15–20 mm diameter, specific gravity 2.83, mean grain crushing strength 1890 N, angle of repose 21.9°, circularity 0.81) and angular crushed stone (specific gravity 2.68, crushing strength 2635 N, angle of repose 26.4°, circularity 0.69); sieve analyses showed the grain-size distributions of the two materials to be nearly identical. Nine gabion cells were arranged in a 3×3 layout inside a timber frame, and a cast-iron sphere of 5 kg mass and 55 mm radius, instrumented with an accelerometer of 2500 g capacity, was released from an adjustable hook at heights of 0.5, 1.0 and 2.0 m (impact energies of 24.5–98.1 J) onto the same point four times in succession (Perera and Lam, 2023). Acceleration records were sampled at 10 kHz and denoised with a 1000–2000 Hz Butterworth filter, and the contact force was obtained as the product of acceleration and impactor mass; the progressive rise of the contact force after each strike thus allowed the increase of the fill compression modulus (ME) to be tracked. The full-scale gabion boxes used in the second stage were deliberately of a different type from those of the small-scale tests: steel cages with 50 mm square aperture and 5 mm wire diameter were filled with 70–100 mm crushed stone, a 500×500×500 mm box weighing on average 181 kg, which corresponds to a bulk density of 1448 kg/m³. To determine the initial compression modulus of the cushion, quasi-static compression tests were performed on the full-scale gabion box under unconfined conditions (Figure 5): an actuator capable of loading rates of up to 1 MN/s was used, a steel plate 32 mm in thickness was laid over the specimen so that the load spread uniformly across the top face, and the box was compressed under displacement control at 1 mm/s up to a strain of 0.2; the average of four tests gave ME ≈ 2985 kPa (about 3000 kPa).

Figure 5: Unconfined compression test on a full-scale gabion box
Source: Perera and Lam (2023)

The reinforced concrete barrier specimen used in the full-scale impact tests consists of a stem wall 1.5 m high and 0.23 m thick resting on a base slab 0.5 m thick and 1.23 m long; the base slab was clamped tightly to the strong floor of the laboratory to provide a fixed support condition. The wall was reinforced with fifteen D500N bars on each of the tension and compression faces, and thirty strain gauges of high elongation capacity, able to record beyond yield, were bonded to the vertical bars near the wall base before concreting. Wall motion was monitored at four levels on the rear face (near the ground, at H/3, at 2H/3, and near the top edge) with ILD 1302 laser sensors mounted on a separate timber frame to isolate them from vibration, and possible movements of the base slab were checked with additional laser sensors. Nine gabion boxes in a 3×3 arrangement were placed in front of the wall inside a plywood frame and secured to the wall with truck lashing straps; the tests were repeated with three cushion thicknesses of 300 mm, 500 mm, and 1000 mm. The blows were applied horizontally by a pendulum arrangement using three solid steel 'torpedo' impactors of 280 kg, 435 kg and 1020 kg with hemispherically machined heads, released from drop heights of 0.5–1.4 m (impact energies of 1.37–10 kJ); the impactor acceleration was recorded with a Dytran 3200B6M accelerometer, and the instant of impact and the impactor velocity with a Phantom v2512 high-speed camera (Figure 6) (Perera and Lam, 2023). A total of 32 tests were performed; after four strikes at the same point, the gabion layer was replaced with new boxes, and only in the series where the 1020 kg impactor struck the 500 mm and 1000 mm cushions were the tests limited to two strikes, because the cages were completely destroyed at the end of the second strike (Perera and Lam, 2023).

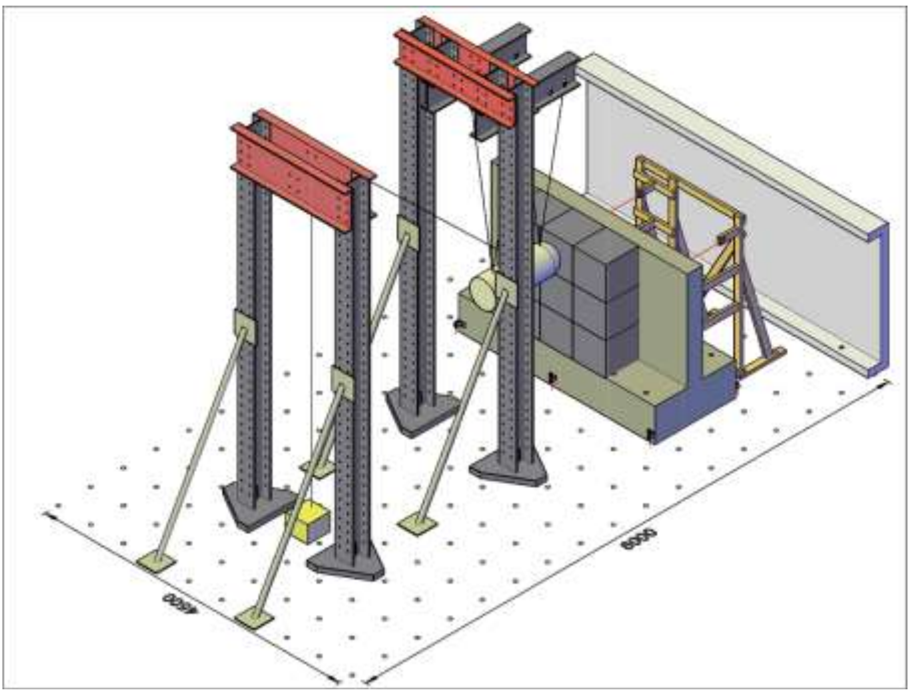

Figure 6: Three-dimensional view of the full-scale pendulum test set-up
Source: Perera and Lam (2023)

The findings revealed that repeated impacts produce a pronounced compaction effect in the cushion. In the small-scale drop tests the compaction was observed to arise solely from grain rearrangement rather than grain crushing, and the contact force increased progressively with each strike; in the test on the crushed-stone cushion from a height of 1 m, for example, the peak contact force of the second strike was measured at 1.19 times that of the first (4494 N versus 3776 N) (Perera and Lam, 2023). A statistical evaluation over the different drop heights and fill types showed that the contact-force multiplier (CF,n) takes average values of 1, 1.32, 1.62, and 1.9 according to the strike number, and that these multipliers are largely independent of cushion size and fill type (Perera and Lam, 2023). Using the Fc ∝ ME0.4 relationship of the contact-force expression in the Swiss guideline (ASTRA, 2008), these multipliers were converted into increases of the compression modulus, and the ME values for successive strikes were computed as 1.0, 2.0, 3.3 and 5.0 times the initial value; for a cushion with an initial value of 3000 kPa this corresponds to approximately 3000, 6000, 10,000 and 15,000 kPa, respectively (Perera and Lam, 2023). That these dimensionless multipliers, derived at small scale, are applicable to the full-scale tests as well was confirmed by the near-perfect agreement between the peak contact forces measured in all 32 tests and the values computed with the relationship; the proposal to reduce the coefficient 2.8 to 1.8 for horizontal impact was likewise corroborated by these tests (Perera and Lam, 2023).

The state of the cushion surface after each strike was documented photographically, and the gabion layer was shown to remain serviceable, with acceptable deformation and without repair, for up to four successive strikes (Figure 7); in the later strikes, when grain interlocking (confinement) had increased, the increment of permanent settlement typically remained small while the contact force rose. As the cushion thickness increased, the variation of contact force between strikes diminished markedly (from t = 300 mm to t = 1000 mm); in every condition the largest difference occurred between the first and second strikes, with progressively smaller differences between later ones. A similar trend was observed in the wall response: the laser measurements showed the wall-top displacement to grow as the cushion became thinner, and the reinforcement and concrete-surface strain distributions displayed a distinct difference between the first and second strikes but only small differences thereafter; the authors stress that this compaction phenomenon must be taken into account in the design of the stem wall (Perera and Lam, 2023).

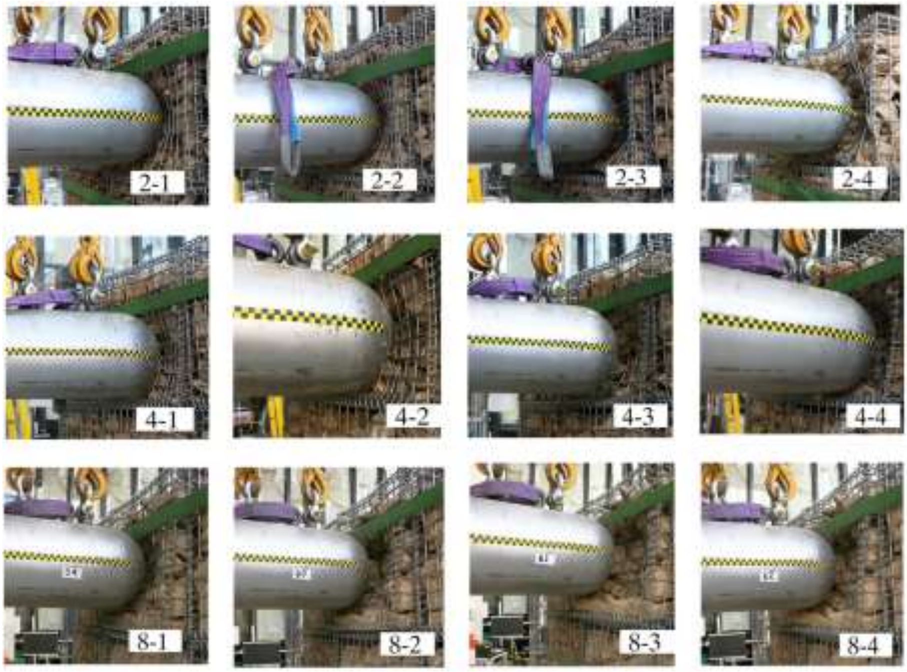

Figure 7: Appearance of the cushion surface after successive impact strikes

Source: Perera and Lam (2023)

Building on the experimental findings, the authors proposed a three-step procedure which they call the 'displacement-based design method': (1) determination of the initial compression modulus by a quasi-static unconfined compression test on a representative gabion specimen and its updating with the multipliers 1.0–2.0–3.3–5.0 according to the strike number; (2) derivation of the cushion stiffness (kl) from the computed peak contact force; and (3) estimation of the wall displacement demand in a model representing the impactor and the wall as a two-degree-of-freedom (2DOF) spring–mass system, with the cushioning coefficient γ representing the delay of momentum transfer. The model predictions agree well with the wall displacements measured in all test series, for both the first and the subsequent strikes; it was also shown that the stiffness of thin (300 mm) cushions is more sensitive to the strike number (Perera and Lam, 2023). From the practical standpoint, the most striking outcome of the study is that a gabion cushion layer placed in front of a reinforced concrete wall can reduce the wall displacement demand by 50–90% and provide protection for up to four successive strikes; this reduction was found to depend strongly on cushion thickness and to be insensitive to the fill type. Maintenance effort can thus be directed to genuine need instead of routine repair after every event, and the life-cycle maintenance costs of barriers on slopes of difficult access can be reduced considerably (Perera and Lam, 2023).

For the capacity verification of gabion-faced reinforced-earth barriers, the Sille Valley study offers an up-to-date template (Nasery, 2025). Taking an average block volume of 9.35 m³ (about 15.3 tonnes) in the dacitic breccia zone, 1200 two-dimensional and 500 three-dimensional analyses were run along 12 travel paths with 100 probabilistic realisations each; 93% of the blocks were found to reach the barrier line, the most unfavourable demand was determined as a bounce height of up to 4.03 m, a velocity of 18.4 m/s and an energy of 2805 kJ, and a gabion-faced reinforced-earth barrier 5.25 m high, with a 1 m crest width and a 67° face inclination, was proposed. In the ABAQUS model, 20 m long, built up in 0.75 m layers to represent the staged construction, and meshed with 200 mm C3D8R elements selected through a convergence study, the fill was defined with parameters from the literature (Ronco et al., 2009; Nasery, 2025). Since the front-face gabion wires were observed to make no significant contribution to the structural response, their essential function being to stabilise the fill, the wires were conservatively neglected. In the 3000 kJ impact analysis, a maximum displacement of 463 mm and a maximum stress of 1.16 MPa were computed on the rear (protected) face of the barrier, and 92% of the energy was dissipated by the barrier; in the 5000 kJ analysis, these values were 710 mm, 1.27 MPa, and 98%, respectively (Figures 8 and 9). The governing criterion was not the stress but the requirement that the rear-face displacement should not exceed the crest width (Ronco et al., 2009); the cross-section remains undamaged up to 3000 kJ, stops the block at 5000 kJ at the cost of possible local repair, and the pre-collapse capacity reported in the literature for sections with a 1 m crest width and 67° inclination is 7500–10,000 kJ (Nasery, 2025). These results confirm, at case scale, the finding of Lambert and Bourrier (2013) that such barriers can absorb energies of the order of thousands of kilojoules through large plastic deformations, and they show that the verification of cross-sectional integrity by non-linear analyses should become a standard design step.

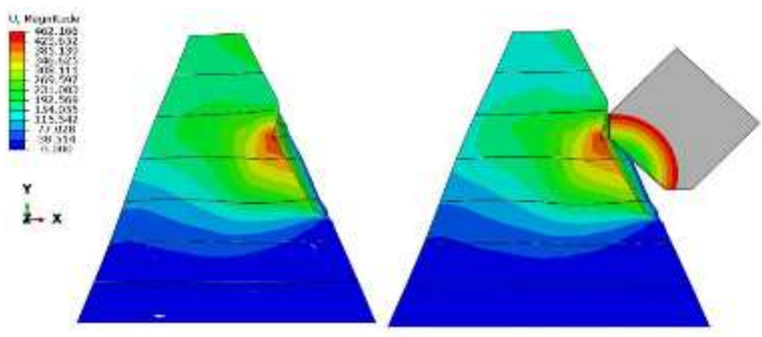

Figure 8: Displacement diagrams (mm) produced in the 5.25 m high reinforced-earth barrier by the impact of a rock block with an energy of 3000 kJ
Source: Nasery (2025)

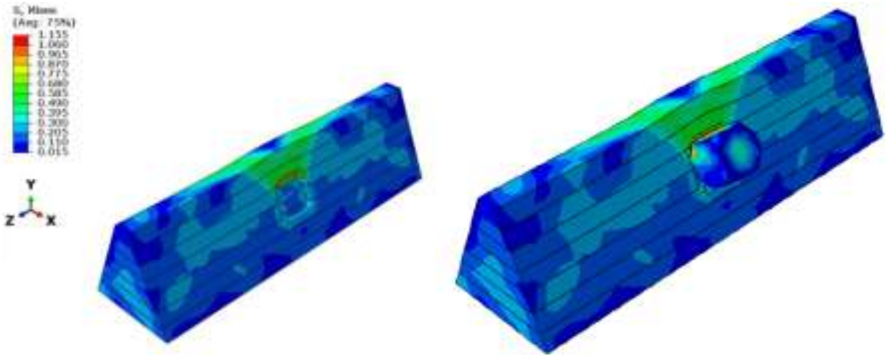

Figure 9: Stress distributions (MPa) produced in the 5.25 m high reinforced-earth barrier by the impact of a rock block with an energy of 3000 kJ
Source: Nasery (2025)

Read together, these studies clarify the place of gabion walls in rockfall mitigation. Gabion-based barriers are most efficient at slope toes where the blocks pass into a rolling regime, the bounce height decreases while the energy remains high, and a sufficient buffer area exists in front of the structure; indeed, in the Sille Valley the bounce heights of 8–10 m on the steep slope sections were shown to drop to 3–4 m as the barrier line was approached, so that the demand in this zone could be met by barrier-type solutions (Nasery, 2025). Since flexible barriers face a perforation risk where the block velocity exceeds 35 m/s (Çelik and Nasery, 2021), gravity-based gabion or reinforced-earth sections, or combined solutions in which velocity and bounce are first controlled by mesh draping, come to the fore in high-velocity, high-energy combinations. Reinforced-earth sections can absorb energies of the order of thousands of kilojoules through large plastic deformations (Ronco et al., 2009; Lambert and Bourrier, 2013; Nasery, 2025), while gabions used as cushions in front of reinforced concrete barriers reduce both the punching risk and the deflection demand substantially and can eliminate maintenance for up to four successive strikes (Perera and Lam, 2023). The cushion/wall thickness is the principal design variable; determining ME by project-specific tests, applying the successive-strike multipliers, and verifying the cross-section by non-linear finite element analyses constitute current good practice. By contrast, the absence of an internationally accepted dimensioning standard for gabion and reinforced-earth barriers (Lambert and Bourrier, 2013), their long-term behaviour under wire corrosion and freeze–thaw, cage integrity under very high-velocity impacts, and the need for representative testing when moving between module scales (Perera and Lam, 2023) remain open research topics in the field.

CONCLUSIONS AND EVALUATION

Rockfall is a disaster that emerges suddenly through the combination of discontinuity development, slope inclination, and triggering forces, carries high kinetic energy, and therefore allows no intervention at the moment of the event. The cost–benefit balance in rural areas, the density of development in city centres, the fixed alignment of engineering structures, and the silhouette and minimum-intervention principles in heritage sites shape both the detection and the mitigation approach.

Today, the detection process rests on the production of centimetre-accurate three-dimensional terrain models by unmanned-aerial-vehicle photogrammetry and laser scanning, the non-destructive characterisation of subsurface conditions by geophysical methods, inventories of hazardous blocks, and two- and three-dimensional trajectory simulations; the energy, velocity, and bounce-height values obtained from these analyses constitute the direct input of protection-structure design.

Taken as a whole, the findings presented here demonstrate that gabion walls can be relied upon not merely as a component complementing other systems but as a stand-alone rock-catching barrier. The most favourable conditions for stand-alone gabion walls are slope toes where block motion passes into a rolling regime, and the bounce height decreases while the kinetic energy remains high, and sites where a sufficient buffer area exists in front of the wall. Gabion-based systems, particularly gabion-faced reinforced-earth barriers and gabion cushions used in conjunction with reinforced concrete walls, have demonstrated substantial energy-dissipation capacity under the investigated conditions. Practical experience shows that the wall alignment should be chosen along routes of the lowest possible gradient; that the loose surface cover should be stripped so that the wall is founded, with a certain embedment depth, on a stratum of adequate bearing capacity; and that at sites with large block sizes, simple measures such as trenches cannot be expected to suffice on their own. The indicative measures suggested by risk classification systems should accordingly be treated as a starting point, and the final choice must be verified by field measurements and trajectory analyses.

The common message of the experimental and numerical studies is that the gabion works as a composite system dissipating energy through inter-grain friction, rearrangement and large plastic deformations. Under impact, damage mostly remains confined to a few cells in the contact zone, displacements are measured at the centimetre scale, and the wall preserves its integrity and continues to function; the possibility of repairing or replacing damaged cells in place is among the most important advantages of these systems in the operating period. The same behaviour is observed in the other two forms of use: gabion-faced reinforced-earth sections can dissipate the great majority of impact energies of the order of thousands of kilojoules, while gabion cushion layers placed in front of reinforced concrete barriers substantially reduce the contact force and the displacement demand of the wall and provide repair-free protection over successive strikes. Maintenance effort can thus be directed to genuine need rather than routine repair after every event, and the life-cycle costs of protection structures on slopes of difficult access can be reduced considerably.

It is remarkable that studies conducted in different regions, in different geological settings and at different scales converge on the same workflow: production of a high-resolution terrain model, determination of the design demands by probabilistic three-dimensional trajectory analyses, selection of the wall position and cross-section according to these demands, and testing of the design by non-linear numerical analyses. The design flow recommended for gabion-based protection structures should therefore comprise project-specific material and compression-modulus tests, allowance for repeated-impact effects through appropriate multipliers, displacement-based preliminary sizing, verification of cross-sectional integrity by finite element analyses, and careful foundation preparation. Testing the reliability of the proposed remedial solution not only by trajectory analyses but also by numerical verifications covering the structural behaviour should become a standard step of design practice. On the other hand, the fact that no internationally accepted dimensioning code yet exists for gabion and reinforced-earth barriers means that design still relies largely on project-specific tests and analyses. The development of more detailed modelling approaches in which the wire mesh and the stone fill are represented separately, the diversification of full-scale multiple-strike tests with different module sizes and impactor shapes, the clarification of behaviour under seismic action, and the monitoring of long-term durability under wire corrosion and freeze–thaw cycles constitute the principal research agenda of the field. Progress on these topics will pave the way for the even more confident use of gabion walls, increasingly widespread thanks to their economy, their use of local materials, and their environmental compatibility, as a stand-alone protective measure against rockfall.

REFERENCES

Agostini, R. (1987). *Flexible Gabion Structures in Earth Retaining Works*. Officine Maccaferri, Bologna.

Akın, M., Dinçer, İ. and Orhan, A. (2020). *Kaya Düşmelerinden Kaynaklı Afetlerin Değerlendirilmesine Yönelik Teknik Kılavuz* [in Turkish]. Disaster and Emergency Management Authority (AFAD), Ankara.

Akın, M., Dinçer, İ., Orhan, A., Ok, A.Ö., Akın, M.K. and Topal, T. (2019). Evaluation of the performance of a rockfall ditch by 3-dimensional rockfall analyses: Akköy (Ürgüp) case. *Jeoloji Mühendisliği Dergisi, 43*(2), 211–232.

Akın, M., Dinçer, İ., Orhan, A. and Varol, O.O. (2024). A comparative study on rockfall block motion characteristics using 3-D and 2-D rockfall simulations: A case study from Cappadocia (Mazı, Türkiye). *Natural Hazards*, 1–27.

ASTRA (2008). *Einwirkungen infolge Steinschlags auf Schutzgalerien* (Richtlinie). Bundesamt für Strassen, Bern.

Baillifard, F., Jaboyedoff, M., Rouiller, J.D., Couture, R., Locat, J., Robichaud, G. and Gamel, G. (2004). Towards a GIS-based hazard assessment along the Quebec City promontory. *Landslide Evaluation and Stabilization*, 207–213, Canada.

Bourrier, F., Lambert, S., Heymann, A., Gotteland, P. and Nicot, F. (2011). How multi-scale approaches can benefit the design of cellular rockfall protection structures. *Canadian Geotechnical Journal, 48*(12), 1803–1816.

Bozzolo, D. and Pamini, R. (1986). Simulation of rock falls down mountain slopes. *Proceedings of the 5th International Congress on Rock Mechanics*, 2, 1291–1299.

Breugnot, A., Lambert, S., Villard, P. and Gotteland, P. (2016). A discrete/continuous coupled approach for modeling impacts on cellular geostructures. *Rock Mechanics and Rock Engineering, 49*(5), 1831–1848.

Çelik, M. (2023). Investigating the performance of passageway corridor for ground reinforced embankments against rockfall. *Journal of Mountain Science, 20*(1), 15–30.

Çelik, M. and Nasery, M.M. (2021). Eğimli arazilerde kaya tutucu toprakarme duvarların uygulanabilirliği ve alternatif kaya ıslahı çözümleriyle karşılaştırılması: Kanlıpelit örneği [in Turkish]. *Doğal Afetler ve Çevre Dergisi, 7*(1), 176–191.

Çelik, M.A. and Gülersoy, A.E. (2017). Evaluation of rock fall risk in Kilis (Turkey) city by using GIS and remote sensing. *International Journal of Computational and Experimental Science and Engineering, 3*(1), 1–4.

Dorren, L.K.A. (2003). A review of rockfall mechanics and modelling approaches. *Progress in Physical Geography, 27*(1), 69–87.

EOTA (2008). *ETAG 027: Guideline for European Technical Approval of Falling Rock Protection Kits*. European Organisation for Technical Approvals, Brussels.

Ersalman, İ. (2023). *Gabion Duvarın Koruma Yapısı Olarak Kullanımında Mühendislik Özelliklerinin Belirlenmesi* [in Turkish]. MSc Thesis, Kırıkkale Üniversitesi Fen Bilimleri Enstitüsü, Kırıkkale.

Gökçe, O., Özden, Ş. and Demir, A. (2008). *Türkiye'de Afetlerin Mekânsal ve İstatistiksel Dağılımı: Afet Bilgileri Envanteri* [in Turkish]. Ministry of Public Works and Settlement, Ankara.

Görüm, T., Tanyaş, H., Karabacak, F., Yılmaz, A., Girgin, S., Allstadt, K.E., Süzen M., L., and Burgi, P. (2023). Preliminary documentation of coseismic ground failure triggered by the February 6, 2023 Türkiye earthquake sequence. *Engineering Geology, 327*, 107315.

Hutchinson, J.N. (1988). Morphological and geotechnical parameters of landslides in relation to geology and hydrogeology. *Proceedings of the 5th International Symposium on Landslides*, Lausanne, 1, 3–35.

Kara, R.T. (2020). *Üç Boyutlu Kaya Düşme Analizleri ile Olası Tehlike Haritası Üretilmesi ve Önlem Yapıları Tasarımı: Gümüşhane Kent Merkezi Örneği* [in Turkish]. MSc Thesis, Gümüşhane Üniversitesi, Gümüşhane.

Keskin, B., Bacak, G., Bilir, M.E. and Geniş, M. (2020). Investigation of rockfall potential of Zonguldak–Kilimli roadway (Turkey). *Arabian Journal of Geosciences, 13*, 805.

Kishi, N., Konno, H., Ikeda, K. and Matsuoka, K. (2002). Prototype impact tests on ultimate impact resistance of PC rock-sheds. *International Journal of Impact Engineering, 27*(9), 969–985.

Labiouse, V., Descoeudres, F., Montani, S. and Schmidhalter, C. (1994). Experimental study of rock blocks falling down on a reinforced concrete slab covered by absorbing cushions. *Revue Française de Géotechnique, 69*, 41–61.

Labiouse, V., Descoeudres, F. and Montani, S. (1996). Experimental study of rock sheds impacted by rock blocks. *Structural Engineering International, 6*(3), 171–176.

Lambert, S. and Bourrier, F. (2013). Design of rockfall protection embankments: A review. *Engineering Geology, 154*, 77–88.

Lambert, S. and Kister, B. (2018). Efficiency assessment of existing rockfall protection embankments based on an impact strength criterion. *Engineering Geology, 243*, 1–9.

Muhçu, M.Y. (2024). *3 Boyutlu Analizlerle Kaya Şevi Islah Yöntemlerinin Değerlendirilmesi: Hemşin (Rize) Kaya Düşmesi Örneği* [in Turkish]. MSc Thesis, Karadeniz Teknik Üniversitesi Fen Bilimleri Enstitüsü, Trabzon.

Mummadisingh, J.V. and Sengupta, A. (2023). Study of the dynamic performance of a gabion wall. *Structures, 50*, 576–589.

Nasery, M.M. (2025). *Arkeolojik Sit Alanlarındaki (Sille-Konya) Potansiyel Kaya Düşme Alanlarının Belirlenmesi ve Optimum Islah Yöntemlerinin Geliştirilmesi* [in Turkish]. MSc Thesis, Gümüşhane Üniversitesi Lisansüstü Eğitim Enstitüsü, Gümüşhane.

Nasery, M.M. and Çelik, M. (2020). Kaya ıslahı çalışmalarında birleşik çözümlerin incelenmesi: Trabzon Kaymaklı örneği [in Turkish]. *Uludağ Üniversitesi Mühendislik Fakültesi Dergisi, 25*(1), 539–554.

Nasery, M.M., Coşgun, S.İ. and Temel, B.A. (2023). Multi-scenario analysis of rockfall hazard for a historical vaulted masonry building in Sumela Monastery. *International Journal of Architectural Heritage, 17*(11), 1876–1904.

Nasery, M.M., Çelebi, E., Ağcakoca, E., İstegün, B. and Yaman, Z. (2024). Development of fully controlled rock crushing method and its vibration impact during rockfall risk reduction at Assos ancient port: Experimental and field studies. *Case Studies in Construction Materials, 21*, e03882.

Ng, C.W.W., Choi, C.E., Su, A.Y., Kwan, J.S.H. and Lam, C. (2016). Large-scale successive boulder impacts on a rigid barrier shielded by gabions. *Canadian Geotechnical Journal, 53*(10), 1688–1699.

Nomura, T., Inoue, S., Fuchigami, M., Yokota, Y., Kubo, T., Tatta, N. and Arai, K. (2002). Experimental research of reinforced soil wall for rock-fall protection. *Proceedings of the 7th International Conference on Geosynthetics*, Nice, 303–308.

Oggeri, C. and Peila, D. (2000). Protection of transportation systems against rockfalls. *Proceedings of the 8th International Symposium on Landslides*, Cardiff, 1141–1146.

Peila, D., Oggeri, C. and Castiglia, C. (2007). Ground reinforced embankments for rockfall protection: Design and evaluation of full scale tests. *Landslides, 4*, 255–265.

Perera, J.S. and Lam, N. (2023). Rockfall protection wall that can withstand multiple strikes without needing to be repaired. *International Journal of Impact Engineering, 173*, 104476.

Perera, J.S., Lam, N., Disfani, M.M. and Gad, E. (2021). Experimental and analytical investigation of a RC wall with a gabion cushion subjected to boulder impact. *International Journal of Impact Engineering, 151*, 103823.

Plassiard, J.P. and Donzé, F.V. (2010). Optimizing the design of rockfall embankments with a discrete element method. *Engineering Structures, 32*(11), 3817–3826.

Ramli, M., Karasu, T.J.R. and Dawood, E.T. (2013). The stability of gabion walls for earth retaining structures. *Alexandria Engineering Journal, 52*(4), 705–710.

Ritchie, A.M. (1963). Evaluation of rockfall and its control. *Highway Research Record, 17*, 13–28.

Ronco, C., Oggeri, C. and Peila, D. (2009). Design of reinforced ground embankments used for rockfall protection. *Natural Hazards and Earth System Sciences, 9*, 1189–1199.

San, N.E., Topal, T. and Akın, M.K. (2020). Rockfall hazard assessment around Ankara Citadel (Turkey) using rockfall analyses and hazard rating system. *Geotechnical and Geological Engineering, 38*, 3831–3851.

Saroglou, H., Marinos, V., Marinos, P. and Tsiambaos, G. (2012). Rockfall hazard and risk assessment: An example from a high promontory at the historical site of Monemvasia, Greece. *Natural Hazards and Earth System Sciences, 12*, 1823–1836.

Seferoğlu, M.T., Coşgun, S.İ., Çelik, M., Seferoğlu, A.G. and Akpınar, M.V. (2016). A numerical study on rock barriers in Uzungöl region. *ICENS 2nd International Conference on Engineering and Natural Science*, Sarajevo, Bosnia and Herzegovina.

Taga, H. and Zorlu, K. (2017). Assessment of rockfall hazard on steep slopes: Ermenek (Karaman, Turkey). *Yerbilimleri, 38*(2), 161–178.

Topal, T., Akın, M. and Özden, U.A. (2007). Assessment of rockfall hazard around Afyon Castle, Turkey. *Environmental Geology, 53*, 191–200.

TS 7994 (1990). *Zemin Dayanma Yapıları: Sınıflandırma, Özellikleri ve Projelendirme Esasları* [in Turkish]. Turkish Standards Institute, Ankara.

Turner, A.K. and Schuster, R.L. (2012). *Rockfall: Characterization and Control*. Transportation Research Board, Washington, D.C.

Uray, E. (2014). *Gabion Tipi Dayanma Duvarlarında Tasarım Kriterlerinin Araştırılması* [in Turkish]. MSc Thesis, Selçuk Üniversitesi Fen Bilimleri Enstitüsü, Konya.

Varnes, D.J. (1978). Slope movement types and processes. In: Schuster, R.L. and Krizek, R.J. (Eds.), *Landslides: Analysis and Control*, Transportation Research Board Special Report 176, 11–33.

Volkwein, A., Schellenberg, K., Labiouse, V., Agliardi, F., Berger, F., Bourrier, F., Dorren, L.K.A., Gerber, W. and Jaboyedoff, M. (2011). Rockfall characterisation and structural protection – a review. *Natural Hazards and Earth System Sciences, 11*, 2617–2651.

Wyllie, D.C. (2015). *Rock Fall Engineering*. CRC Press, Boca Raton.

Wyllie, D.C. and Mah, C.W. (2004). *Rock Slope Engineering: Civil and Mining* (4th ed.). Spon Press, London.

Yue, M., Qu, L., Zhou, S., Wu, D., Chen, Z. and Wen, H. (2024). Dynamic response characteristics of shaking table model tests on the gabion reinforced retaining wall slope under seismic action. *Geotextiles and Geomembranes*, 52, 167–183.

Zhang, H., Liu, G., Liu, W., Chen, Z., Liu, Q. and Xu, G. (2022). Experimental study on failure mode and mechanical characteristics of gabion material. *Construction and Building Materials, 344*, 128119.

Zhang, L., Lambert, S. and Nicot, F. (2017). Discrete dynamic modelling of the mechanical behaviour of a granular soil. *International Journal of Impact Engineering, 103*, 76–89.